Non-collinear magnetoeletronics in single wall carbon nanotubes

Alina Dora Crisan

UNIVERSITÉ PARIS-SUD

École Doctorale: 107

Laboratoire de Physique des Solides, Paris-Sud
Laboratoire Pierre Aigrain, ENS Paris

THÈSE DE DOCTORAT

Soutenue le 17.12.2013

Présentée par:
Alina Dora CRISAN

Non-collinear Magnetoeletronics in Single Wall Carbon Nanotubes

---

Co-directeur de thèse: Dr. Takis KONTOS
Co-directeur de thèse: Dr. André THIAVILLE

Composition du jury:

Dr. Marco APRILI, Univ. Paris – Sud,	**Président**
Dr. Lauren VILA, INAC – CEA Grenoble,	**Examinateur**
Pr. Elke SCHEER, Univ. Constance,	**Rapporteur**
Pr. François MONTAIGNE, Univ. Lorraine,	**Rapporteur**

To my family.
For the unequivocal support they gave me,
no matter what craziness i chose to do.

To Alex.
With you by my side, i am ready
for a second one.

Acnowledgements

It would not have been possible to complete this doctoral work without the help and support of the kind people around me, to only some of whom it is possible to give particular mention here. The special conditions of this thesis made of the past three and a half years both challenging and enriching ones.

First of all, i would like to thank my two supervisors, Andr Thiaville and Takis Kontos whom, in my perception of things, acted like the two sides of a coin but exactly because of this contrast, they made a very good team. Their knowledge, patience and ambition has been an invaluable help during these three and a half years. I wish i had at the beginning of this journey the wisdom of today, to better use all their gifts.

I am most grateful, more than i could express here, to the two persons that helped me enormously with the sample fabrication proceeses: Raphael Weil and Michael Rosticher. They, both, have been truly patient and understanding with me. All the results i had during this thesis are due in great part to them. Also, i would like to acknowledge the support i received from the two post-docs i directly worked with: Keisuke Yamada and Shubadeep Datta, who made much easier my permanent "ballet" between two labs and two different research subjects. The same feeling i have for Jean-Yves Chauleau and Cheryl Feuillet-Palma who first introduced me to the subjects i developed in this manuscript.

I must say nanometric scale devices are though to work with. For this reason, i cannot forget the help received from Mathieu Delbecq and Jeremie Viennot with the sample preparation part. Even more, knowing, i am not the easiest person to work with. Also, i have greatly benefited from the generous support of Luc Fruchter and Frédéric Bouquet during my electrical measurements done in Orsay. They, both, entered this project in a moment i was loosing hope on one part of this work.

Audrey Cottet, thank you for all the theoretical work you have done, it helped so much in the understanding of the experimental results, giving that "edge" that all experimental work needs. And because i mentioned experimental results, here i need to mention and express my gratitude also to Olivier Andrieu, who saved the day, in more than one occasion, by providing us with the so-much-wanted-(by everyone)-helium.

Maybe the best part of my thesis represented the oportunity to meet many interesting people. The back and forth between two labs that was needed in the last few years gave me the oportunity to interact with twice as many persons than other students do. I would like, here, to express my apreciation to all the members of both teams i worked with for their guidance and all the pleasant moments spent together. Gwendal Fewe, Bernard PlaÃ§ais and Jean-Marc Berroir, thank you very much for your warm encouragements, given in key moments of this thesis. Alexandra Mougin, Jacques Miltat, Stanislas Rohart, Jean-Pierre Jamet, Vincent Jeudy, Grgory Malinowski and Jacques Ferr i am grateful for the helping hand given with various experiments i had to perform and for the efforts to integrate me in the group. Of great help was the excelent colaboration with Charys Quai and Sylvie Gautier for the metalisations done in Orsay.

Looking behind, i realise that i was truly fortunate people wise. During this thesis i gained some very good friends wit hwhom i shared many pleasant moments. Thank u, Andreas Betz (and lovely Clara) for your tonic company and continuous moral support, Erwan Bocquillon, Jon Gorchon, Jacob Torejon, Quentin Wilmart, Francois Permentier, Vincent Freulon and many others for the beautiful memories you have given me. A special, grateful, wink to Clementine Carbillet, your presence and the discussions we had during our usual runs really made a difference in tough moments.

And last but not least, i want to include on this list also to the people outside the labs that believed in me and encouraged me during this thesis. Here i need to mention my family who encouraged me from afar and my friends that sometimes traveled long distances to be next to me or that shared many hours and cups of tea with me. I will open this list with Alex, my best friend and my flatmate during all this time and then i will continue with Ieva, Lars, Cristina and Adrian, Anxi, Becky and Andreas, Jeremy, Riad, Dita, Alina, Ioana, Szonja, Olimpia, Alan, Catalin, Ibtissem, Ramona ... and i would better stop here even if i could go on like this for another half a page.

Thank you, everyone!

Contents

List of Figures

Chapter 1

Introduction

Electronics represents a corner stone for our modern technology. With the recent development of nanotechnology, people eventually became able to access the adequate length scale to closely investigate the spins and the wide interest and large prospects of using the electrons spin degree of freedom in new generation electronic devices have lead to a vibrant field dubbed spintronics.

In this work, we present experiments in the field of spintronics that combine two very promising materials: single wall carbon nanotubes (SWCNTs) and palladium nickel (PdNi), a tunable ferromagnet, with the purpose to manipulate the electronic spin both in the classical and in the quantum regime. Carbon nanotubes (CNTs) are carbon cylinders of a few nanometers in diameter and up to several millimeters in length. They were discovered by Sumio Iijima in 1991 [1] and they have attracted a lot of interest because of their exceptional electronic and mechanical properties. CNTs have been applied as FETs in logic circuits, and have been also proposed for other electronics applications. More recently, also spin injection and transport in CNTs came under intense scrutiny. The combination of high charge mobility, negligible spin-orbit coupling and weak hyperfine interaction holds the promise of very long spin relaxation times.

Pd_xNi_{100-x} (where x represents the atomic concentration, in percent) alloy also attracted considerable attention as ferromagnetic electrodes in carbon based spin valves. Its excellent contact properties on carbon nanotubes (CNT), lead to low resistance contacts (transparent) [2], while its ferromagnetic behavior provides the means for spin injection. Surprisingly in the case of CNTs a tunneling barrier between the PdNi and the CNT itself seems not to be an indispensable ingredient for spin injection. In fact the anisotropy of the alloy plays an important role since the successful demonstration of spin injection is based on the observation of a giant magnetoresistance (GMR) effect, determined by the relative orientation between the magnetization of the ferromagnetic electrodes. In carbon-based spin-valve devices the planar arrangement of the system complicates the realization of non-collinear magnetizations, and the ability to control the magnetization direction with respect to the plane of the electrode which is an essential factor in the evolution of the system. For this, a good knowledge of the magnetic properties of such ferromagnetic alloys when lithographically patterned into

narrow electrodes.

Manipulating spin or magnetization requires to apply a torque via a real or an effective magnetic field. Not so long ago it was shown that spin polarized current is another possibility to achieve the same results thanks to the spin transfer torque phenomenon [7]. So far, the spin transfer torque has been intensely studied in systems (nanopillars [11], magnetic stripes [45] etc) exhibiting a classical, essentially diffusive, transport mechanism. In this context, the question to ask is: what happens when these classical conductors are replaced by quantum ones such as nanowires or quantum dots. The immediate interest in such systems, beside the fundamental phenomenology involved is a new generation of electronic devices where the spin transfer torque dominates over heating and/or Oersted field effects.

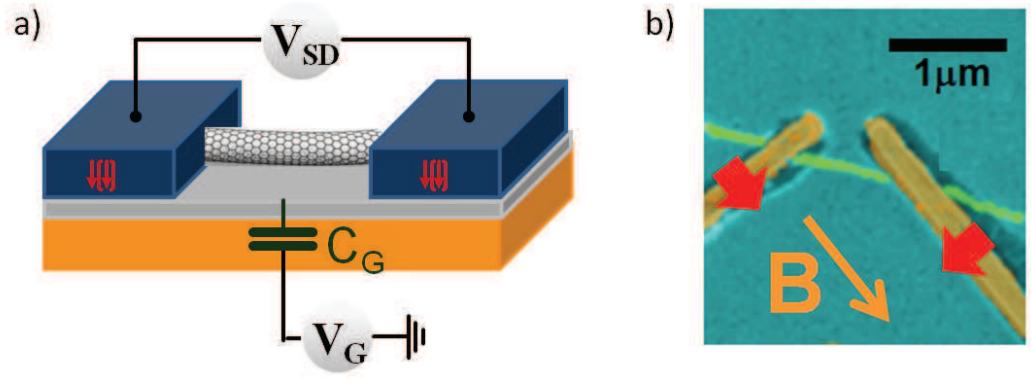

Figure 1.1: *(a) Schematic view of a CNT based quantum dot: two metallic leads (source and drain) are evaporated on the CNT; the nanotube is capacitively connected to a gate voltage while a source-drain tension is used to vary the chemical potential of the electrodes; (b) SEM image of a typical sample in false colors. The red arrows indicate the direction of the magnetizations. A back gate electrode (not visible) is used to tune the energy levels of the device. As shown by the orange arrow, the external B-field is applied along one of the easy axis of the two PdNi strips. A bias voltage (not visible) is used to tune the electrochemical potentials of the electrodes.*

The control which is generally offered when scaling down to nanometric dimensions allows one to achieve new functionalities with high potential, as it is the case of the spin field effect transistors [35], [38]. So far, results of such a high potential have been demonstrated only for collinear geometry-based systems, where spin transport can be described using a single quantization axis. Still, magnetoelectronics devices exploiting actively the electronic spin, meaning a total control over classical or quantum spin rotations have not been achieved so far.

Here we implement a quantum dot connected to two non-collinear ferromagnetic leads forming an angle of $\theta = \pi/2$, schematically presented in fig. 1.1, (a). The device we propose acts like a spin-valve device. A finite tunneling magnetoresistance effect is to be expected. in fig. 1.1, (b) one can see a SEM image of a typical sample in false colors. The red arrows indicate the direction of the magnetization of the two leads. A back gate electrode (which is not emphasized in the image, see fig. 1.1, (a)) is used to tune the energy levels of the device. As shown by the orange arrow, the external magnetic field, B, is applied along the easy axis of one of the PdNi stripes.

1.1 Main results

1.1.1 PdNi anisotropy

For a better understanding of the magnetic switchings taking place in such a device and also for optimizing its electronic properties, a detailed understanding of the magnetic characteristics of Pd_xNi_{100-x}, alloy becomes crucial. During this work we studied PdNi alloy nanostripes by means of extraordinary Hall effect measurements on lithographically patterned crosses (see fig. 1.2) by varying the chemical composition of the alloy, its thickness and the capping films used to impede oxidation.

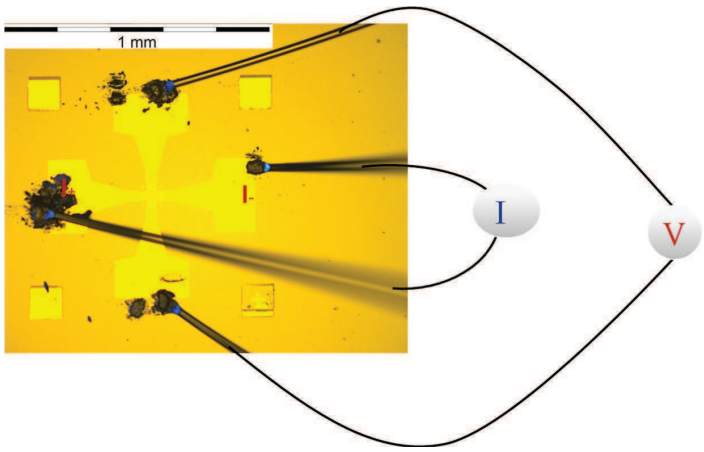

Figure 1.2: *Optical image of a typical Hall cross; the PdNi crosses are connected to Au pads further contacted using a microbonding machine to the sample holder; the principle of a 4-points electrical measurement is exposed in the image: we measure the voltage difference V while applying an electrical current between the I_+ and I_- terminals.*

The results presented here were measured on samples having 40 μm in width and a length of 100 μm. We investigated also nanometric sized samples with 300 nm in width and 2 μm in length. The thickness of PdNi varied between 5 and 15 nm. Capping layers of aluminium, palladium and samples without capping were probed. All samples

were fabricated on a Si substrate and structured via electron beam lithography. The deposition of the thin films was done using evaporation techniques. Gold (Au) leads are attached to the PdNi crosses as contact pads for electrical measurements; small Au crosses are used to align the patterns during the various steps of lithography. The study focused on $Pd_{20}Ni_{80}$ and $Pd_{90}Ni_{10}$.

A first question we wanted to anwser to regards the influence that the proportion of Pd in PdNi alloy has on the anisotropy of ones' samples. For that, both, $Pd_{90}Ni_{10}$ and $Pd_{20}Ni_{80}$ were investigated. Measurements performed on $Pd_{20}Ni_{80}$ for temperatures between 10 K and 140 K in a field sweeping between -9 T and 9 T show a saturation field between 100 and 200 mT that increases with the increase of the temperature and a lack of remanent magnetization. This testifies for the in-plane magnetization alignment of the sample, even at the lowest temperatures.

The hysteretic curves for $Pd_{90}Ni_{10}$, in the same interval of temperatures, show an evolution from in-plane to out-of-plane magnetization at around 60 K. An increase in the coercive field with the decrease of temperature is emphasized.

An important aspect when considering the transition from $Pd_{20}Ni_{80}$ to $Pd_{90}Ni_{10}$ is lower magnetization of the later alloy (average atomic moment $\mu = 0.6$ B for $Pd_{20}Ni_{80}$ while $\mu = 0.25$ B for $Pd_{90}Ni_{10}$ as Fischer et al reported [43]), thus a smaller demagnetization energy for the $Pd_{90}Ni_{10}$. On the other hand, magnetostriction initially increases with the increase of the Pd percentage in the compound. So, when analyzing $Pd_{90}Ni_{10}$ we have a smaller demagnetization while more anisotropy in the system thus a bigger chance to observe an out-of-plane magnetization.

For $Pd_{20}Ni_{80}$, this experiment is a first at low temperature and results show that the magnetization remains in plane even at $T = 10$ K This translates into a small stray magnetic field exerted by the material which is very helpful in constructing small size spin valve devices with ferromagnetic leads. Indeed, the result is very helpful for the second part of this work, the one concentrated on quantum spin valve effect since an in plane magnetization translates into a small stray magnetic field exerted by the electrodes.

Also a comparison between the Curie temperature of the two alloys: about 120 K for $Pd_{90}Ni_{10}$ while for $Pd_{20}Ni_{80}$ this is well above room temperature (reported at 600 K by Ferrando et al [40]) offer an obvious facility in the case of $Pd_{20}Ni_{80}$ to use further room temperature techniques for a more thorough investigation. Following these results, in our CNT based spin devices, we used a Ni-rich alloy for the electrodes connecting the CNT, due to the in-plane orientation of the magnetization that produces a small stray field.

Extraordinary Hall measurements confirm previous experiments [3], [4] that showed a preferential direction of high aspect ratio PdNi contact strips, with a magnetically easy axis transverse to the strip orientation. Furthermore, we provide experimental proof for the model proposed by Chauleau et al who interpreted this magnetically easy axis, transversal to the strip orientation as a consequence of the stress/strain relaxion at the strip edges. While a perpendicular component magnetization effect was also recorded for the core of the stripe, according to Chauleau et al the edges remain transverse.

Further measurements show that geometry, thickness and the choice of capping layer used to protect the PdNi against oxidation, are all key parameters when choosing the right characteristics for a spin-based device. Measurements done on nanometric sized Hall crosses show a out-of-plane component of the magnetization at small temperatures (below 40 K), but less than in the case of the micrometric samples. This is due to due to the stress relaxation at the edges that becomes important, in relative terms, in such small devices.

1.1.2 Non-collinear magneto-electronics/Spin dependent transport in quantum dots

An important factor in quantum dots physics, due to the spatial confinement of electrons, is the (Coulomb) electron-electron interaction. The tunneling of electrons from the ferromagnetic electrodes to the island is strongly influenced by the Coulomb charging energy of the QD. Tunneling of an electron into such an island increases the electrostatic energy of the island by the charging energy $E_C = e^2/2C$, where e represents the electronic charge and C is the total capacitance of the QD.

When speaking about electron tunneling we need to consider the transparency of the contacts between the CNT and metallic leads. In samples with low contact transparency, a pronounced Coulomb blockade is observed, where single-electron conductance peaks are separated by broad valleys of vanishing conductance. To observe Coulomb blockade regime, thus discrete charges inside the QD, one needs that the transmission events between the leads and the island are much smaller than one.

In the case of a more transparent contact between the island and the leads, we can speak about a Fabry-Perot transport regime which is the electronic analog to the Fabry-Perot interferometer. In this regime, the electronic interactions can be neglected.

Measurements presented in this section were performed on CNTs connected to fer-

romagnetic electrodes, of nominal composition $Pd_{30}Ni_{70}$, 45 nm thick, covered with 5 nm of Pd. The conductance measurements are done using a standard lock-in detection technique. Each magnetoresistance plot was obtained by averaging 4 times single curves, all displaying a hysteresis switching. The external magnetic field is applied along the direction of one of the electrodes and thus perpendicular to the second one to ensure the maximum effect differences while swept between $\pm 0.4\ T$.

1.1.3 Coulomb blockade transport regime

Transport measurements revealed a Coulomb blockade transport regime, confirmed by a color scale differential conductance map of the device (see fig 1.3) as a function of the source-drain bias V_{SD} and the gate voltage V_g for the transport spectroscopy over a wide range of voltages. The color scale plot displays specific Coulomb diamonds characteristic to the spectroscopy of a quantum dot. The mean level spacing variate with the gate region: from smaller in the gate region displayed ($< 1\ meV$), to substantially larger (about 3 meV) for more positive values of the gate.

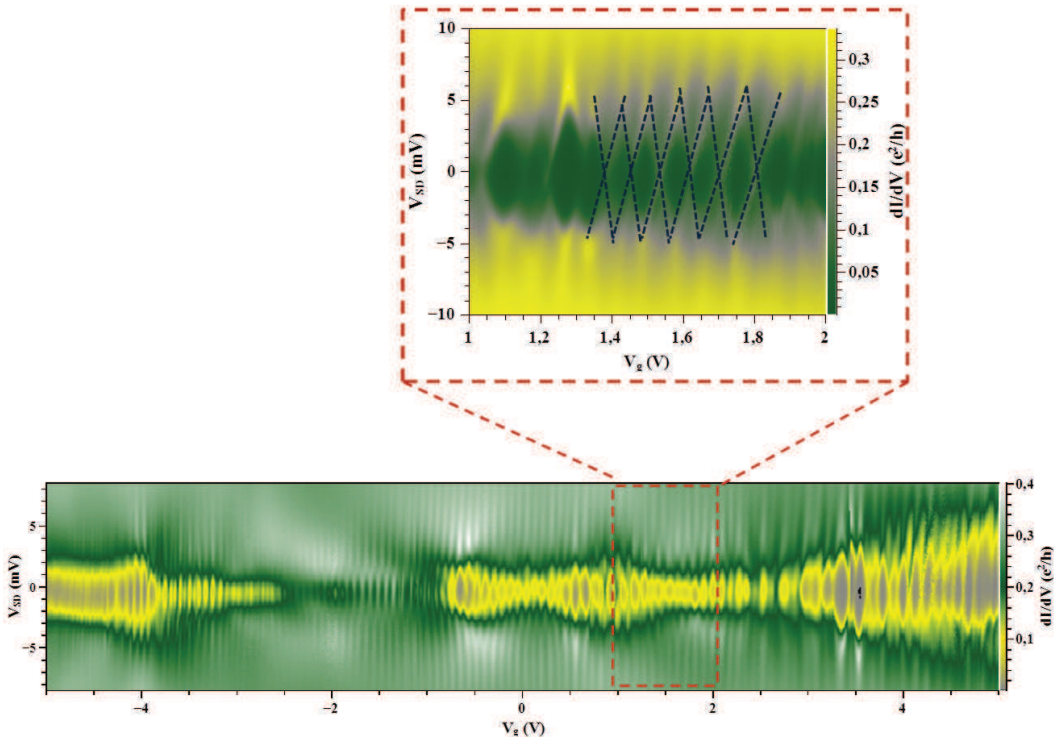

Figure 1.3: *Color scale differential conductance spectroscopy of the device as a function of gate voltage, V_g (over a wide range), and source-drain bias, V_{SD}. Characteristic Coulomb diamonds are displayed. Experimental temperature is* 1.8 K.

The sample was further tested in both linear regime (in the absence of a source-drain voltage) and non-linear one. In linear regime, results show a typical TMR signal when placed under the sweeping field, behavior specific for a spin-valve device. The hysteretic switchings are symmetric with respect to the 0 external magnetic field and correspond to modifications in the relative magnetization of the electrodes.

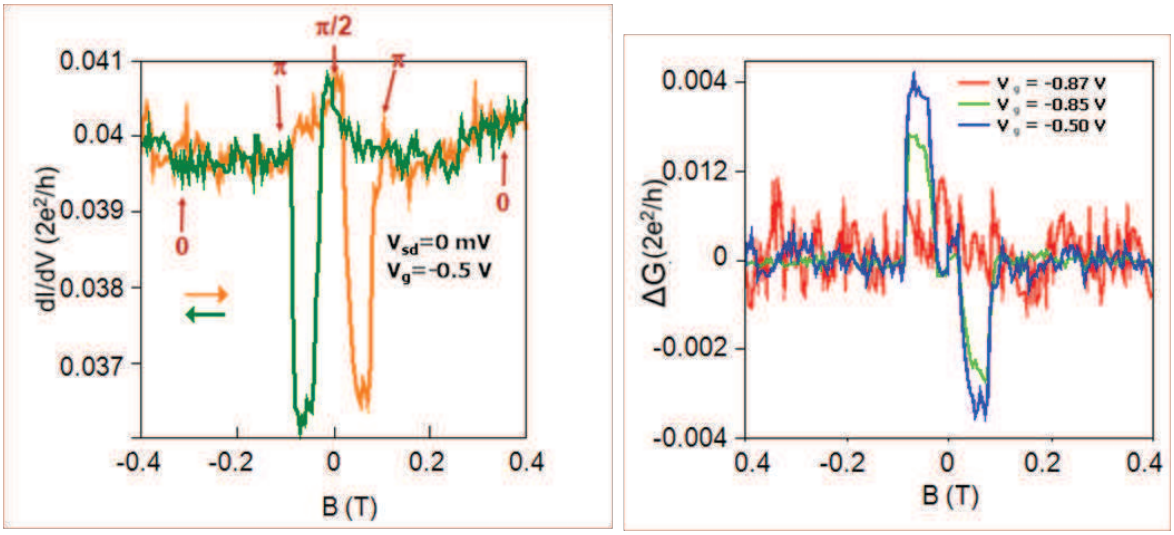

Figure 1.4: *Gate effect on magneto-resistance* (a) *Single magnetoresistance curve for* $V_{sd} = 0\ mV$ *and* $V_g = -0.5\ V$*. The orange curve corresponds to increasing magnetic field* (G_{trace})*. The green curve corresponds to decreasing magnetic fields* ($G_{retrace}$)*.* (b) *Variations of the jumps magnitude* ($\Delta G = G_{trace} - G_{retrace}$) *were observed for different values of* V_g *.*

Plots of the conductance, dI/dV, as a function of V_g show a clear high conductance for negative gate voltages. In fig. 1.4, (a), it is displayed a typical hysteretic swich registrated for a gate voltage: $V_g = -0.5\ V$ where is indicated also the evolution of the relative angle between the magnetizations of the two ferromagnetic electrodes. The first switch can be translated as the return of the magnetization in one of the leads leading to the relative degree between the two magnetization of $\theta = \pi$. The second switching event is attributed to a modification of the angle θ from π to 0. If one defines the amplitude of the hysteresis, ΔG, as the difference in conductance upon increasing the external magnetic field, G_{trace}, and decreasing the external magnetic field, $G_{retrace}$, then as it can be seen in fig. 1.4, (b), for different gate voltages ($V_g = -0.87\ V$, $V_g = -0.85\ V$ $V_g = -0.5\ V$) the jumps magnitude changes.

The TMR signal oscillates with the gate voltage due to the quantum behavior of the nanotube connected to the leads. The oscillations of the TMR stem from quantum interferences phenomena as well as interactions taking place inside the device.

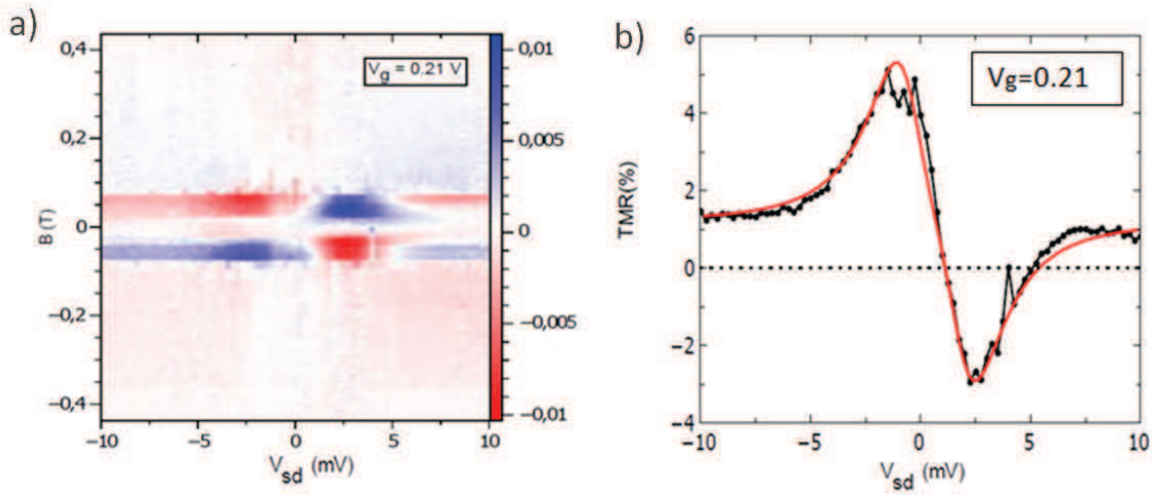

Figure 1.5: *(a) Wide range gate voltage variation of the spin signal* $\Delta G = G_{trace} - G_{retrace}$ *in color scale as a function of the magnetic field,B, and the source-drain* V_{SD}*.* $V_g = 0.21\ V$*; (b) Black line - linear conductance measured simultaneously with the spin signal, red line - prediction of the proposed model with appropiate parameters.*

In the non-linear regime the hysteresis signal (the spin signal $\Delta G = G_{trace} - G_{retrace}$) measured on a wide source-drain voltage range as a function of the magnetic field, B, for a gate voltage $V_g = 0.21\ V$ (displayed in fig. 1.5, (a)) it can be identified a change of sign as the bias changes from positive to negative values. Also the TMR displays a nearly anti-symmetric behavior around the 0 magnetic field point (see fig. 1.5, (b)). Measurements done for different values of the gate voltage account for the non triviality of this behavior. Comparison of the expermental data with calculations supports the hypothesis of an interplay between spin accumulation phenomena which tends to force the spin inside the dot to follow the symmetry of the current and spin relaxation that acts against it, a precession of the spin inside the QD (see schematics in fig. 1.6) is taking place.

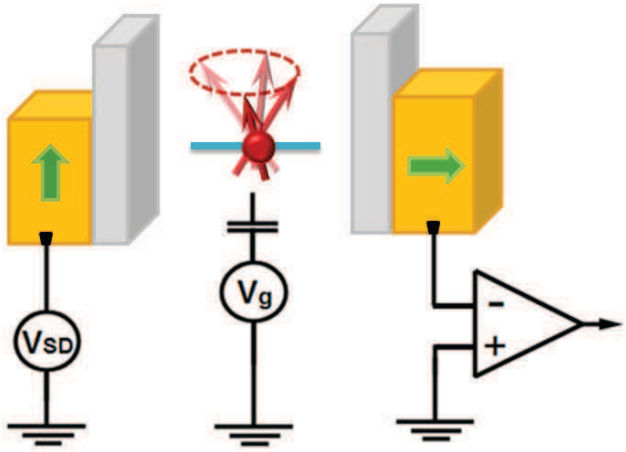

Figure 1.6: *Illustration of the phenomenological behavior of the device. A single active energy level carries a single spin which can take in principle any direction since it is controlled by non-collinear electrodes. A concurential behavior between spin accumulation phenomena which tends to force the spin inside the dot to follow the symmetry of the current and spin relaxation that acts against it, determine a precession of the spin inside the QD.*

1.1.4 Fabry-Perot transport regime

Colorscale plots of the conductance as a measure of the source-drain and gate voltages confirm the chessboard like pattern specific to the Fabry-Perot physics. The spacing between the centers of two adjacent rhombs gives access to the spacing of the energy levels inside the quantum dot (QD) which is, experimentallly, determined by, L, the length of the nanotube: $\Delta E = hv_F/L$. In our case the spacing between rhombs is 5 mV as highlighted in fig. 1.7, (a), using orange dashed lines and it is consistent with the lithographically defined length of the nanotube which is about 600 nm.

Measurements performed in the linear regime were used to characterize the spin transport in the absence of a source-drain voltage. The signal registered has a hysteretic evolution, with the switchings indicating modifications in the magnetization of the PdNi leads. Measurements done on a large interval of gate voltages show consistent variations in the jumps magnitude up to 4 %.

A striking result obtained here in presented in fig. 1.7, (b). A similar hysteretic curve was obtained in out of equilibrium transport regime for multiple gate voltages values. The hysteretic signal shows magnetization reversal in the electrodes taking place before the external magnetic field applied changes sign. The phenomena was studied both when the field increases and decreases.

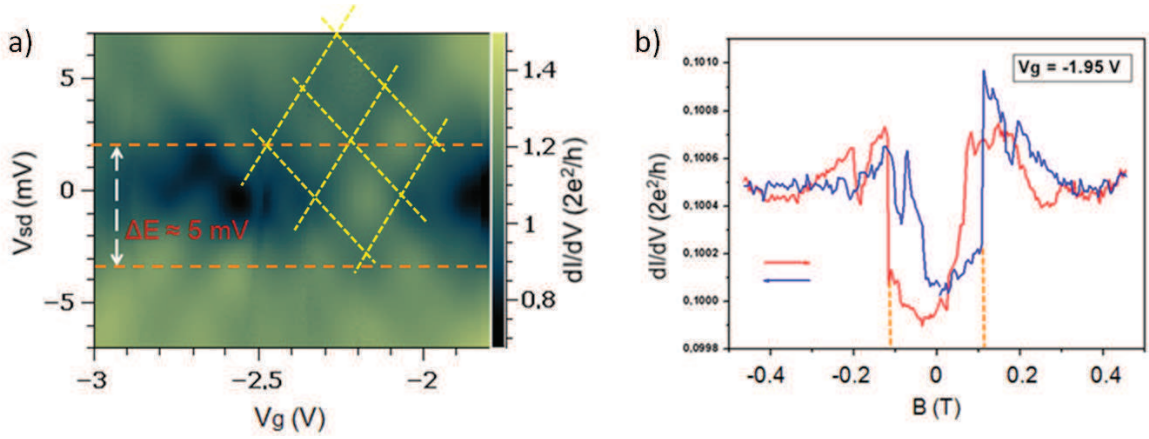

Figure 1.7: (*a*) *Color scale differential conductance spectroscopy of the device over a wide range of source-drain bias* V_{SD} *and gate voltage. Characteristic chessboard patters - highlighted by the yellow dotted line, specific to Fabry-Perot physics. Experimental temperature is* 1.8 K. (*b*) *Single magnetoresistance curve for* $V_g = -1.95\ V$. *Magnetization reversal before the external field changes sign.*

While it is too early for a final conclusion on the nature of this result, this preliminary work may suggest a transfer torque that "helps" the external applied field to switch the magnetization inside the two ferromagnetic PdNi leads. This result is even more important since it represents a first in such type of structure. Nevertheless more investigations need to be pursued to present a final picture of the phenomenology involved.

Chapter 2

Non-collinear magneto-electronics/Spin dependent transport in quantum dots

2.1 Spin transfer torque

In an era of information and communication, there is a high interest towards new technology related to the interaction with the information. Therefore, research branches bound to generate a better organization, storage, transmission and reading of the information are all in the focus of the scientific community.

Spintronics is the field in which the accent falls on exploiting both the intrinsic spin of the electron and its associated magnetic moment, in addition to the fundamental electronic charge. The discovery of giant-magnetoresistance (GMR) by Fert et al. [5] and Grunberg et al. [6] in 1988 became the monumental moment that spin transport came into mainstream.

2.1.1 The evolution of magneto-electronics

Electrons, as charge carriers, have a property known as spin which is an angular momentum intrinsic to the particle. The quantum mechanical nature of the spin determines that an electron can be described using only two states, with the spin pointing either "up" or "down" (the choice of up and down being arbitrary). An electrical current passing through a macroscopic, non-magnetic conductor is unpolarized due to the fact that spins are randomly oriented.

Things change when ferromagnetic components are incorporated into electronic devices. The particularity of the ferromagnetic materials is that the electron's magnetic dipoles are aligned in the same direction, their individual magnetic momentum added together creating a measurable macroscopic magnetic moment. In materials with a

filled electron shell, the total moment of the electrons is zero because the spins are in up/down pairs. Only atoms with partially filled shells (i.e. unpaired spins) can have a net magnetic moment, so ferromagnetism only occurs in materials with partially filled shells. Ferromagnetism involves an additional phenomenon, though: the dipoles have to align spontaneously, giving rise to a spontaneous magnetization, even when there is no applied field.

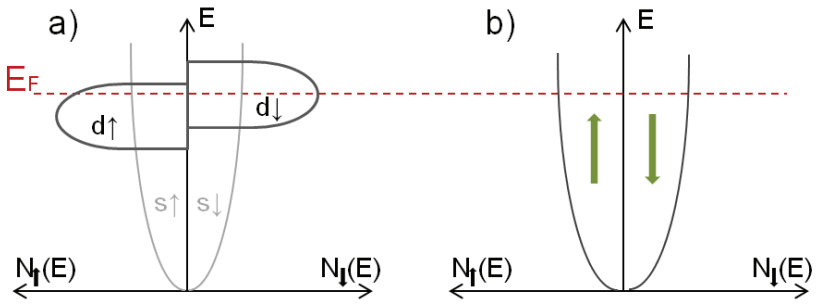

Figure 2.1: (*a*) *The structure of the density of states in the conduction band for majority spin* (↑) *and minority spin* (↓) *in a ferromagnet;* (*b*) *density of states for the free electrons for a non-magnetic material*

Using magnetic engineering, the intrinsic bistability of the ferromagnet materials was used to construct device elements with multiple magnetic states. To gain control over both the output/input of such elements, these magnetic states must be converted into something that can be easily manipulated, e. g. voltage or current. Due to spin-based interactions between the ferromagnets and electrons, the orientations of the magnetization for ferromagnetic elements can determine the amount of current flowing through the system. The reverse phenomena in which we can control and vary the orientation of the ferro's magnetization become also possible.

A good method to do so, is to exploit the spin state of the conduction electrons. In fig. 2.2, one can see how electrical current can be used to detect the magnetic state of a ferromagnetic element (F) [7]. We contact the ferromagnet with a normal conductor N and the entire system to a current source. We consider the magnetization of the ferromagnet to be uniformly orientated to the $+x$ axis. The magnetic moments of the conduction electrons in the ferromagnet are aligned along the axis of magnetization.

The current crossing the F/N interface will be composed by spin-polarized electrons that can diffuse on quite long distances into the non-magnetic material before having their spin orientation randomized. Johnson and Silsbee [8] first reported diffusion lengths of 1 μm for spins injected from a ferromagnet into an Al film at low temperature. Spin state of the electrons injected in N is linked to the orientation of the magnetization of F. These electrons move around diffusely carrying this marker,

the spin orientation. They can be described as spin-polarized conduction electrons. Conventionally, we denote the electrons having their spin oriented along the $+x$ axis as having a spin-up while those pointed towards -x are called spin-down carriers. The conduction electrons of the normal element, N, are not spin-polarized.

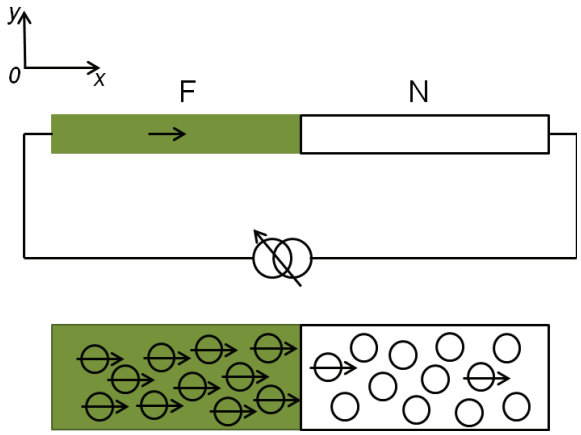

Figure 2.2: *Heuristic picture of spin and charge transport in a ferromagnetic/nonmagnetic, F/N, system.*

A second ferromagnet $F\prime$ is used as drain. We create thus a sandwich structure, called a spin valve, in which we place a nonmagnetic material N between two ferromagnetic ones: F acts as spin injector and $F\prime$ fulfills the role of spin analyzer. We consider that F and $F\prime$ can be controlled separately. If the two ferromagnets have parallel magnetization and orientation, the spin-polarized carriers are driven from F through N and then to $F\prime$ with relative ease. If the magnetization are antiparallel, then the spin current generated through the structure is small, due to the high resistance of the system. A more extensive explanation of this phenomena is given using Julliere's model in section 2.1.5.

If we consider the magnetization of F as being fixed and we vary only the magnetization of $F\prime$, then the structure we just depicted, $F - N - F\prime$, represents a model of memory cell in which the output is evaluated through the reading of the electrical resistance of the device given by the alignment of the two magnetizations. More generally, the method presented above represents the way the spin state of an electron can be directly accessed through it's electrical charge, becoming thus a controlling parameter that can be used to obtain new functionalities for a device. In a similar way, other properties associated to the magnetic state (like magnetostriction) can be used as control parameters.

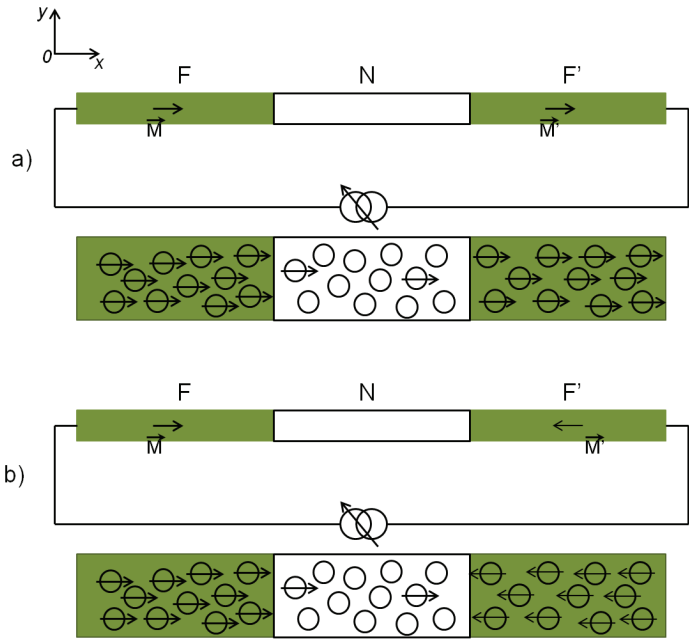

Figure 2.3: *Heuristic picture of spin charge transport and spin current detection in a ferromagnetic/non-magnetic/ferromagnetic, F/N/F′, system.*

An aspect of great interest is that the spin current flows through an interface even at zero applied bias, if the magnetizations of the two ferromagnetic layers are non-collinear; the source of the exchange coupling can be understood as the transfer of angular momentum from this spin current to each magnetic electrode. In this case, the current doesn't merely respond to the magnetization of the layer but actually alters it. When an electron, with misaligned spin, passes from a non-magnetic into a magnetized material, the mismatch gives rise to a small twisting force - a torque - between the electron and the magnet.

In fig. 2.4 it can be seen how at a non-magnetic/ferromagnetic interface, by means of conservation of angular momentum, the ferromagnetic material absorbs the transverse component (with respect to its own magnetization) of the angular momentum of an incoming electron, which acts on the magnetization of the material as a torque. At the same time, the parallel component of the angular momentum is reflected back into the normal conductor. A large current generated like this can in principle shift the magnetization direction of the material that it is passing through.

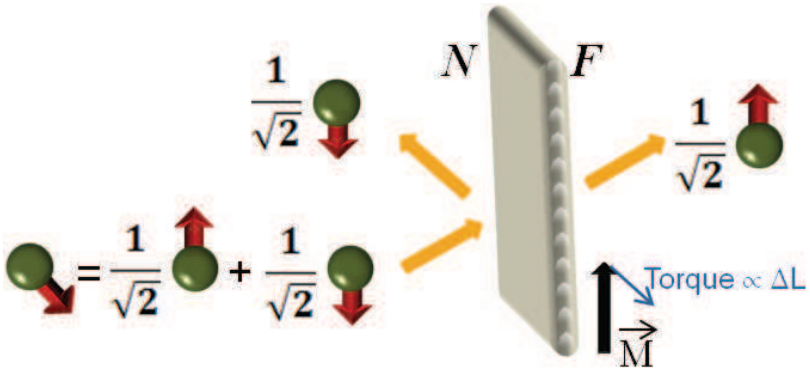

Figure 2.4: *Illustration of the magnetization torque exerted by a spin current at a non-magnetic/ferromagnetic metal interface. The magnetization of the ferromagnet is normal to an incoming electron that can be written as a linear combination of the "up" and "down" spin states. Assuming that the interface is transparent only to the spin having the same orientation as the magnetization, M, of the ferromagnet, the parallel spin and charge currents are conserved, whereas the transverse spin current is absorbed and acts as a torque on the magnetization.*

Some very important papers, launching the study of spin transfer torques appeared in 1996, when Slonczewski [9] and Berger [10], independently, showed that current flowing perpendicular to the plane in a metallic multilayer can generate a spin transfer torque strong enough to reorient the magnetization in one of the layers.

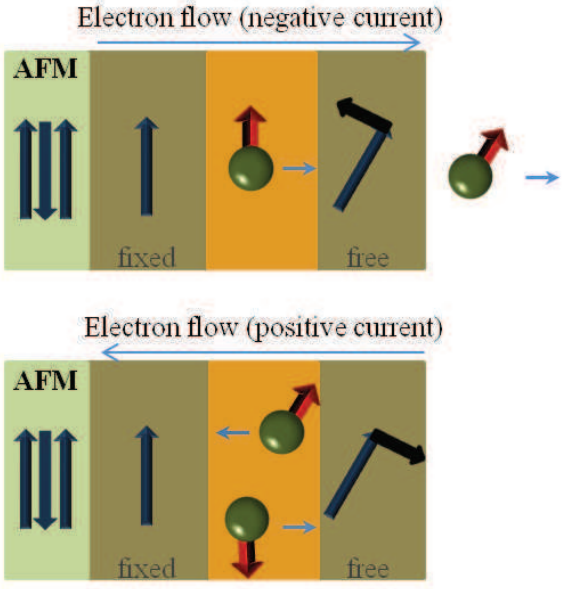

Figure 2.5: *Simplified illustration of the direction of the spin torque for both current polarities in a typical metallic spin valve structure.*

Slonczewski predicted that the spin transfer torque from a direct current could trigger two types of magnetic behaviors depending on the design of the device and the magnitude of an external applied magnetic field: either simple switching from one static magnetic orientation to another or a dynamical state in which the magnetization undergoes a steady-state precession.

In the case of a typical spin valve, with one layer pinned by an exchange bias - see fig. 2.5, we can focus on the spin transfer torque experienced by the free layer. The direction of the spin transfer torque depends on the polarity of the current flow. Positive current (electrons flowing from free layer to fixed layer) promotes anti-parallel alignment between the two ferromagnetic layers, while negative current (electrons flowing from fixed layer to free layer) favors parallel alignment.

Spin transfer torque (STT) in classical conductors has been already extensively studied. Most of the studies have been carried out on spin valve or magnetic tunnel junction structures patterned into nanopillars. For example, Myers et al [11] studied STT in Co/Cu/Co sandwich nanopillars, with many transversal transport channels and used it to verify that an applied current on the structure can switch the orientation of the magnetic electrodes.

2.1.2 The spin field effect transistor

An important brick to todays spintronic devices is the spin field effect transistor (SFET) proposed in 1989 by Supriyo Datta and Biswajit Das [12] that exemplifies very well, still, the relevance of electrical control over the magnetic degrees of freedom as means of spin modulating charge flow. The physical basis for this proposal relies on gate controlling the strength of the Rashba effect (demonstrated by de Andrada e Silva et al. [13]) in a one-dimensional conductor. In other words, in a confining potential (surfaces, asymmetric quantum wells, etc), the spin-orbit coupling may result in a spin splitting of electron states, which has the nature of the so-called Rashba effect [14]. This splitting can be tuned using an additional electric field opening up a pathway for realizing electric-field spin manipulation [15], [16].

In the Datta-Das device (see schematics in fig. 2.6), the current is modulated using the Rashba spin-orbit coupling (SO) between the spin of the polarized current inside the semiconductor material. The electric charge is introduced through an injecting electrode and collected via a drain electrode. A gate is used to generate an electric field that tunes the value of the effective magnetic field, $\overrightarrow{B}_{SO}$, through which the source-drain current can flow. This results in a very small electric field being able to control large currents. The effective magnetic field acting on the spin of an electron moving at velocity v in a region where an electric field E exists, reads (special relativity):

$$\overrightarrow{B}_{SO} = \frac{1}{c^2}(\overrightarrow{v} \wedge \overrightarrow{E}) \tag{2.1}$$

The novelty of the this system, whose principle has been studied recently in a structure using indium-aluminum-arsenide and indium-gallium-arsenide by H. C. Koo et al [17], is the conduction channel for two-dimensional electron transport between the ferromagnetic electrodes. The electrons can travel between the two electrodes ballistically, if the channel length is small enough. One electrode acts as an emitter, the other a collector (similar, to the source and drain principle described above for the field effect transistor).

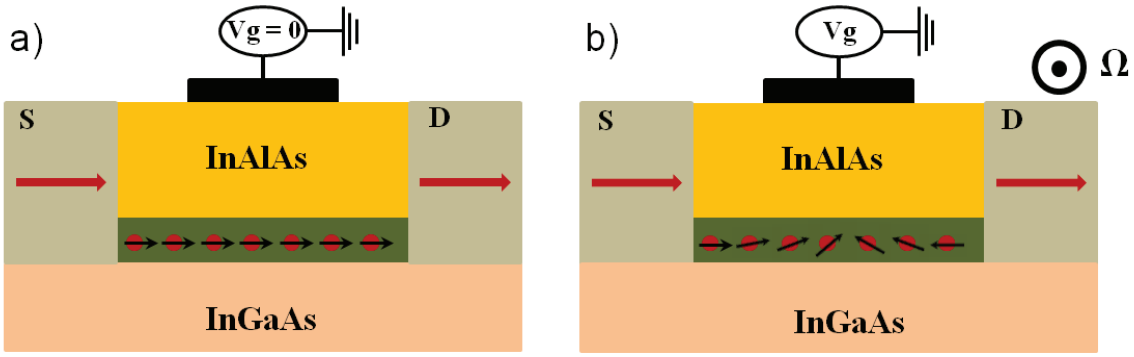

Figure 2.6: *Illustration of the Datta - Das SFET [12]. A quasi-unidimensional transport channel is connected to two magnetic contacts that serve to inject spin polarized current and detect its orientation. A gate voltage is used to produce a magnetic field that controls the precession of the spins of the electrons during their motion between the two electrodes.*

The structure works analogously to the optical polarizer/analyzer system. The source electrode emits electrons with their spins oriented along the direction of the electrode's magnetization, while the collector filters the electrons having the same spin orientation as the magnetization of the electrode. If no changes occur to the spins of the electrons during the transport between the two electrodes, then all the electrons pass through the collector. A gate electrode is used to produce a field that makes spins of the electrons traveling from one electrode to the second to precess. Using this field it is possible to effectively orient the spin of the electrons passing through the conduction channel according to one's needs. The electron current is thus tuned using the degree of precession of the electron spin induced by the gate field. An electron arriving at the collector passes through it only if its spin is parallel to the magnetization of the electrode, and it is reflected if it is antiparallel to it.

2.1.3 Transport characteristics in nanotubes/nanoconductors

The originality of low dimensional conductors arises from the enhanced importance of the electron-electron interaction and the quantum coherence in the electronic transport. These two characteristics open the door to individual spin manipulation which is a very hot topic related especially to quantum computing but also to the realization of SFETs.

At such small dimensions, the phenomena taking place are of quantum nature, the transport is of the ballistic type and the physics that reunites all that is the mesoscopic physics. The length scale is in between microscopic and macroscopic systems, and bounded on one side by the de Broglie wavelength of the electron, and on the other, by the length scales for various scattering mechanisms that destroy the electron's phase coherence or momentum [7].

Starting from the Datta - Das proposition that allows injection/detection of spins and also electrical control over quantum interference, similar to an optic polarizer-analyzer system.

H. T Man et al [18] presented an electronic device analogue to the Fabry-Perot interferometer based on a single wall carbon nanotube, capacitively coupled to a back gate. The nanotube is contacted with two PdNi ferromagnetic leads with different coercive fields, that function as source and drain. A source-drain voltage is used to control the chemical potentials of the two leads. The magnetic moments inside the electrodes lie in the sample plane.

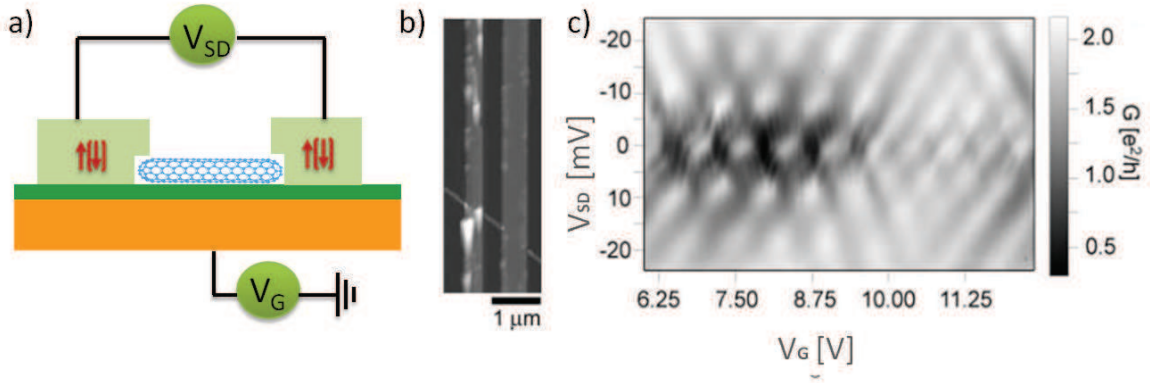

Figure 2.7: (*a*) *Illustration of a carbon nanotube based device. The geometry used is the one of a FET, similar to the Datta - Das transistor: The chemical potentials of the two electrodes are controlled using a source-drain tension. The system is capacitively coupled to a gate voltage applied though the substrate;* (*b*) *AFM image of the device illustrated in image* (*a*) *realized by Man et al [18]. A SWCNT is connected with two PdNi electrodes that act as source/drain system;* (*c*) *The conduction spectrum as a function of the source-drain voltage and gate voltage, measured at* 4.2 K. *The interferometric type of pattern, chessboard like, is given by the different interferences of the electronic waves.*

Measurements performed on this system emphasized the wave nature of the spin polarized electrons. The flow of the electrons is controlled using the source drain voltage and the gate voltage who act on their wave vector; as the wave vector changes during the passage through the nanotube also the phase of the electron changes accordingly. Conductance measurements on this device as a function of V_{SD} and V_G revealed a chessboard like pattern which corresponds to the modulations in transmission acting on the device and which has its origin in the quantum interference of the electronic waves. These results are more thoroughly discussed later on.

In order to speak about mesoscopic physics and ballistic transport, one needs conductive media smaller than the phase-coherence length: ($L << l_\phi$); where the phase-coherence length represents the mean distance between successive phase randomizing inelastic events like electron-phonon, and electron-electron scattering. This characteristic length varies strongly with the temperature which, this way, becomes an important factor of the measurements.

2.1.4 Electron tunneling

To study this device we proposed, we need to discuss the phenomena which allow an electron to quantum tunnel over a classically forbidden barrier. This is an area of physics which is both philosophically fascinating and technologically important.

In classical mechanics, if a free particle is not sufficiently energetic to cross over a potential barrier, it is reflected and it will never appear on the other side of the barrier. In quantum mechanics, the same free particle that encounters a barrier with a higher energy than its own, can be either reflected back into the environment where it came from or will penetrate into the forbidden region and, ultimately, reach a point on the other side of the barrier. This is a consequence of the wave like behavior and it represents the probability different of zero of the particle being detected on the other side (see in fig. 2.8).

To calculate this probability we consider a potential barrier with a δ-function shape [19]. By writing the incident wave to the barrier, the transmitted one and the reflected one and taking into account the continuity limits at the two interfaces of the barrier, one gets the following formulas for the transmission and reflection factors:

$$t_\sigma = \frac{2i\sqrt{k_n k_\sigma}}{i(k_n + k_\sigma) - Z} \tag{2.2}$$

$$r_\sigma = \frac{i(k_n - k_\sigma) + Z}{i(k_n + k_\sigma) - Z} \tag{2.3}$$

where: Z is the height of the barrier, k_n is the momentum of the incident electron and k_σ is the momentum of the outgoing electron. This form of the transmission suggests the following parametrization:

$$t_\sigma = -i\sqrt{T^\sigma} \tag{2.4}$$

$$r_\sigma = e^i \varphi_\sigma \sqrt{1 - T^\sigma} \tag{2.5}$$

where φ^σ is the reflection phase that depends on the spin.

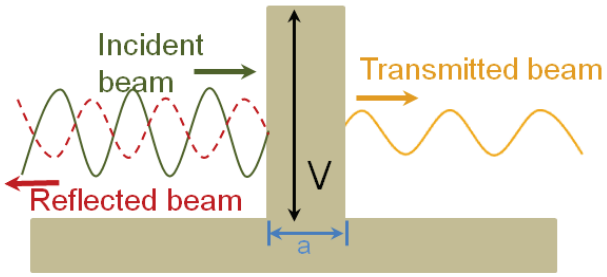

Figure 2.8: *Illustration of a rectangular potential barrier of height V and thickness a. An incident electron falling on the barrier can, according to quantum phenomena, be either transmitted through the barrier or reflected by it.*

2.1.5 Julliere's model

The difference in conductance that appears when electrons are tunneling through a device of the type $F/N/F'$ in which the two ferromagnetic leads have parallel/antiparallel configuration, can be explained by using the model that Julliere [20] proposed, which explains the nature of the magnetoresistance in terms of the fraction between the majority and the minority density of states at the Fermi level. This model does not take into consideration the height or the thickness of the insulating barrier and the magnetoresistance is expressed only in terms of the fraction of majorityy/minority density of states at the Fermi level.

The number of conduction electrons in the electrode L/R (left/right) it is assumed proportional to $N_{1(2)}(E_F)$. The electrodes are separated by a thin tunnel barrier and a small voltage V_{SD} is applied. The number of spin-up conduction electrons (majority electrons or electrons with spin parallel to its magnetization) in the electrode 1 is:

$$N_{1,\uparrow} = a_1 N_1(E_F) \tag{2.6}$$

and in electrode 1:

$$N_{2,\uparrow} = a_2 N_2(E_F) \tag{2.7}$$

where a_e $(e = 1, 2)$ is the fraction of the spin-up conduction electrons in the electrode e:

$$a_e = N_{e,\uparrow}/(N_{e,\uparrow} + N_{e,\downarrow}) \tag{2.8}$$

For parralel magnetizations of the two electrodes, the majority electrons tunnel in electrode 2 into the majority band in electrode 1, and the minority electrons tunnel to the minority band. Thus the tunnel current for majority electrons and minority electrons can be summed up:

$$I_P \propto (N_{1,\uparrow}N_{2,\uparrow} + N_{1,\downarrow}N_{2,\downarrow})eV_{SD} \tag{2.9}$$

and that gives the conductance:

$$G_P \propto N_{1,\uparrow}N_{2,\uparrow} + N_{1,\downarrow}N_{2,\downarrow} \tag{2.10}$$

In the case of antiparallel magnetizations of the electrodes, the majority electrons from electrode 2 have to tunnel into the minority band of the electrode 1 assuming there is no spin flip inside the barrier region. Similarly, the minority electrons have to tunnel into the majority band. If the tunneling currents are summed up, one gets the following formula for the conductance:

$$G_{AP} \propto N_{1,\uparrow}N_{2,\downarrow} + N_{1,\downarrow}N_{2,\uparrow} \tag{2.11}$$

By introducing a_1 and a_2 in the above equations, the conductance can be written:

$$G_P \propto (a_1 a_2 + (1 - a_1)(1 - a_2))N_1(E_F)N_2(E_F) \tag{2.12}$$

$$G_P \propto (a_1 a_2 + (1 - a_1)(1 - a_2)) \tag{2.13}$$

$$G_{AP} \propto ((1 - a_1)a_2 + a_1(1 - a_2))(E_F)N_2(E_F) \tag{2.14}$$

$$G_{AP} \propto ((1 - a_1)a_2 + a_1(1 - a_2)) \tag{2.15}$$

Thus the magnetoresistance of the junction takes the following form:

$$TMR = \frac{2P_1P_2}{1 - P_1P_2} \tag{2.16}$$

where $P_1 \equiv (2a_1 - 1)$ and $P_2 \equiv (2a_2 - 1)$ are the spin polarization P_1 and P_2 of the two FM electrodes. Usually, the resistance (R_P) for parallel alignment of the magnetization of the FM electrodes is smaller than the resistance (R_{AP}) for the antiparallel alignment, resulting in a positive TMR, called normal TMR effect. However an inverse (anomalous) TMR effect is also possible. To fully understand the anormal TMR, a more complex theoretical model it is needed.

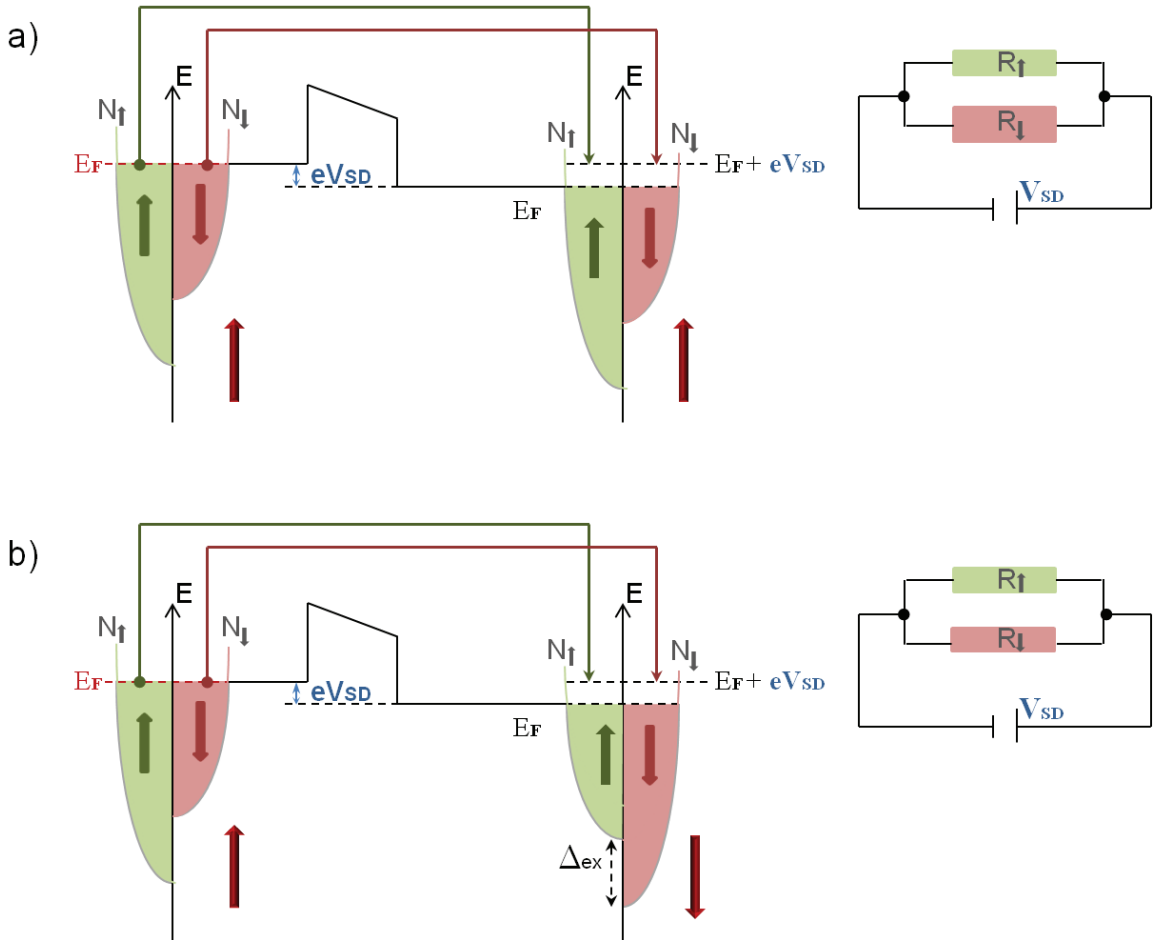

Figure 2.9: *In a F/I/F' junction the resistance is dependent on the relative orientation of the magnetization of the two ferromagnets. The easiest explanation is to compare two cases. In the first case, both electrodes have parallel magnetizations (a). A source-drain voltage is applied and the majority spin (minority spin) electrons will tunnel into the majority spin (minority spin) available states. For the second case, the electrodes have antiparallel orientation magnetization (b). The majority spin electrons must tunnel into a minority spin available state due to the antiparallel configuration and vice versa. The density of states are in this configuration not equal on both sides of the barrier, and thus decrease the conductance (and increase the total resistance of the system).*

2.1.6 Magnetic tunnel junctions (MTJ)

Julliere's model was used to explain the normal TMR effect in MTJ's. This type of device serves as a basis for magnetic detectors and its structure is composed by a barrier, that can be realised for example by using a thin insulating layer, sandwiched between two electrically conducting materials (see fig. 2.10, (*a*)). The magnetic electrodes are assumed to have different coercive fields and electrons are passing through it by the process of quantum tunneling described earlier.

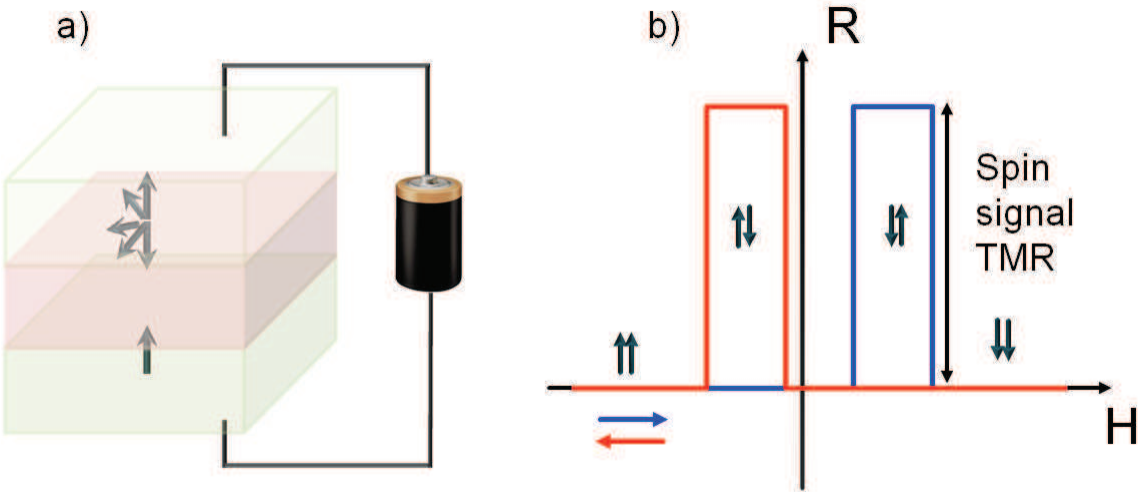

Figure 2.10: (*a*) *Simplified illustration of the direction of the spin torque for both current polarities in a typical metallic spin valve structure;* (*b*) *typical TMR signal in a MTJ in presence of a sweeping external field, indicating a change in the magnetization orientation in the two magnetic layers.*

Having different coercive fields, each of the two magnetizations of the ferromagnets can be controlled individually by using an external magnetic field. When a positive field, $B > 0$, is applied the conductance displays a weak variation with the field; however, when the external field equals the coercive field of the electrode (initially considered antiparallel to the field), the magnetization of the ferromagnet switches; this translates into a jump in the resistance of the system thus also in a conductance vs B representation.

When the magnetic field applies is negative, $B < 0$, the conductance continues to vary weakly with the field as described before as long as no switching of the magnetization takes place; however, for an external field equal to the coercive field of the second electrode, the magnetization of the ferromagnet switches; this translates into a new jump in the conductance of the device. For even more negative values of the external field, the conductance will return to a constant dependence with B. This kind of dependence of the conductance in the presence of the a field is called a hysteresis curve and it is represented in fig. 2.10, (*b*).

The difference between the maximum and minimum values of the conductance, obtained for parallel/antiparallel relative orientation of the magnetizations of the electrodes, give the so called "spin signal". This behavior is in agreement with Julliere's model presented above and that gives the TMR signal of the system:

$$TMR = \frac{\Delta R}{R_P} = \frac{R_{AP} - R_P}{R_P} = \frac{2P_1P_2}{1 - P_1P_2} \tag{2.17}$$

Unfotunatelly, Julliere's model cannot explain some experimental measurements of the magnetoresistance like the ones reported by Suzuki et al [23] and displayed in fig. 2.11, (*b*), which are similar to the one presented by DeTeresa et al [22], [21] and others. The measurements simply exposes a lower resistance in antiparallel configuration of the magnetization of the leads than in the parallel one; situation inverse to what was expected. To explain this "anormal" TMR signal one needs a wider phenomenological image, more precisely, it should be taken into account the spin dependence of the tunneling transmission or its energy dependence.

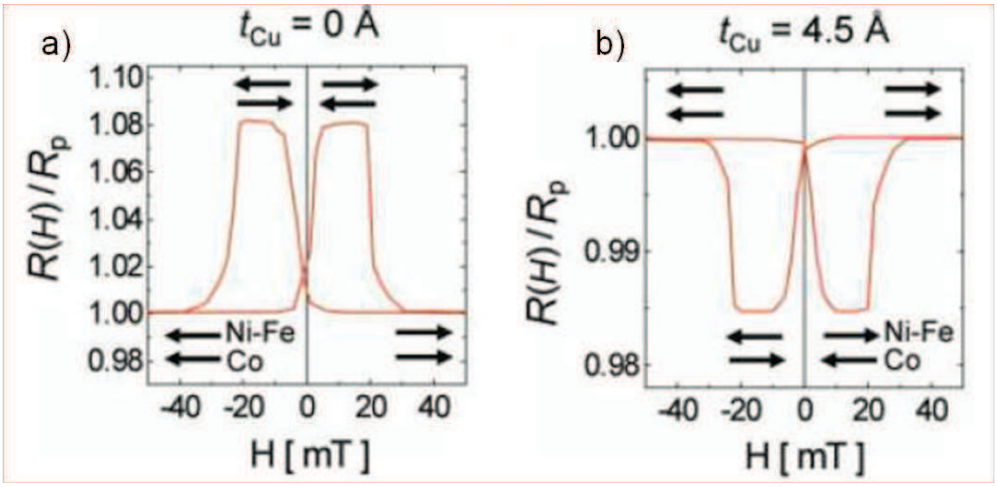

Figure 2.11: (*a*) *Normal hysteretic curve as a function of an exterior magnetic field obtained by Suzuki et al [23] in a JTM; (b) Anormal hysteretic curve registered as a function of an external magnetic field, that accounts for a resistance in antiparallel orientation of the magnetization in the electrodes smaller than the one in parallel configuration, obtained for a different thickness of nobel matal (Cu) than the results presented at point* (*a*).

Slonczewski [24] proposed a more suitable model for such cases, because it calculates the spin current through a $F - N - F$ junction using a second tunnel junction. This model considers the spin current as being responsible for an exchange coupling between magnetizations of the two ferromagnets. Between the two identical ferromagnetic electrodes is assumed a rectangular potential barrier and the tunneling conductance is calculated as a function of the angle between the two magnetization vectors of the leads. All this is expressed using the Schrodinger equation for the wave function of spin-up and spin-down electrons.

Landauer and Buttiker presented a formalism to characterize the electronic transport in the presence of a scattering center in a ballistic conductor [25], [26]. The model

establishes the relation between the wave functions of a noninteracting quantum system and its conducting properties. In fact, the coherence of the electron transport as well as weak electron-electron interaction are essential for the use of this model, because there is no phase-breaking and the quantum interference is preserved during the electron motion across the system.

The initial idea of this formalism was given by Landauer [27] that expressed the conductance of the elastic scatterer using the quantum mechanical transmission coefficient, T. For a system exhibiting spin polarized transport, the conduction can be written as:

$$G = \frac{2e^2}{h} \sum_n T_n \tag{2.18}$$

where T_n represents the n eigenvalues of the transmission matrix product $TT^\dagger$.

This formalism was successfully used by Man et al [18] to describe the behavior of a nano-device based on CNT connected to two collinear ferromagnetic PdNi electrodes having different coercive fields. A source-drain voltage (V_{SD}) is used to tune the polarization of the system while a gate voltage (V_G) is capacitively connected to the nanotube (see fig. 2.12).

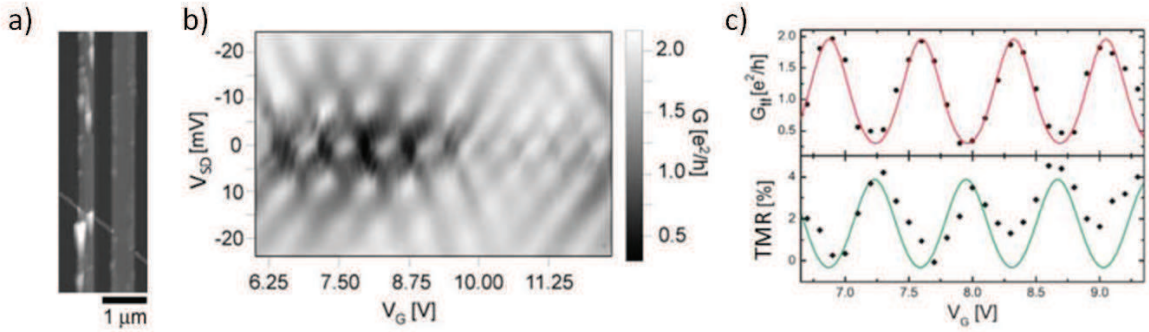

Figure 2.12: *(a) SEM image of a device based on CNT connected to collinear PdNi electrodes with different coercive fields and polarized using a V_{SD}; the CNT is capacitively connected to a gate voltage, V_G. The device is the electronic correspondent of a Fabry-Perot interferometer and it was proposed and studied by Man et al [18]. (b) The differential conductance for the system presented in fig. (a), as a function of the source-drain voltage and gate voltage, measured at 4.2 K. The interferometric type of pattern, chessboard like, is given by the different quantum interferences of the electronic waves. (c) the experimental variation of the conductance $G_{\uparrow\uparrow}$ with the gate voltage for parallel configuration of the leads' magnetizations and theoretical curves of the TMR as a function of V_G, calculated using a diffusive model in non-interacting regime.*

Man, adopted a Landauer-Buttiker picture to describe his device [25]: a coherent quantum conductor connected to two diffusive centers, presented schematically in fig. 2.13 The spin-dependent conductance of an individual SWCNT at zero temperature can then be written using the transmission probability for the majority spin (↑) and minority spin (↓) for the left and right contacts. The electronic wave, traveling between the two scattering centers, suffers multiple reflections and transmissions as a consequence of several scattering events taking place.

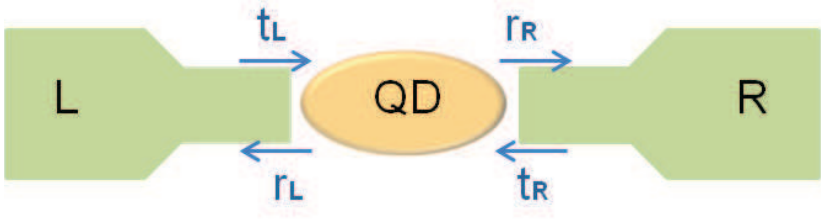

Figure 2.13: *Schematics of the Landauer-Buttiker type of transmission model adopted by Man et al to explain the spin-dependent conductance in a MTJ containing a quantum dot.*

If ϕ represents the phase difference acquired by the electronic wave inside the ballistic conductor as a consequence of these reflections and with $t_{L,R}$ and $r_{L,R}$ the amplitudes of the waves transmitted through/reflected by the right, respectively left

scattering center and with T_i^σ the spin dependent transmission probability through the scatterer, then one gets:

$$t_i^\sigma = \sqrt{T_i^\sigma} e^{i\varphi t_i^\sigma} \tag{2.19}$$

$$r_i^\sigma = \sqrt{1 - T_i^\sigma} e^{i\varphi r_i^\sigma} \tag{2.20}$$

Thus, the total transmission probability of an electron through both scatterers can be written as:

$$T^\sigma = t^\sigma * t^{\sigma\dagger} = \frac{T_1^\sigma T_2^\sigma}{|1 - 2\sqrt{(1 - T_1^\sigma)(1 - T_2^\sigma)} e^{i(\varphi r_(1)^\sigma + \varphi r_(2)^\sigma + 2\phi)}|^2} \tag{2.21}$$

For electrons having an energy close to the Fermi energy (E_F) and a velocity close to the Fermi velocity (v_F), while passing through a coherent conductor of length L, they get a phase difference, ϕ, that can be written as:

$$\phi = L(\kappa_F + \frac{E + e\alpha V_G E_F}{\hbar v_F}) \tag{2.22}$$

For small transmission rates and big rates of reflection, near the resonance one has $\phi - \phi_0 \sim 0$, where:

$$\phi_0 = \frac{\varphi_{r(1)}^\sigma r(1) + \varphi_{r(2)}^\sigma}{2} - \frac{\pi}{2} + n_0\pi \tag{2.23}$$

Now, the transmission factor for σ spin, T^σ can writen as:

$$T^\sigma = \frac{T_1^\sigma T_2^\sigma}{(\frac{T_1^\sigma T_2^\sigma}{2})^2 + (\phi - \phi_0)^2} \tag{2.24}$$

$$T^\sigma(E) = \frac{\Gamma_L^\sigma \Gamma_R^\sigma}{(\frac{T_1^\sigma T_2^\sigma}{2})^2 + (E - E_0^\sigma)^2} \tag{2.25}$$

This is called the Breit-Wigner formula. $\Gamma_{L(R)}^\sigma = \gamma_{L(R)}(1 + \sigma P_{L(R)})$ represents the characteristic of the left(right) contacts between the CNT and the ferromagnetic leads tuned using the $V_{SD=}$ voltage. E_0^σ is the spin-dependent energy level inside the QD that can be modulated using the gate voltage. It can be seen that the total transmission of the system it is in fact tuned by changing the wave vector of the incident electrons. Of course, by doing that, also the phase acquired by the electrons travelling through the system changes.

In this context, the chessboard like conductance obtained by Man et al, see fig 2.12, (b) represent in fact the modulations of the transmission along the system obtained as a result of the quantum interferences taking place for different electronic waves of the incident electrons. The Breit-Wigner equantion 2.25 was also used to explain qualitatively the data presented by Sahoo et al, presented in the Section 2.3.

2.2 Transport regimes

Carbon nanotubes are unique nanostructures that can be considered the prototype of a one-dimensional conduction wire. The fundamental block of carbon nanotubes is an all-carbon cylindrical single wall carbon nanotube (SWCNT). Initially, carbon nanotubes raised a great interest in the research community because of their exotic electronic properties that exhibit, at low temperatures, a variety of transport phenomena specific for mesoscopic metallic conductors or semiconductor quantum wires and dots.

These transport properties depend in great part on a combination of multiple factors. For example, quantum effects can be studied as long as the length of the nanotube is smaller than the coherence length, ($L << l_\phi$), at low temperature, and we can talk about ballistic transport if $l_m << L$; for SWCNT, in order to respect the two conditions we need a length smaller than $\sim 700\ nm$. When connected to metallic leads, the confinement of the system gives rise to a discrete energy level inside the QD with a spacing between the levels that can be calculated from the interference condition: $\Delta = hv_F/L$ (see fig. 2.14, (b)).

Another important factor in quantum dots physics, due to the spatial confinement of electrons, is that the Coulomb electron-electron interaction becomes increasingly important and the same happens with correlations between electrons which play a prominent role in the characteristics of the systems. Spin correlations are built up due to the exchange spin-spin interaction, which results from the Pauli principle and also from the concerted action of charging effects.

The tunneling of electrons from the electrodes to the island is strongly influenced by the Coulomb charging energy of the QD. Tunneling of an electron into such an island increases the electrostatic energy of the island by the charging energy $E_C = e^2/2C$, where e represents the electronic charge and C is the total capacitance of the QD.

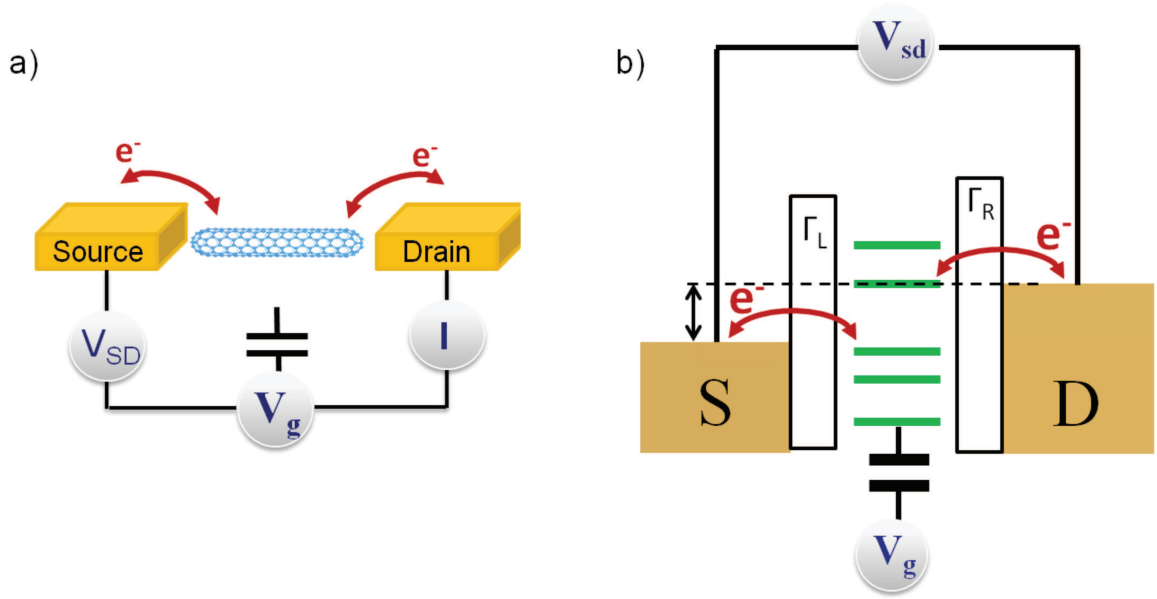

Figure 2.14: *(a) Schematic view of a CNT based quantum dot: two metallic leads (source and drain) are evaporated on the CNT; the nanotube is capacitively connected to a gate voltage while a source-drain tension is used to vary the chemical potential of the electrodes. (b) Heuristic picture of a QD connected through tunneling barriers ($\Gamma_{L(R)}$) to the metallic leads. The gate voltage controls the discrete energy levels inside the nanotube while the source-drain tension controls the chemical potential of the electrodes.*

Of course, we cannot speak about electron tunneling if the contacts between the CNT and metallic leads are not, to some degree, transparent to the charge carriers. In fact, probably, this is the most difficult to control parameter that influences the transport properties of a CNT. In samples having a low contact transparency, a pronounced Coulomb blockade is observed, where single-electron conductance peaks are separated by broad valleys of vanishing conductance (see fig. 2.15). To observe Coulomb blockade regime, thus discrete charges inside the QD, one needs that the transmission rate between the leads and the island to be much smaller than one, i. e. is the charges that manage to penetrate into the QD to remain blocked there for a sufficiently long time [30].

In the case of a more transparent contact between the island and the leads, we can speak about a Fabry-Perot transporting regime. Since we are speaking of highly transparent barriers, it become obvious that $E_C = e^2/2C \ll kT$. In this regime, the electronic interactions can be neglected; this makes the Landauer-Buttiker formalism very suited to electronically characterize such system. For a quasi-1D system, this is given by:

$$G = \frac{e^2}{h} \sum_{\sigma} \int -\frac{\partial f[(E - E_F)/k_B T]}{\partial E} T^{\sigma}(E) dE \tag{2.26}$$

where $T^{\sigma}(E_F)$ is the transmission of the i electron at the Fermi energy and df/dE

is the energy derivative of the Fermi function. The conductance is thus a measure of the transmission of electrons through the entire device at the Fermi energy, broadened by the finite thermal width of the Fermi function. When the Fermi energy is in the energy gap of the QD, $T^{\sigma}(E_F) = 0$ then the conductance is dominated by thermal activation. When E_F lies within an electron or hole subband, that is E_F is aligned with an energy level inside the QD, the transmission properties of the system, tube plus contacts, determine the conductance. If the transport is ballistic and the contacts are perfectly transparent, this equation predicts a quantized conductance of $4e^2/h$ associated with the 2 spin-degenerate channels.

A more complex behavior is revealed in samples where the conductance is partially blocked, but the signal in the valleys with a non-zero electron spin increases at low temperatures (that is we have a single electron on the last occupied energy level inside the QD), the system being in a Kondo regime. Nonetheless interesting, this transport regime does not concern the work done during this thesis, so i will not insist on it.

Fig. 2.15 shows such an example of the linear-response conductance versus gate voltage for a metallic nanotube measured at 1.6 K. It exhibits a quasi-periodic sequence of sharp peaks separated by zero-conductance regions, which signals Coulomb blockade single-electron charging behavior. A highly transparent contact allows for a Fabry-Perot's physics to manifest, represented in the same linear-response conductance by the chessboard region explained already above. In this regime the nanotube acts as a coherent waveguide and the resonant cavity is formed between the two CNT-electrode interfaces. The distance between the centers of the adjacent rhombus depends on the length of the nanotube.

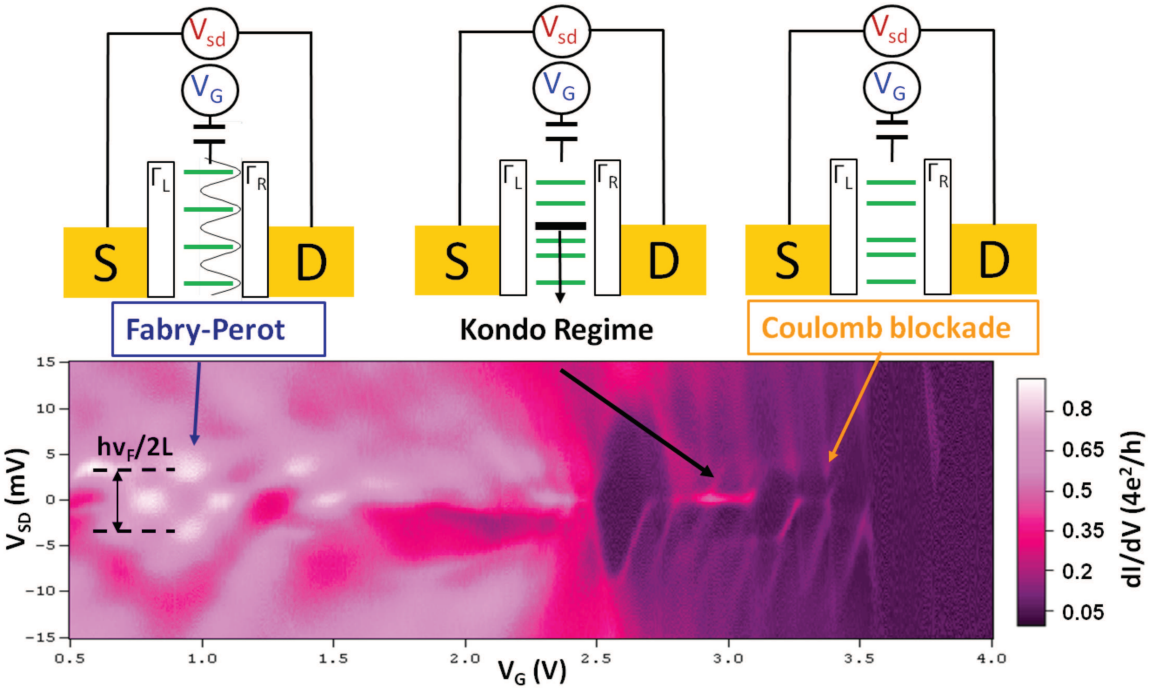

Figure 2.15: *Spectroscopy showing different types of transport regimes [28]. For highly transparent barriers between the QD and the metallic leads one gets the rhombic structure specific to the Fabry Perot transport regime with broadened spacing between the energy levels inside the nanotube. The distance between the centers of the adjacent rhombus is equal to the double of the spacing between the energy levels of the quantum dot and depends on the length of the nanotube. For low transparent barriers one gets a Coulomb blockade regime with narrow spacing between the energy levels. Fabry-Perot regime is observed at smaller gate voltages while the Coulomb blockade is in the higher gate voltage area. Between the two regimes we have also the Kondo ridge.*

2.2.1 Quantum spin valves in weak-coupling regime

In a two-terminal spin valve geometry, one can expect a difference in the resistance between two basic situations: first when the ferromagnetic leads are magnetized in anti-parallel geometry, so the majority of spins injected by the first lead will get mostly reflected by the second; this results in a high resistance state. Second situation describes the case when the ferromagnets have parallel alignment, so the injected electrons couple well with the second ferromagnet leading to a state with smaller resistance. At nanometric dimension, of course, one needs to take into account quantum confinement effects.

Recently, important progress has been made in the study of systems in weak coupling regime (Coulomb blockade regime). A very diversified transport behavior of the quantum-dot spin valves, as compared to other spintronic devices that relies on the

possibility to generate a non-equilibrium spin accumulation on the QD, that can be, a priori, manipulated through a multitude of parameters (gate and bias voltages, asymmetries in the tunnel couplings to the ferromagnetic leads and external magnetic field etc) recommends QDs as very promising systems to investigate [29].

A step in the understanding of this type of spintronic devices was added by Braun et al [31] who developed a theory of electron transport through QD weakly coupled to non-collinear ferromagnetic leads; central quantities in this model are the magnitude and the direction of the spin cumulated on the QD. They investigate both the linear ($V_{SD} = 0\ V$) and non-linear regime ($V_{SD} \neq 0$) and their theory can also integrate other parameters as external magnetic field, spin relaxation processes etc.

The calculus relies on a series of approximations. First of all, it is considered a QD with a level spacing exceeding thermal broadening, in which only a single level of energy ε measured relative to the Fermi energy of the leads, contributes to transport. Also, the QD is considered to be weakly-coupled to non-collinear ferromagnetic leads which are treated as reservoirs with noninteracting electrons. Thus only the degree of freedom of the QD will determine the transport properties of the system.

The Hamiltonian of such system is given by:

$$H = H_{dot} + H_L + H_R + H_{T,L} + H_{T,R} \tag{2.27}$$

where H_{dot} describes the atom like QD having a spin-degenerate energy level plus the charging energy $Un_\uparrow n_\downarrow$ for the double occupancy; $H_{L(R)}$ are the hamiltonian of the two leads $H_{T,L(R)}$ are used to characterize the tunneling events between leads and dot. The two ferromagnetic leads, denoted L and R are treated as a reservoir of itinerant electrons; for ferromagnetic leads,it is considered a strong spin asymmetry in the density of states $\rho_{r,\pm}$ for majority $(+)$ and minority $(-)$ spins; the direction of magnetization is considered parallel to the direction of majority spins. The asymmetry in the density of states is characterized by the degree of spin polarization $p_r = (p_{r,+} - p_{r,-})/(p_{r,+} + p_{r,-})$ with $0 \leq p_r \leq 1$; $p_r = 0$ describes a nonmagnetic lead and $p_r = 1$ a halfmetallic lead, with majority spins only. The magnetization of the leads form an angle of ϕ. A bias voltage is used to tune the electrochemical potentials in the two leads.

$H_{T,L}$ and $H_{T,R}$ describe the tunneling rates at the magnetic lead/QD interface that take into account the reflection/transmisison events that can take place. Braun and all use for the quantification of the QD the $\sigma = \uparrow, \downarrow$ in the z direction.

The dynamics of the system can be modulated using a density matrix which contains all degrees of freedom of the dot and of the leads. Since the leads are treated as reservoirs of noninteracting electrons, only the island's degrees of freedom account for the transport behavior. In concequence, a reduced density matrix, ρ_{dot} for the dot's degrees of freedom is enough to characterise the evolution of the system. A set of 6

master equations are used to describe the occupation probabilities and the average spin inside the QD. For the experiments presented in this work, one is especially interested in the three equations describing the time evolution of the average spin:

$$\frac{dS}{dt} = (\frac{dS}{dt})_{acc} + (\frac{dS}{dt})_{rel} + (\frac{dS}{dt})_{rot} \tag{2.28}$$

where: $(\frac{dS}{dt})_{acc}$ describes nonequilibrium spin accumulation via tunneling to and from spin-polarized leads, and is the source of the spin polarization in the quantum dot. The second term $((\frac{dS}{dt})_{rel})$ is an equilibrium term that describes the decay of the dot spin by tunneling out of the electron with given spin or by tunneling in of a second electron with opposite spin forming a spin singlet on the dot.

2.2.2 Magneto-Coulomb effect

Recently, significant progress has been made in studying the spin devices exhibiting a Coulomb blockade transport regime. Many of the interpretations, so far, have mostly focused on spin transport and spin accumulation. In this work we want to discuss another aspect of the "bystate" resistance systems.

In this context, for the general case of one-dimensional conductor weakly contacted with one ferromagnetic lead, the coupling can be described by using a resistance, R, and a capacity, C, for the F/QD interface. The QD is considered capacitively coupled to a gate voltage V_g. In this context, one wants to investigate what happens when an external magnetic field is applied. The magnetization of the ferromagnet is considered to have the same direction as the field applied. An important aspect to be taken into account is the initial difference in the density of states for the two species of electrons in the ferromagnet.

When, finally, the magnetic field is applied, the energy of the electrons ($\uparrow \downarrow$) inside the ferromagnet shift by the Zeeman energy in opposite directions. This results into a change of the chemical potential [50], $\Delta\mu$, in the electrodes:

$$\Delta\mu = -\frac{1}{2} P g \mu_B B \tag{2.29}$$

where $P = \frac{N^{\uparrow} - N^{\downarrow}}{N^{\uparrow} + N^{\uparrow}}$ is the polarization of the lead, g, it accounts for the gyromagnetic ratio and μ_B is the Bohr magneton. Now, one can write the conductance, G, as a function of the induced charge. Hence, when a field is applied, the conductance changes:

$$G(q, B) = G(q) + \frac{dG}{dq} \Delta q(B) \tag{2.30}$$

Here q denotes the charge state of the QD in the absence of magnetic field, B. For a Coulomb island, both $G(q)$ and $\frac{dG}{dq}$ can be experimentally measured. It is visible that

$G(q)$ has a periodic character thus also $\frac{dG}{dq}$ changes sign periodically, too. Energetically speaking, to observe distinct charges in QD, one needs:

$$E_C = e^2/2C \gg kT \tag{2.31}$$

and in addition a tunnel resistance of the metal/CNT interface larger than h/e^2.

Since the ferromagnet is contacted to a non-magnetic material, an equality in the chemical potentials must be reached. Hence, the energy shift inside the ferromagnetic electrode leads to a change of the contact potential, $\Delta\phi$ at the F/QD interface by:

$$-e\Delta\phi = -\Delta\mu \tag{2.32}$$

This shifts the Coulomb levels inside the QD and additional charge Δq is induced into the island due to the change in the contact potential $\Delta\phi$. Thus we can see an effect analogous to the use of a gate voltage on the system. This equivalence was demonstrated by Ono et al [32]. For the situation described above, we can write:

$$\Delta\ q(B) = \frac{C}{2e} P g \mu_B B \tag{2.33}$$

The magneto-Coulomb effect was first reported by Ono in a single-electron transistor based on a metallic island coupled to two ferromagnetic leads which exhibited a Coulomb blockade transport regime. He reported an enhancement of the MR signal in the island and concluded that the effect originated from the Zeeman energy of the ferromagnetic contacts which were inducing a splitting of the majority/minority carriers inside the island.

So far, the magneto-Coulomb effect (MC) was treated only in the absence of any magnetization switching inside the ferromagnet. If one considers the system presented above, with one ferromagnet weakly connected to a non-magnetic conductor and applies a negative field $B < 0$, then the conductance varies linearly with the field as long as no switching of the magnetization takes place; however, when $B = -B_C$, where B_C is the coercive field of the lead, the magnetization of the ferromagnet switches. Thus the charge changes too by $\Delta\ q(B) = \frac{C}{2e} P g \mu_B B$.

On a map representing the current transport as a function of the external field, the magneto-Coulomb can be seen as a jump in the conductance; for more negative external field applied then the conductance will return to a linear dependence with B. To characterise devices with two ferromagnetic electrodes, one would need to simply add the two effects [33]. The conductance, in this case, can be written as:

$$G(V_G) = G(V_G - C_L \Delta\mu_L/e - C_R \Delta\mu_R/e) \tag{2.34}$$

where $R(L)$ designate the right/left electrodes. If an external magnetic field is applied, an hysteretic signal, signature of a reversal in the magnetization of the leads,

could be recorded. This happens in the absence of spin injection related phenomena. The magnetization contribution to the MC effect can be written as:

$$MR = -\frac{1}{G}\frac{dG}{dV_G}\frac{g\mu_B(p_L C_L H_{cL} + p_R C_R H_{cR})}{eC_G} \tag{2.35}$$

It can be easily seen that the magnetoresistance of the system depends on the derivative of G (the conductance of the system) which can be translated into a change of sign along the MR variation and the presence of conductance peaks.

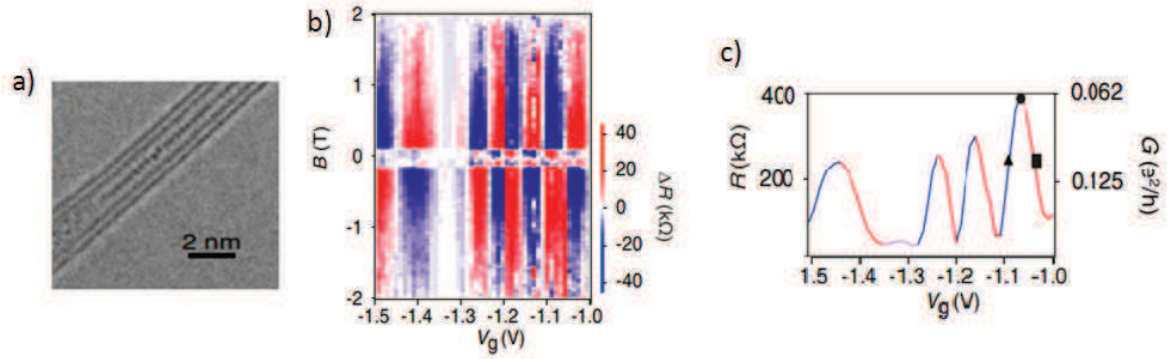

Figure 2.16: *(a) High resolution TEM image of a portion of a double-wall CNT filled with elongated FeO particles; (b) Hysteresis plot (difference between trace and retrace) as a function of V_G. Positive, negative, and zero hysteresis are plotted respectively in red, blue, and white. (c) The differential resistance as a function of V_g (the same V_g values interval as for the hysteretic curves presented at point (b)). The color of the curve changes with the sign of the slope: red → positive and blue → negative. We note a correlation between the sign of the hysteresis after the jump and the slope at the same point.*

Datta et al [34] investigated MCE in a double-wall CNT QD system containing a single magnetic nanoparticle. The nanotube is connected with Pd electrodes and capacitively coupled to a gate voltage as seen in fig. 2.16, (a). Transmission electron microscopy of hybrid nanotubes shows row of crystallites several tens of nanometers long encapsulated inside the inner shell of the CNT. Electrical measurements on the junction were performed at very low temperature ($T = 40\ mK$).

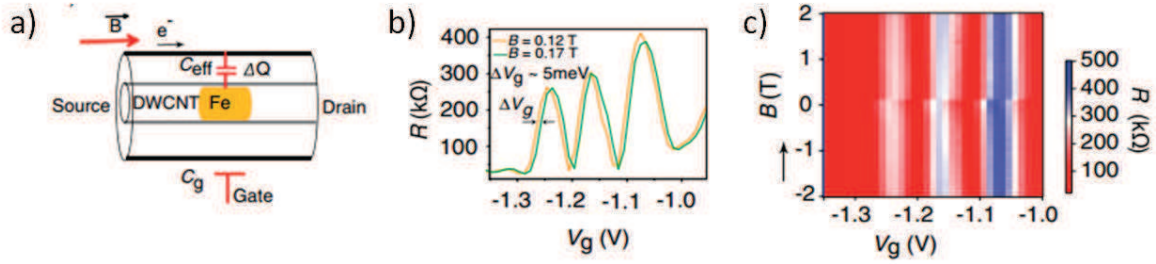

Figure 2.17: *(a) SEM image of a portion of the CNT filled with FeO particles and the equivalent electrical circuit of the resulted device; it should be noted that the magnetic particle is trapped inside the interior wall of the CNT. (b) Hysteresis plot (difference between trace and retrace). Positive, negative, and zero hysteresis is color plotted as red, blue, and white, respectively. (c) The resistance as a function of V_g and B (traces from -2 to $+2$ T) together with horizontal cuts, presented above, showing a right shift (V_g) of 5 meV of the Coulomb oscillations after the switching field $B = \pm 0.15$ T*

The differential conductance dI/dV spectrum as a function of the gate voltage V_g emphasizes a series of peaks and dips, related to Coulomb blockade transport regime, characterized by single-electron tunneling through the QD. The irregularity of the G amplitude modulation as a function of V_g is probably due to the filling procedure.

Electrical measurements done in presence of a sweeping external field, on a bigger range for the gate voltage show a hysteretic TMR signal. When plotting the trace minus retrace signal (trace, when the field is increasing and retrace when is decreasing, for example) as in fig. 2.16, (b)), color alternates red and blue as a function of V_g. This succession of colors indicates the sweeping character of the TMR between negative and positive values, separated by regions of completely suppressed signal, colored in white.

At high fields, the resistance R tends to diminish. The discontinuous jumps occur for the same value of the switching field $B_{sw} \pm 150$ mT and have a symmetric evolution, independent of the gate voltage. Datta et al stated the B_{sw} value in this V_g range can be attributed to the magnetization reversal of the magnetic nanoparticle.

They observed a hysteretic TMR signal clearly correlated to the differential resistance of the device at zero field plotted in fig. 2.16, (c). It is obvious theree is a relation between the sign of R_{sw} and the sign of the differential resistance slope dR/dV_g, due to the sweeping through Coulomb peaks.

By looking at the MR single traces directly as a function of V_g, a sudden gate shift can be noticed at $B = B_{sw}$, see fig. 2.17, (b). The gate oscillations of R which occur when V_g is varied, for $B < B_{sw}$ and , $B > B_{sw}$ are similar in fig. 2.17, (a) and (b) though shifted by an amount of $V_g = 5$ mV. The influence of magnetization reversal

at B_{sw} on the nanotube QD can thus be compared to a change in the offset charge.

An equivalent electrical circuit of the device is presented in fig. 2.17, showing the nanoparticle isolated from the environment in the inner wall of a DWCNT. The outer wall is coupled to the gate electrode via the capacitance C_g. The effective coupling between the two walls of the nanotube and the nanoparticles is depicted using a capacitance, C_{eff}. In this geometry the current is passing only through the outer wall.

Giving all these evidences, Datta et al concluded the MCE measured, originated from the contact between the magnetic particles and the ferromagnetic leads, being induced by a local coupling of the magnetic particle/QD, without having a ferromagnetic contact. The measured magnetoresistance of CNT turned out to be completely tunable by using a gate voltage.

2.3 Recent experimental work on spin polarized transport

Current efforts in designing and manufacturing spintronic devices are focused on two main different approaches. One way of progressing is by perfecting the existing GMR-based technology by either developing new materials with larger spin polarization of electrons or making improvements or variations in the existing devices that allow for better spin filtering. The second direction, which is more radical, focuses on finding novel ways of both generation and utilization of spin-polarized currents, eventually in totally new systems.

In this context, Sahoo et al [35] investigated MWCNT and SWCNT contacted with PdNi ferromagnetic leads in collinear geometry. The nanotubes are capacitively coupled to a back-gate (V_g) used to tune the CNT's energy levels. A source-drain voltage is used on the ferromagnetic leads to vary their chemical potential. Transport characterizations of the system revealed that in resonant tunneling conditions, the amplitude and sign of the TMR show a dependence with the gate voltage.

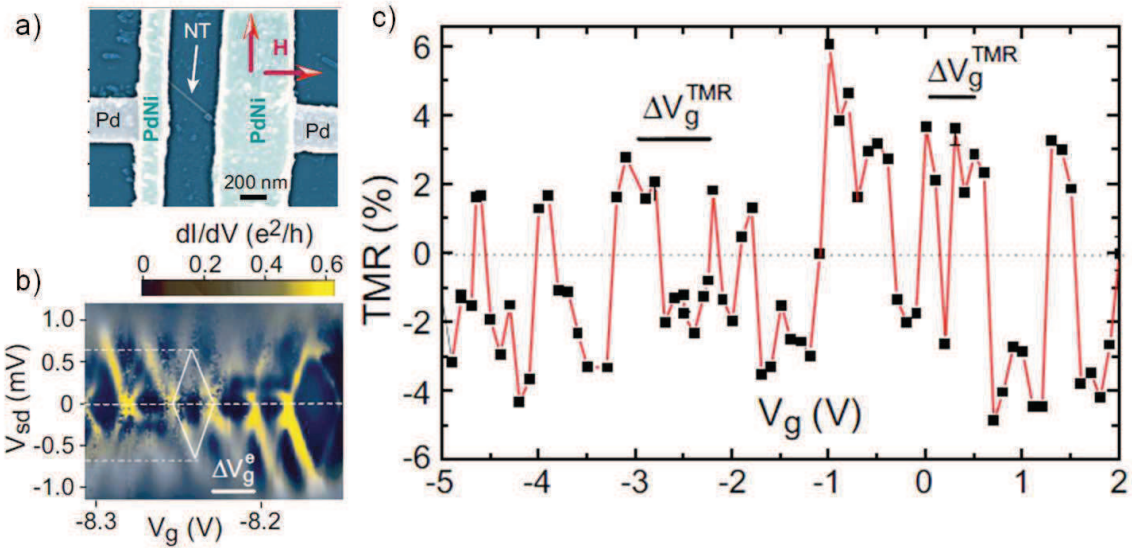

Figure 2.18: *Experimental results obtained by Sahoo et al [35] on a MWCNT based device connected to PdNi leads; (a) SEM picture of the device: the nanotube is connected with two parallel ferromagnetic leads with different chemical potentials; the nanotube is approximatively* 400 *nm long. The magnetic field can be applied both along the easy/hard geometric axes of the leads. (b) Differential conductance* dI/dV *as a function of both* V_g *and* V_{SD} *taken at* 300 mK*. Diamond shape structures reveal a single electron tunneling (Coulomb Blockade) conduction regime. (c) The TMR variations with gate voltage* V_g*. Measurements performed at* $T = 1.85$ K*.*

Differential conductance measurements, dI/dV, as a function of both V_g and V_{SD} taken at 300 mK revealed diamond shape structures characteristic for single electron tunneling events which places the system in a Coulomb Blockade conduction regime. Measurements of the TMR signal with gate voltage performed at $T = 1.85$ K revealed variations of the magnetoresistance, which can take both positive and negative values.

The same group reported transport measurements on a SWNT-based device, where single particle resonant levels can be probed even at temperatures of $T = 1.85$ K. In MWCNT the QD behavior can be seen only around 300 mK. The explanation comes from the fact that single particle energy addition is much higher in SWCNT than in MWCNT, allowing to measure the TMR signal for each resonant level. They concluded that the interference of single particle levels is at the origin of the observed TMR oscillations.

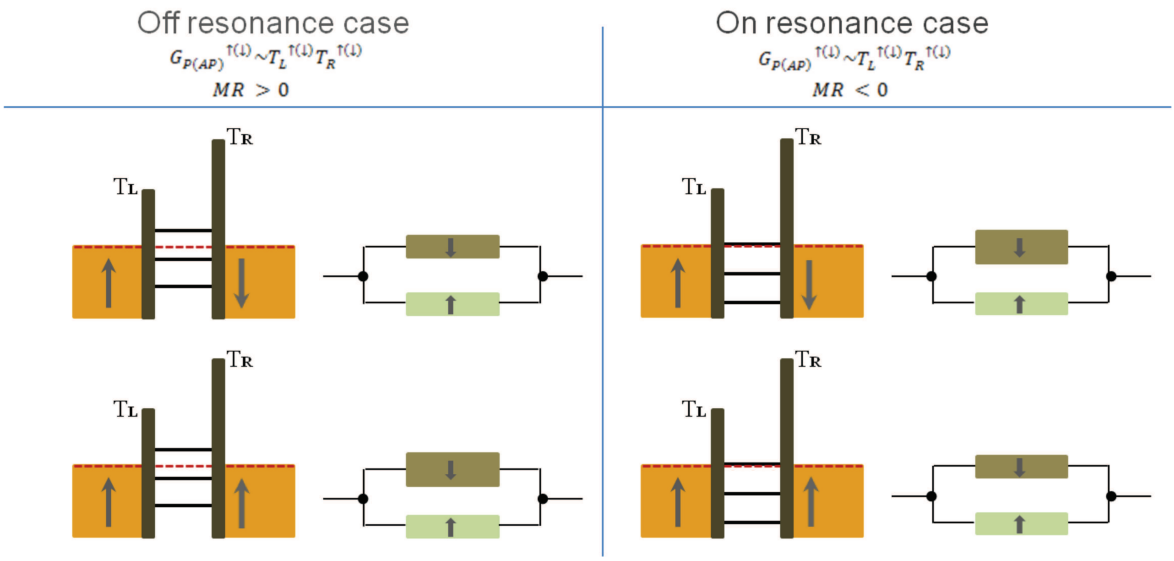

Figure 2.19: *Spin-dependent tunneling effect in QD-like system connected with ferromagnetic leads; in these conditions, the tunneling rates are spin-dependent turning the total electric resistance of the system also spin-dependent; the total resistance R is equivalent to a parallel circuit between $R^{\uparrow}$ and $R^{\downarrow}$. On resonance, $R^{\uparrow} = R^{\downarrow}$ in the parallel configuration, while $R_{\uparrow}$ is smaller and $R_{\downarrow}$ larger in the antiparallel configuration. Due to the dominance of the smaller resistance in a parallel circuit, R is smaller in the antiparallel as compared to the parallel case, corresponding to a negative TMR signal. Off resonance, $R^{\uparrow} = R^{\downarrow}$ in antiparallel configuration, while $R_{\uparrow}$ is smaller and $R_{\downarrow}$ in the parallel configuration determining a positive TMR signal.*

A mechanism based on spin-dependent resonant tunneling effect was used to explain the anomalous sign and the asymmetric variations of the TMR with V_g. Breit - Wigner reference formula is appropriate to express the total transmission of the system; this provides a good description of the experimental data, as long as the couplings to the leads are small (see fig. 2.18, (a) [35]).

For off resonance cases, $|E - E_0^{\sigma}| \gg (\Gamma_L^{\sigma} + \Gamma_R^{\sigma})$ and one expects to the normal positive values of TMR, which can be explained using Julliere's model.

The situation changes on resonance, when the TMR is naturally negative (see fig. 2.19). For ferromagnetic leads, the tunneling rates are spin-dependent: it increases for the majority spin and it decreases for the minority ones. In consequence, the electric resistance becomes also spin-dependent and the total resistance R is equivalent to a parallel circuit between $R^{\uparrow}$ and $R^{\downarrow}$. It becomes obvious that $R^{\uparrow} = R^{\downarrow}$ in the parallel configuration, while $R_{\uparrow}$ is smaller and $R_{\downarrow}$ larger in the antiparallel configuration. Due to the dominance of the smaller resistance in a parallel circuit, R is smaller in the antiparallel as compared to the parallel case, corresponding to a negative TMR signal.

Sahoo et al obtained a good coordination between theoretical and experimental data (see fig. 2.20, (*b*)) for SWCNT based device suggesting a finite spin-dependence of interfacial phase shifts (SDIPS) in the system that leads to a TMR effect tunable with the gate voltage and the magnetic field.

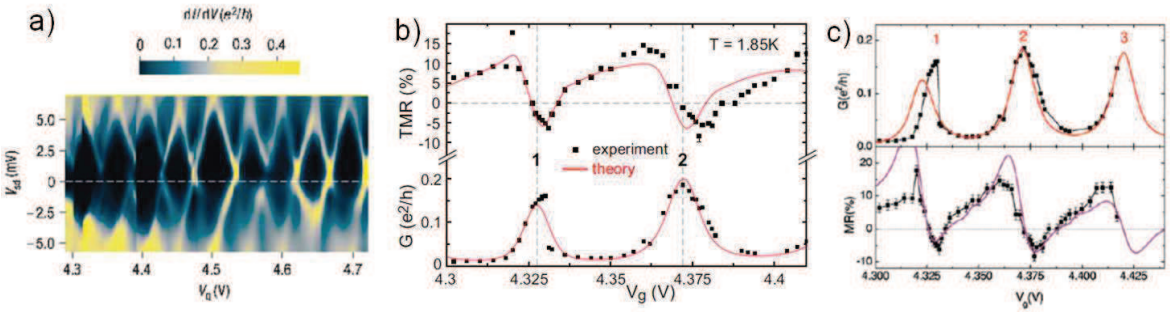

Figure 2.20: *(a) Grey scale plot of the nonlinear conductance of the nanotube as a function of the source − drain voltage, V_{SD}, and the gate voltage, V_g. The intrinsic energy spacing of the levels is about $E = 2,5\ meV$. (b) the dotted line (black): conductance G and the TMR as a function of V_g; the full lines (in red) theoretical curves consistent with the experiment, obtained by using an non-interacting model; (c) the dotted line (black): conductance G and the TMR, simultaneously measured at $T = 1.85\ K$; the full lines (in red) represent theoretical curves obtained by using an equation of motion (EOM) for a QD with two degenerate energy levels.*

Even if good to explain the negative values of the TMR, this model cannot fully explain the differential conduction as a function of V_{SD} and V_g measured for the two types of devices presented in fig. 2.18, (*b*) and 2.20, (*a*). An interacting approach that considers the nanotube as a quantum dot (QD) connected through tunneling barriers to the two ferromagnetic leads proved much more appropriate. In fact the two spectroscopies presented by Sahoo et al describe the case of the electrons tunneling into/outside the QD one at a time which gives a Coulomb blockade specific pattern in the conductance.

Cottet et al [36] presented a model based on an equation of motion technique (EOM). They obtained a good quantitative agreement with Sahoo's experimental data on SWCNT 2.20, (*c*). The presence of the ferromagnetic leads is taken into account by introducing a spin dependent phase difference of the electronic wave when reflected by the CNT/ferromagnetic interface. Such parameter takes into account the asymmetry of the TMR which underlines the existence of an local exchange field that can be calculated from the difference between the energy level of the up/down spins: $E_\uparrow - E_\downarrow = 0.26\ meV$ which corresponds to a $B_{ech} \sim 2\ T$.

The spin imbalance in the CNT could also originate in the stray magnetic field coming from the ferromagnetic leads. The stray magnetic field due to FM electrodes

varies with the magnetizations of the two electrodes when they swing between parallel or antiparallel configuration; thus the magnetic environment close to the nanotube also experiences some changes. That could be responsible for the hysteretic behavior of the system. Sahoo et al proved this is not the case for their sample by simply comparing the high-field magneto-resistance with the low-field hysteretic TMR signal and found that the magnitude of the TMR signal is much superior to one provided by the background which in addition does not variate with the gate voltage.

2.3.1 Effective fields

So far, we have addressed the problematic of spin polarization and detection by a current. But, how can we best manipulate the direction of this polarization once it has been created? Intrinsic effective magnetic fields that depend on the motion of charge in the system could be an answer.

As seen in the work presented by Sahoo et al, spin valve like devices based on CNT can exhibit an effective magnetic field. Others also found that systems based on CNT connected to ferromagnetic leads can exhibit similar intrinsic magnetic fields.

For example, Pasupathy et al [37] performed transport measurements in C_{60} molecules, connected to Ni electrodes with different coercive fields, so that they undergo magnetic reversal at different values of the external field. Fullerenes represent a distinct state of carbon, like diamond and graphite, which is composed by hexagonal/pentagonal packed carbon atoms rapped into a spherical hollow shape, similar to a football.

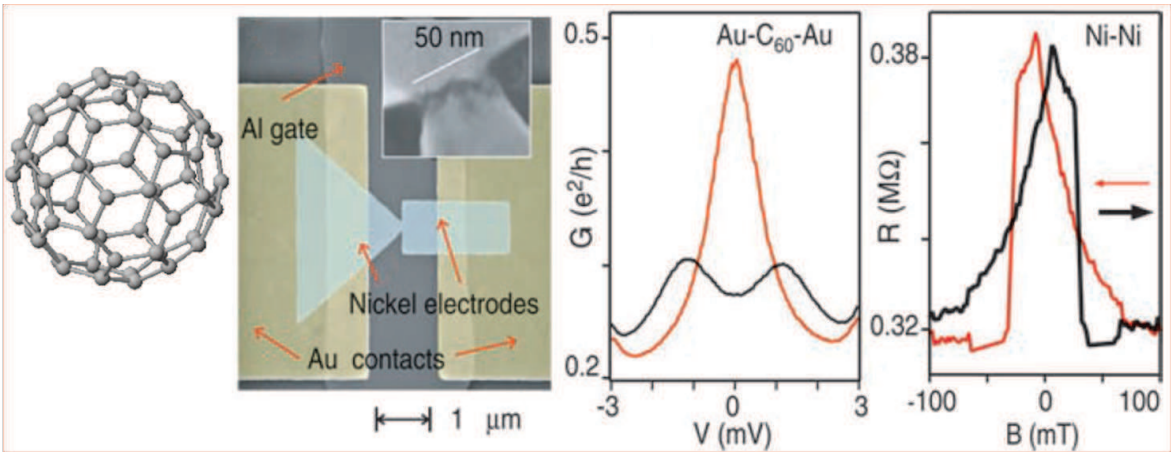

Figure 2.21: *(a) Fullerene molecule: hollow, spherical molecule composed of hexagonal and occasionally pentagonal groups of carbon atoms; (b) SEM photo of a Ni break junction capacitively connected to a Al gate voltage and to Au contacts. A zoom of the area where the fullerene molecule is introduced is presented in the inset; (c) Kondo signal measured in a C_{60} based junction. Red line: Kondo specific peak for $B_{ext} = 0\ T$, black line: splitting of the Kondo peak at $B_{ext} = 10\ T$, measurement performed at $T = 1.5\ K$; (d) hysteretic cycle measured for $V_{SD} = 0\ V$, after the electromigration process and in the absence of the fullerene, measurement done at $T = 4.2\ K$.*

The phenomenology tested by Pasupathy refers to Kondo physics: a coupling between a localized spin that acts as a "magnetic impurity" and conduction electrons of a host material, with the purpose of screening the perturbation created by the spin. The Kondo effect is easy to identify using conduction measurements, at low temperature; measurements done on C_{60} contacted with Au electrodes show a narrow peak in conductance with a broadening of order of T_k (see fig. 2.21, (c) - red curve) that splits when exposed to an external magnetic field (see fig. 2.21, (c) - black curve).

TMR measurements on Ni electrodes, in the absence of the fullerene molecule (presented in fig. 2.21, (d)), show typical, hysteretic switching for the relative orientation of the magnetic moments in the two electrodes between parallel (P) and antiparallel (AP) alignment.

The novelty of this experiment, comes from the low temperature ($T = 4.2\ K$) conduction measurements done on a single-electron transistor type of system made using C_{60} coupled to Ni and gold electrodes, see fig. 2.21, (b). One would expect for the Kondo physics to vanish due to its competitional character with Ni's ferromagnetism character, but Pasupathy et al reported Kondo signatures demonstrating the existence of a strong coupling between the fullerene island and nickel electrodes.

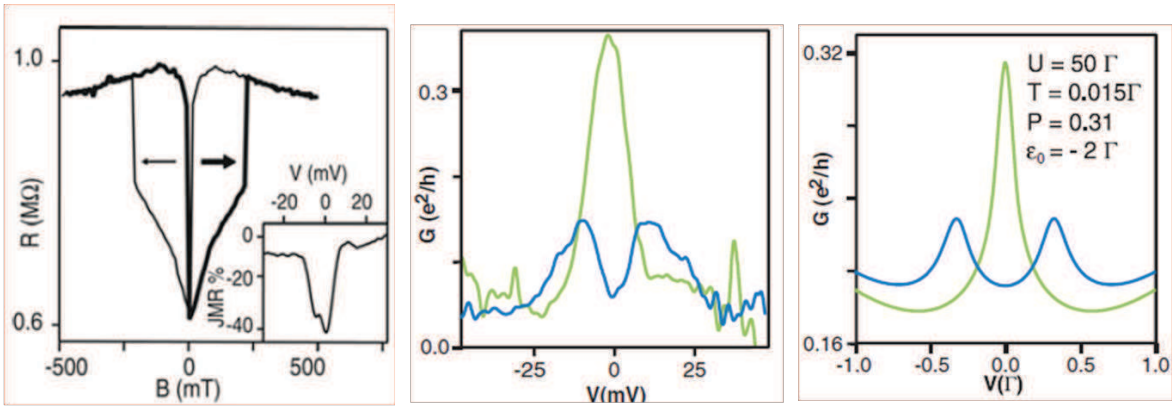

Figure 2.22: *(a) Magnetoresistance taken at $V = 0\ V$ in a $Ni - C_{60} - Ni$ sample exhibiting a unusual negative TMR value for a MTJ. In the inset it is visible the TMRis of about 40 percent ; measurement done at $T = 1.5\ K$; (b) blue line, a conductance measurement on a $Ni - C_{60} - Ni$ system showing a dedublation Kondo peak that gets reconstructed - green line, when the magnetizations of the leads switch to the antiparallel configuration; (c) Theoretical fit to the experimental curves presented at point (b) using a technique equation of motion .*

In fig. 2.22, (b) - blue line, a measurement in parallel configuration shows a splitting in the Kondo peak that gets reconstructed (like in fig. 2.22, (b) - green line) when the magnetizations of the leads pass in antiparallel configuration. This splitting in the conduction peak is important for two reasons: one because it allows a calculation of the effective field of the sample and second because it explains the presence of the negative TMR presented in fig. 2.22, (a). The negative TMR, opposite to the typical behavior in MTJs, and its magnitude, almost twice larger than the one calculated using Julliere model; this happens because the Kondo resonance occurs close to the Fermi energy in the antiparallel orientation of the magnetizations, thus enhancing the system's conductance.

Theoretical calculations using EOM equations presented in fig. 2.22, (c), are in good agreement with the experimental results proving that an electron inside a quantum dot can interact with the ferromagnetic leads giving rise to a Kondo phenomenology.

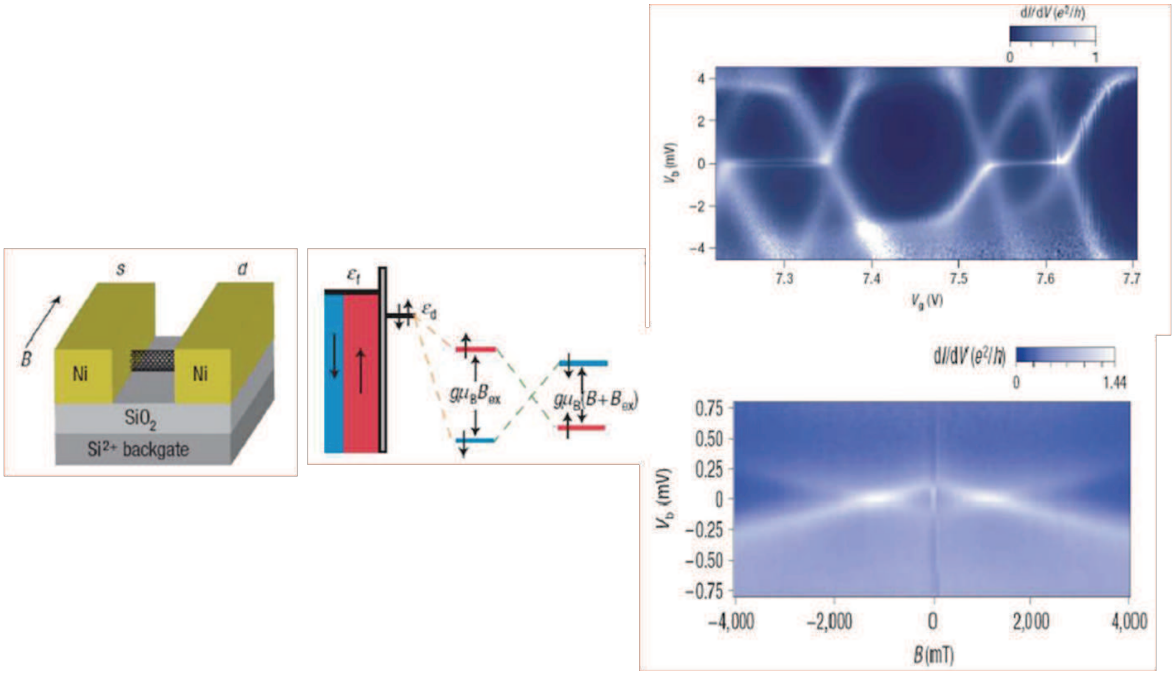

Figure 2.23: *(a) Illustration of a CNT-based dispositive. The nanotube is capacitively connected to a gate voltage V_g and also to two Ni electrodes. An external field can be applied in the same plane as the substrate; (b) the splitting of the localized spin state can occur both by an applied external field (blue) and an internal exchange field (red) tunable by the gate voltage; (c) measurements of the differential conductance, dI/dV, as a function V_g and V_{SD} show 4 Coulomb diamonds with a Kondo resonance binding two of them; (d) differential conductance, dI/dV, as a function V_g and B_{ech} measured inside one of the diamonds exhibiting a Kondo resonance mark.*

The existence of internal effective magnetic fields inside an CNT coupled to ferromagnetic leads was reported also by Hauptman et al [38]. The device presented in fig. 2.23, (a) couples Ni based leads to an CNT which is capacitively coupled to gate voltage represented by the doped substrate. The improvement with respect to Pasupathy's device is the back gate which allows for direct electrical control over the coupling between the ferromagnet and the island. In these conditions, one would expect that the exchange field would be also tunable with the gate voltage. The origin of this exchange field comes from the local field induced by the ferromagnetic leads that will polarize the localized spins even in the absence of an external field.

This effective field can be compensated using an external field applied in the same plane as the sample. Hauptman found that for a $B_{ext} = 1.1\ T$ the Kondo peak is restored for $V_{SD} = 0\ V$ - see fig. 2.23, (d). Even more the exchange field can be tuned using the gate voltage solely.

Both Patsupathy's and Hauptman's experiment proved the existence of an intrin-

sic effective field (B_{ech}) that originates in the exchange magnetic field created by the ferromagnetic leads which will polarize the spin trapped in the carbon-based island. B_{ech} can be theoretically reproduced by using a Spin-Dependence of Interfacial Phase Shifts (SDIPS) approach and correlation exchange field.

Chapter 3

Experimental setup

3.1 Sample preparation

The results presented in this thesis concern, mainly, two different types of samples. A first one represented by PdNi crosses, used to investigate the anisotropy of PdNi-based micrometric and nanometric systems while the second type of samples concern devices based on CNTs connected by PdNi nanostripes.

The spin-valve devices we studied are based on a SWCNT, capacitively coupled to a back gate and, at the same time, contacted with two ferromagnetic leads as we can see in the fig. 3.1. Obtaining such a system requires a succession of lithographic/carbon nanotube growth/metallic film deposition processes that will be further discussed. In addition, to better understand the properties of these devices we also magnetically investigated PdNi micrometric/nanometric sized samples.

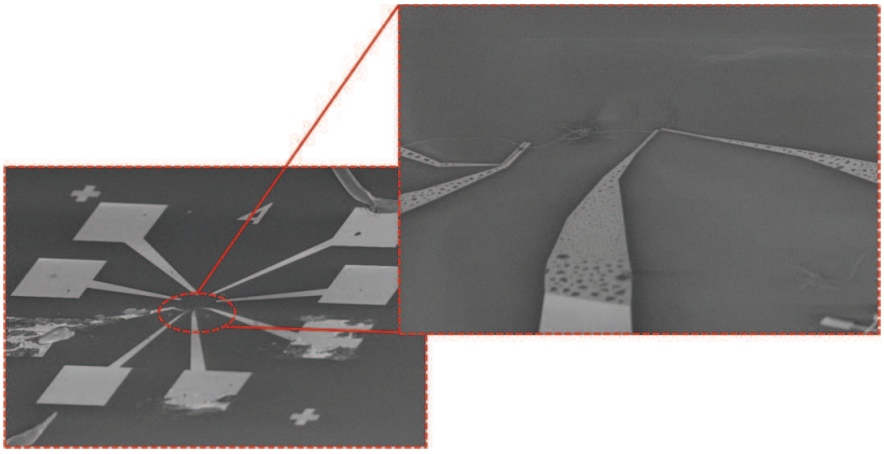

Figure 3.1: *Typical samples. Pictures acquired under a SEM observation system microscope. CNTs are connected with ferromagnetic electrodes,* $Pd_{30}Ni_{70}$*,* 30 *nm thick and* 200-300 *nm wide, covered with* 5 *nm of Pd; on one substrate one can have both parallel contacts and contacts that form an angle* $\theta = \pi/2$*.*

The nanometric dimensions of this device as well as the use of carbon nanotubes and the high sensibility of the entire system to any electrostatic charge, make the nanofabrication process a delicate one. In fig. 3.1 are visible two such systems that we tested during this thesis. In the insert we see magnified two of the samples exhibiting a perpendicular, respective, parallel geometry. The carbon nanotubes are connected with PdNi electrodes which at their turn are contacted to Au pads. We use Au alignment crosses (both small and big ones) to align the lithography onto the selected nanotubes and thus gain in precision over the physical properties of the system.

3.1.1 The substrate

The first step towards a good sample is the appropriate choice of the substrate. In order to minimize the fabrication steps needed to obtain a viable sample, we decided to apply the gate voltage directly to the substrate. Thus we chose to work with a n-doped Si substrate, having a resistivity of $0.004 - 0.008$ Ωcm and coated with 525 ± 25 μm SiO_2. We cut the wafer in pieces of 8 x 8 *mm* and we clean it in three different shown in table 3.1.

Step no	Procedure	Characteristics
1.	Sample immersed in acetone, in ultrasound bath	10 mins
2.	Sample immersed in isopropanol (IPA), in ultrasound bath	10 mins
3.	Harrick plasma oven	10 mins in O_2 plasma, 200 W, $P \leq 10$ μbar

Table 3.1: *The different steps for cleaning the substrate.*

3.1.2 The lithographic process

Working with samples of nanometric sizes, together with the need of high precision for patterning functional materials (such as Au and PdNi), made the electronic lithography an indispensable tool to this thesis work. The lithographic process consists in exposing the surface of the sample, while covered with a resist film, using a beam of electrons.

The exposed parts of the resist, in this case, Polymethyl methacrylate (PMMA), become consequently soluble in a specific developer, leaving on the substrate only the unexposed regions.

Catalyst is deposited or functional materials are evaporated in the resist free area. The rest of the resist is removed during the last step of the lithographic process called "lift off". All these steps are presented in the fig. 3.2.

3.1.3 The resist

For sample fabrication process it was used as resist A6 Poly(methyl methacrylate) 950, diluted in anisole. This is a standard positive resist which can be developed away in the areas exposed to the beam of electrons.

The sample was prepared for lithography by depositing few drops (4 or 5) of PMMA on the substrate, which is after spunned in a spin coating machine at 4000 revolutions/min for 30 s. The chip is then baked at 165° C for 15 minutes. This process creates a 500 nm thick layer of resist. Such a layer is enough for successfully patterning structures up to 50 nm in thickness. For features thicker than that, a second layer of

	Lithographic Process	General Parameters
1.	Contact pads and alignment structures	Voltage: 20 kV, Aperture 10 μm, Step size 20 nm, Dose 250 $\mu m * cm^{-2}$
2.	Fine structures	Voltage: 20 kV, Aperture 7.5 μm, Step size 20 nm, Dose 360 $\mu m * cm^{-2}$
3.	CNT localization	Voltage: 2 kV, Aperture 10 μm, Magnification $\sim 1k$

Table 3.2: *SEM parameters used during each lithographic step.*

resist, deposited in similar conditions to the first one described above, is needed.

3.1.4 The electronic lithography

The fabrication process of the devices measured here needs the use of the e-beam lithography three times. First to pattern the areas later exposed to the catalyst, necessary for the nanotube growth, then in a second step to open the areas where the alignment markers and the big contact pads will be evaporated and finally to draw the PdNi electrodes.

Parameters like the aperture size, which determines the dimension of the e-beam and indirectly also the writing speed, need to take into consideration the shape and size characteristics of the patterns we want to create. The smaller the aperture, the longer the time the resist will be exposed to the electronic bombardment. The exposure gives the amount of charges that reach the resist per area unit. In case of overexposure, oversized patterns are to be expected while underexposed, the development will not be complete. For all the samples measured during this thesis, dose tests were performed on test samples.

The SEM system was also used to acquire images of the CNT, necessary to create the dedicated electrode masks. In order to avoid damaging the nanotubes, the observations were conducted using acceleration voltages much smaller than the ones used for the lithographic step (see table 3.3).

3.1.5 Development

After each lithographic step, the removal of the resist exposed to the electronic bombardment is done methyl-isobutyl-ketone (MIBK): isopropanol (IPA) 1:3. The sample in this solution for 2 minutes and then dried using a nitrogen gun.

Schematically, the entire sample fabrication process, together with the general settings used, is shown in fig. 3.3.

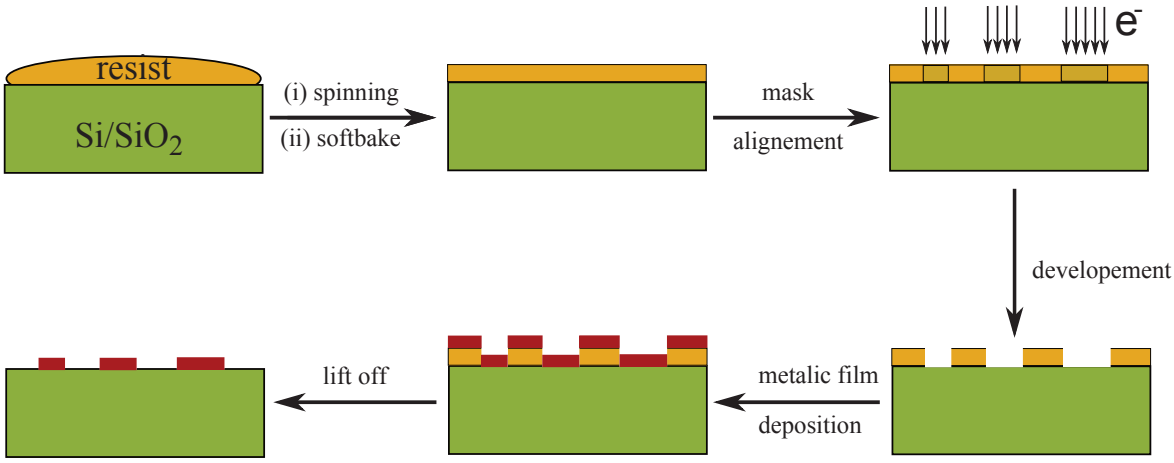

Figure 3.2: *Typical nanofabrication process: a resist is deposited on the substrate that is further spun in a coating machine and baked at* 165 C *to obtain an uniform layer of resist; the sample is exposed to an electron beam following pre-drawn patterns; the exposed resist is removed during a development process; the sample undergoes a metallic film deposition step; the rest of the resist and the surplus of the metallic resist are removed during a lift off process.*

3.1.6 Thin film deposition

As indicated in fig. 3.3, there are needed 2 steps of metallic film deposition during the nanofabrication process: one to create the gold contact pads and the alignment crosses and a second one for the PdNi used to contact the nanotubes.

The common evaporation method, namely the Joule heating of a metallic target above its melting point, creating thus a beam of metallic atoms that will reach the surface of the sample is more than enough for the task. To obtain a good, uniform, homogeneous film, one needs the entire process to take place in high vacuum ($P \leq 10^{-6}\ mbar$). This is done by using a two step pumping process. The thickness of the film is controlled using a quartz deposition controller placed inside of the evaporation machine.

For a better adhesion of the gold on the substrate, first it is evaporated a very thin layer of chromium. The general parameters used during this step can be consulted in table 3.3.

Metal	**Pressure (mbar)**	**Current (A)**	**Rate (Å/s)**	**Thickness (nm)**
Chromium	$2.5 * 10^{-5}$	90	0.1	30
Gold	$1.1 * 10^{-5}$	85	0.15	60

Table 3.3: *Evaporation parameters for the cromium/gold metallization.*

The second metallization process, dedicated to the PdNi is a more delicate one, because PdNi requires a better vacuum for a good evaporation ($P \simeq 10^{-7}/10^{-8}\ mbar$).

For this step it was used a UHV system at ESPCI which used endowed with an electron gun capable to produce a beam of high energy electrons. This beam brings the metallic target to sublimation point. During this work, this process was used to obtain layers of 30 nm of PdNi covered by a cap of $\sim 5\ nm$ of Pd, to avoid the oxidation of the PdNi. The details of this metallization process, can be found in table 3.4.

Metal	**Pressure (mbar)**	**Current (A)**	**Rate (Å/s)**	**Thickness (nm)**
PdNi	$5 * 10^{-7}$	$7 * 10^{-7}$	3	30
Pd	$8 * 10^{-7}$	$2 * 10^{-7}$	1.5	$4 - 5$

Table 3.4: *Evaporation parameters for the PdNi/Pd electrodes.*

After the evaporation is done, an acetone-based lift-off process is done to remove the metallic parts that were not exposed during the lithographic process. The sample is immersed into preheated acetone, ($\sim 55°$ C) for some minutes (usually, 5 - 10 minutes will suffice, but the process can continue up to 30 minutes or more, if needed). A pipette is needed to blow the acetone on the surface of the sample to speed up the process.

3.1.7 CNT growth

Various methods were used to improve the control on the properties of such structures. The main interest at this point is to obtain single wall carbon nanotubes (SWCNT) displaying metallic and/or semiconductor behavior. Thus, a chemical vapor deposition (CVD) technique, with molybdenum oxide based catalyst seemed the most advantageous.

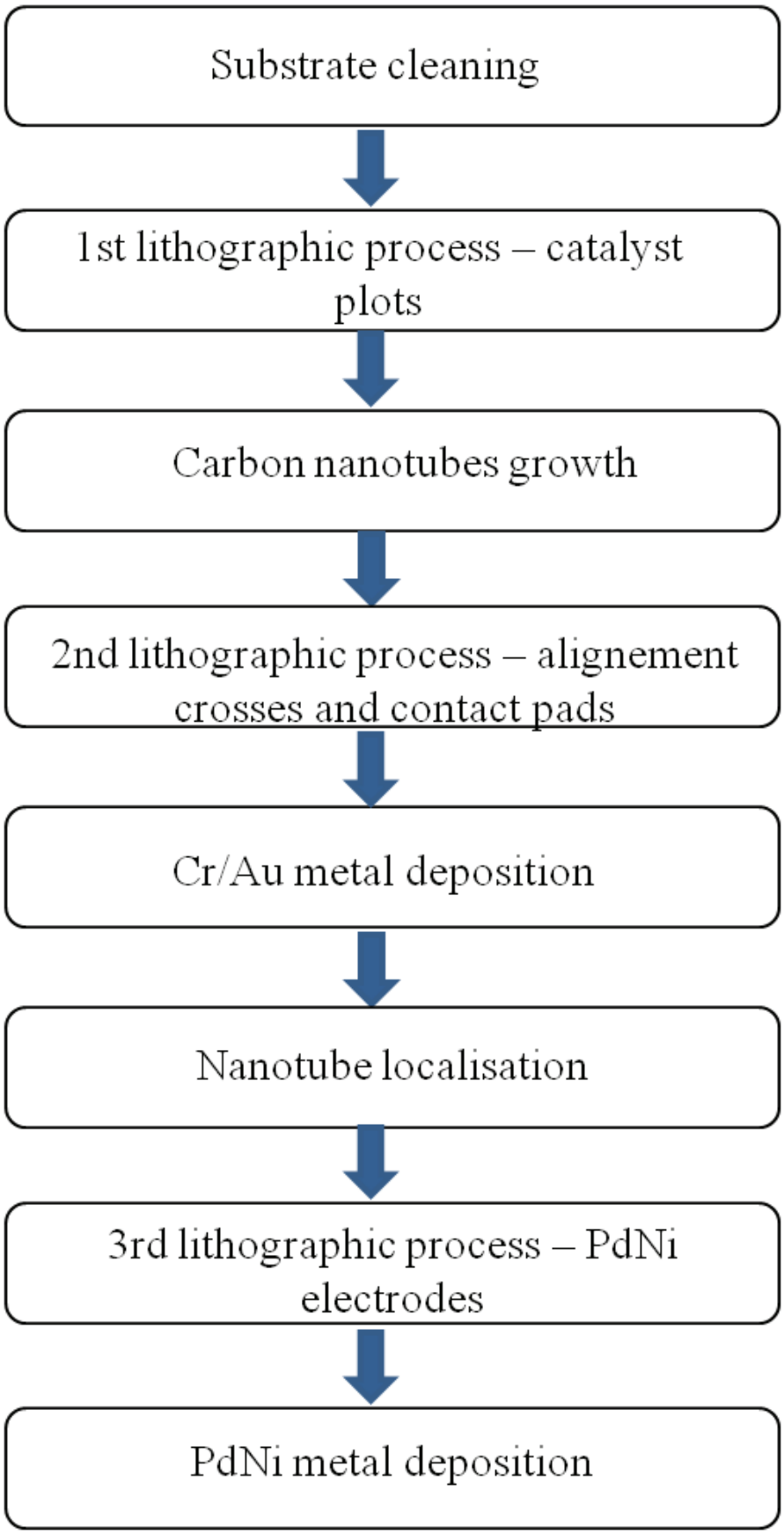

Figure 3.3: *Schematic overview of the sample preparation process.*

As seen in fig. 3.2, during the first lithographic step, are opened various windows in the resist of ~ 1 μm width. These windows will be later filled with catalyst. The recipe of the catalyst used is: 39 mg of Fe(NO_3-H$-$2O), 7.9 mg of MoO_2 and 32 g of Al_2O_3 diluted in 30 ml of IPA. Before using it, one needs to stir the compound for 1h in an ultrasonic bath in order to break the clusters of catalyst into small particles and then to let it rest for 45 minutes. These timings are important in order to obtain a final solution with optimum sized and good concentration catalyst.

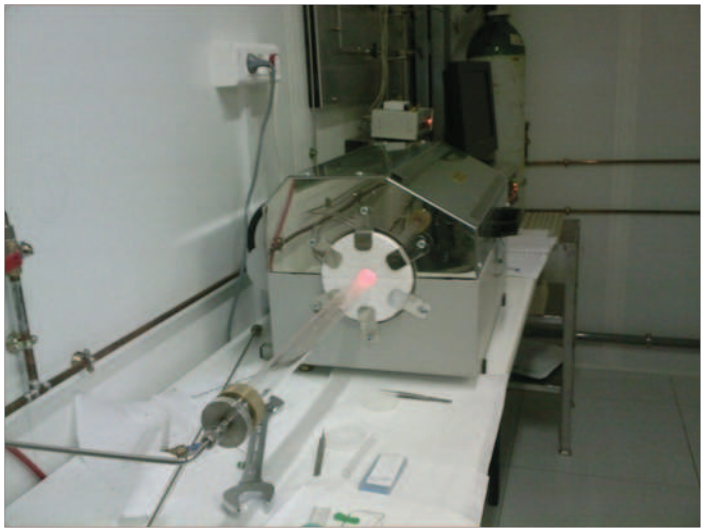

Figure 3.4: *Methane based CVD oven used in the nanotube growth process.*

1 or 2 drops of catalyst (collected mainly from the surface of the solution) on the surface of the sample are enough. The sample needs to be dried immediately after, using a nitrogen gun. The CNT will grow starting from the nanoparticles deposited in the lithography-opened windows. The resist is removed using 4 beakers filled with acetone: the sample is immersed successively, for $30''/60''/90''/3'$ in the beakers. A 5th beaker with IPA is used at the end to ensure the sample is properly cleaned. Further, the sample is introduced in a furnace (see fig. 3.4) that is heated up to 900 C. The sample is exposed to a succession of 3 gases: Ar (as neutral gas), H_2 (as reducer for the catalyst) and CH_4 (as carbon source).

For complete details on the growth parameters used, please, consult table 3.5.

Step	**Time (min)**	**Temperature (°C)**	**Argon (mL/min)**	H_2 **(mL/min)**	CH_4 **(mL/min)**
Purge	3	20	1500	220	1100
Heating	≈ 20	$20 \nearrow 900$	1500	0	0
H_2 flash	8	900	0	220	0
Growth	10	900	0	220	1100
Cooling (Step 1)	≈ 180	$900 \searrow 300$	1500	220	0
Cooling (Step 2)	≈ 60	$300 \searrow 20$	1500	0	0

Table 3.5: *Growth parameters used for SWCNTs.*

3.1.8 PdNi Hall crosses

For the PdNi Hall crosses, the fabrication process detailed in fig. 3.5 is a simplified version of the one described above for the spin-valve device.

Small differences appear in the substrate cleaning process where the sample is sonicated first in acetone for 10 minutes and then in IPA for another 10 minutes to ensure a proper surface. The lithographic processes and the metallizations respect similar principles as the ones described above. In table 3.6 and table 3.7 can be consulted the general parameters used during the metallizations; one can note the gold film fixed by using titanium instead of chromium.

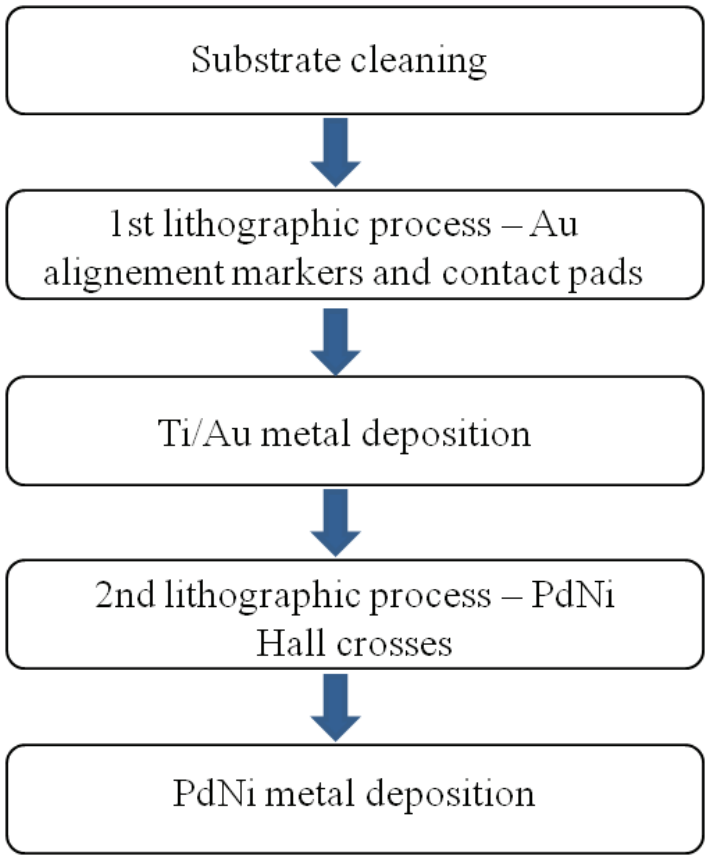

Figure 3.5: *Overview of the sample preparation process for the PdNi Hall crosses.*

Metal	**Pressure (mbar)**	**Current (A)**	**Rate (Å/s)**	**Thickness (nm)**
Ti	$5 * 10^{-7}$	$7 * 10^{-7}$	3	30
Au	$8 * 10^{-7}$	$2 * 10^{-7}$	1.5	$4 - 5$

Table 3.6: *Evaporation parameters for the Au contacting pads and alignment crosses.*

Metal	**Pressure (mbar)**	**Current (A)**	**Rate (Å/s)**	**Thickness (nm)**
PdNi	$5 * 10^{-7}$	$7 * 10^{-7}$	3	30
Pd	$8 * 10^{-7}$	$2 * 10^{-7}$	1.5	$4 - 5$

Table 3.7: *Evaporation parameters for the PdNi Hall crosses.*

3.1.9 Observations on the sample fabrication process

Given the extremely small dimensions of the samples and the multitude of procedures required to obtain them, a series of problems can arise during the manufacturing process. Some key steps that oftenly fail: insufficient/excessive density of CNT's - situation exposed in fig. 3.6, faulty SEM localization of the CNTs due to accumulation of charges on the surface of the sample, problems with PdNi metallization due to a poor choice of lithographic parameters or even issues in reaching an optimal pressure during the evaporation.

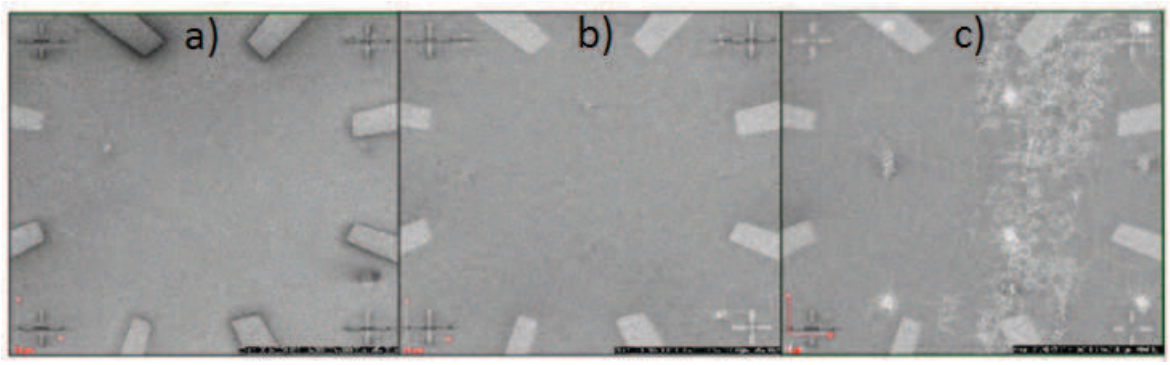

Figure 3.6: *Typical SEM images of different areas of a substrate; (a) very low density of CNT's - insufficient in length to connect them with PdNi electrodes; (b) good density of nanotubes, ready to be connected; (c) very high density of tubes - due to entanglements of the tubes, it is impossible to connect and measure them.*

After the last lift-off process is performed, we glue the sample onto the sample holder and we connect the structures using a micro-bonding machine. Once the structures are connected, all electrostatic variations must be avoided, not to damage the CNTs.

3.2 Measurement techniques

3.2.1 Conductance measurements

Schematically, the setup used to perform the transport measurements is of the type, $F/QD/F$. In chapter 2 was discussed already the conditionsin which a CNT can be considered aproximated by a quantum dot. Assuming such conditions fulfilled, in order to characterize the device's electronic properties, the differential conductance of the system, both in the presence and absence of an external magnetic field can be measured.

For that, one neeeds to apply a gate voltage through the substrate (see fig. 3.7) to control the energy levels of the QD and, also, a source-drain voltage between the two

PdNi electrodes to polarize the system. The local differential conductance is measured by applying a small V_{AC} voltage (with the help of a lock-in amplifier) which is proportional to the alternative current passing through the circuit. The signal obtained at the drain electrode is detected using a current pre-amplifier with a gain of 10^6.

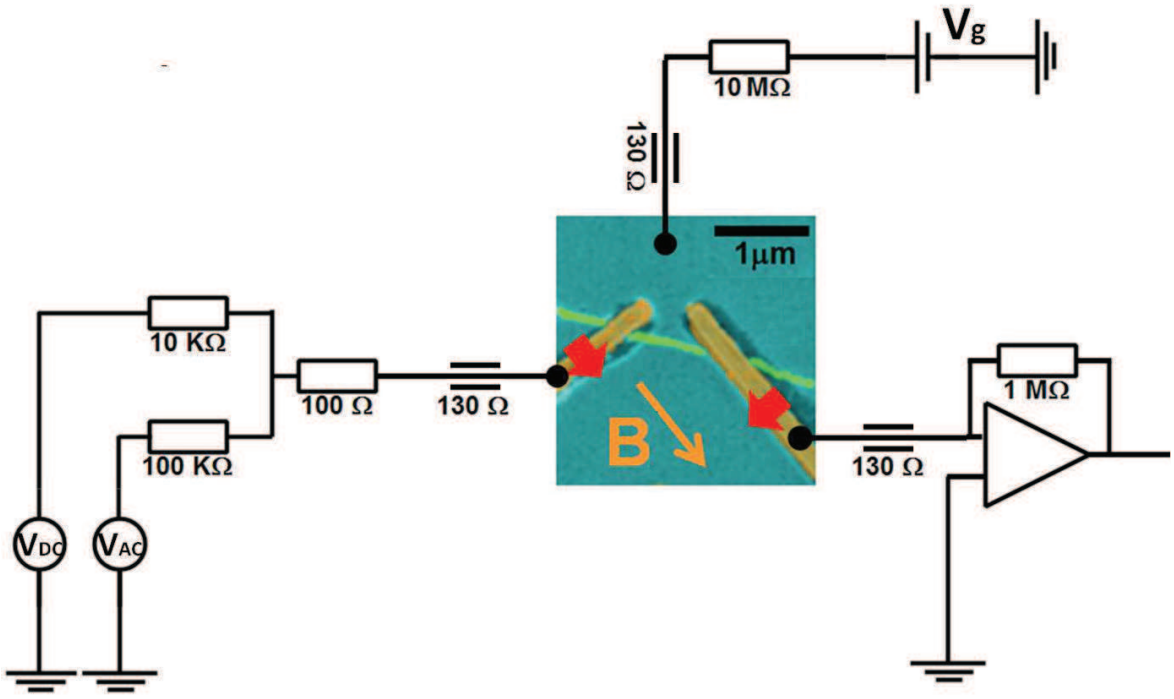

Figure 3.7: *Electrical diagram of the conduction measurements.*

According to the transport properties exhibited by the CNTs, the currents involved are very small, of few pA, so a good grounding of the entire system and a proper amplification of the obtained signal becomes essential.

3.2.2 MFM characterizations

With the purpose to better understand the properties exhibited by the CNT-based system, magnetic force microscopy (MFM) was used to look into the magnetic evolution of the PdNi when shaped in nanometric sized nanostripes.

As investigation technique, MFM is based on a method first introduced by Martin and Wickramasinghe [39] to map the magnetic distribution of a sample using the magnetic force gradient acting between the surface of the sample and the MFM probe. This probe consists of a magnetic tip mounted on a cantilever. Once the tip is brought close enough to the sample ($\sim$ 100 nm), then changes into the cantilever's position occur due to the tip-sample interaction. These changes are optically detected and put together forming a 2D image.

To ease the work, one can exploit the fact that a MFM can be operated in two-pass (tapping-lift) mode or constant height mode to minimize surface topography features on the image of the magnetic forces distribution. The first pass is using the semi-contact (tapping) operation mode to obtain a topography of the surface while the cantilever follows the scan line direction (see fig. 3.8, (a)). At the second pass, the cantilever is lifted above the surface at a required height and follows the topographic contour previously acquired (see fig. 3.8, (b)).

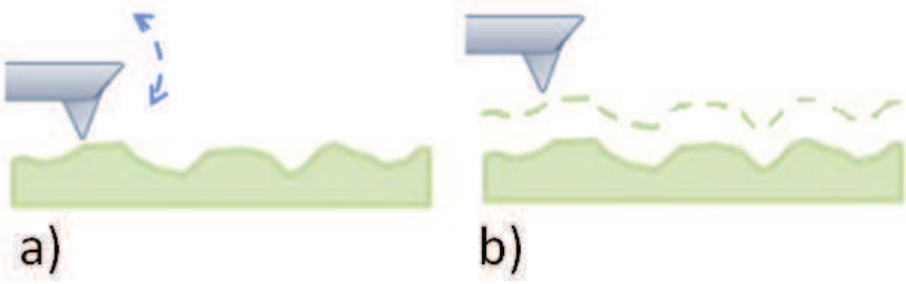

Figure 3.8: *Typical images acquired by MFM technique; (a) topographical profile of the sample; (b) magnetic map of the sample.*

As mentioned above, MFM probes the magnetic force (or gradient) fluctuations of a magnetic sample. The distance between the magnetic probe and the sample surface plays important role because if the tip is brought too close to the sample, the resulting image would be a topographic depiction of the sample mainly because there we would deal also with other tip-sample interactions, like: electrostatic forces or van der Waals interactions, capillary or quantum mechanical (Casimir etc) forces.

However, among all these interactions, the magnetic force, as a long-range force displays a measurable effect in the case of an appropriate tip-sample distance, where the resulting image would be magnetic.

The MFM is used in dynamic mode: the cantilever (and thus the tip) is made to vibrate at its resonance frequency. By measuring the shift in the frequency or the difference in the phase that are induced by the tip-sample interaction, we have direct access to the force acting on the tip. If we consider F_z as being the z component of this force (normal to the surface of the sample), we can write:

$$f_r = f_0 \sqrt{1 - \frac{1}{k} \frac{\partial F_z}{\partial z}} \tag{3.1}$$

where f_r represents the resonance frequency, f_0 is the resonance frequency of the cantilever without any force acting upon and k is the constant of the cantilever. But

as we said earlier, the MFM detects the magnetic force or magnetic force gradient conveying the magnetic interactions between the tip and the sample. Thus we can write the shift in the frequency as:

$$\frac{\Delta f_r}{f_r} = -\frac{1}{2k}\frac{\partial F_z}{\partial z} \tag{3.2}$$

and the phase difference:

$$\Delta\varphi = \frac{Q}{k}\frac{\partial F_z}{\partial z} \tag{3.3}$$

Q is the quality factor of the resonance. Using the approximation that the magnetization of the tip lies only in z direction ($\overrightarrow{u}_z$), we get:

$$\frac{\partial F_z}{\partial z} = \mu_0 m_z \frac{\partial^2 H_z}{\partial z^2} \tag{3.4}$$

where m_z is the z component of the magnetization of the tip multiplied by the volume. Equation (3.4) shows a direct proportionality between the gradient of the force acting on the tip and the magnetic field created by the sample.

We now explain why MFM is a magnetic charges microscope. The magnetization of the tip interacts with the stray field of the sample, the energy of the interaction, E_{int} can be written as:

$$E_{int} = -\mu_0 \int_{tip} \overrightarrow{M}_{tip}\overrightarrow{H}_{sample} dV \tag{3.5}$$

If we write the magnetic field as a derivative of a potential in a zero current density: $\overrightarrow{H} = -\overrightarrow{\nabla}\phi$ and by using the volume magnetic charges definition, $\rho = -M_S div\overrightarrow{m}$ and the magnetic charges specific to the surface $\sigma = M_S\overrightarrow{m}\,\overrightarrow{n}$, we obtain:

$$E_{int} = \mu_0 \int\int\int_{tip} \rho_{tip}\phi_{sample} dV + \mu_0 \int\int_{tip} \sigma_{tip}\phi_{sample} dS \tag{3.6}$$

Equation 3.6 describes the signal recorded by the MFM and it can be used to interpret the contrast obtained in the magnetic images. By taking into account that the signal is proportional to the gradient of the force, then one gets:

$$-\frac{\partial F_z}{\partial z} = \mu_0 \int\int\int_{tip} \rho_{tip}\frac{\partial^2\phi_{sample}}{\partial z^2} dV + \mu_0 \int\int_{tip} \sigma_{tip}\frac{\partial^2\phi_{sample}}{\partial z^2} dS \tag{3.7}$$

This shows that $\frac{\partial^2\phi_{sample}}{\partial z^2}$ is the resolution function of the MFM as a magnetic charges microscope.

3.2.3 Extraordinary Hall effect measurements

Intrigued but not completely satisfied by the preliminary MFM images obtained on the PdNi stripes, further investigations needed to be done in order to comprehend of the evolution of the magnetization with temperature. In this sense, the extraordinary Hall effect (EHE) has been recognized as a useful tool for measuring the magnetic hysteresis $M_z(H)$ loops, for perpendicular magnetization component.

One great advantage of this method represents the easiness of the measurement. In fact, a simple 4 points electrical measurement, in the presence of an external magnetic field, will suffice. The samples measured are crossed-shaped, like the ones presented in fig. 3.9.

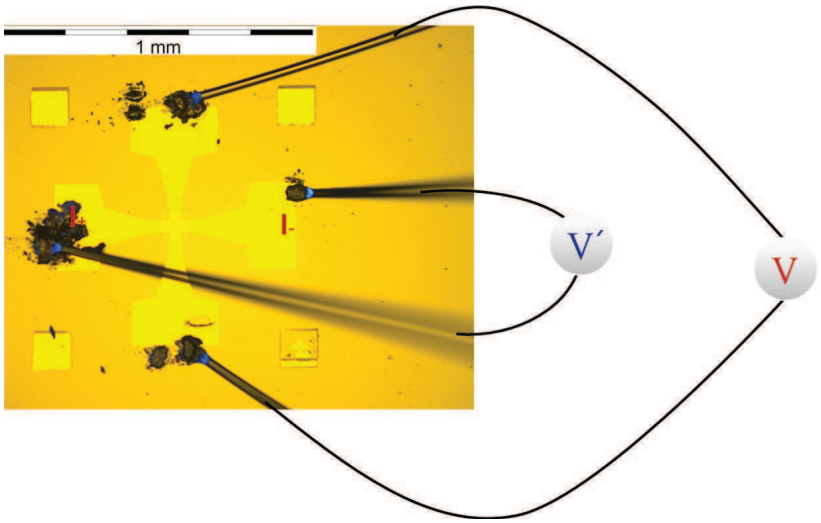

Figure 3.9: *Typical Hall cross sample; image acquired under an optical microscope; the PdNi crosses are connected to Au pads which is further contacted using a microbonding machine to the sample holder of the PPMS; the principle of a 4-points electrical measurement is shown in the image: the voltage difference V is measured while applying an electrical current between the I+ and I− terminals.*

For the measurements presented here, a PPMS (Physical Properties Measurement System) facility was used to collect the data. The PPMS gave the possibility to investigate the evolution of the EHE in a temperature range between 5 K and 300 K and in interval of the field between -9 T and 9 T. A further discussion of the mechanism of the EHE and of the results obtained is extensively presented in chapter 4.

Chapter 4

Magnetic anisotropy in PdNi nanostripes

Anisotropic magnetoresistance, planar Hall effect, spin-dependent tunneling and the extraordinary (anomalous) Hall effect (EHE) are spin-dependent electronic transport phenomena known for many years. However, it is the discovery of the giant magnetoresistance (GMR) that gave birth to the term spintronics and triggered a world-wide expansion of the spin-related research. Recently, much attention has been focused on the electrical conductivity and magnetoresistance of hybrid nanometric structures containing ferromagnetic elements but up until now, it is not entirely clear how other transport properties of such systems are influenced by the ferromagnetic elements.

4.1 General considerations on PdNi anisotropy

4.1.1 General considerations on anisotropy

It has been seen experimentally, that ferromagnetic materials exhibit " easy "and " hard "directions of the magnetization; i.e. the energy required to magnetize a crystal depends on the direction of the applied field relative to the crystal axes. Technologically speaking, this aspect is very important because depending on the type of application, material with high, medium or low magnetic anisotropy can be used for specific application as, for example, permanent magnets, information storage media or magnetic cores in transformers and magnetic recording heads. The physical basis that underlies a preferred magnetic moment orientation in magnetic materials comes from two main sources: the magnetic dipolar interaction and the spin−orbit interaction.

Spins on the other hand, are coupled via the spin−orbit interaction to the orbits which, in turn, are influenced by the crystal lattice. For itinerant electrons the spin−orbit interaction induces a small orbital momentum, which then couples the total (spin plus orbital) magnetic moment to the crystal axes. This results in a total energy which depends on the orientation of the magnetization relative to the crystalline axes

that reflects the symmetry of the crystal. This is known as the magnetocrystalline contribution to the anisotropy. A lower symmetry at the interface strongly modifies this contribution as compared to the bulk, yielding an interface anisotropy.

The spin−orbit interaction, together with the overlap in wavefunctions between neighboring atoms, is also responsible for the magneto−elastic or magnetostrictive anisotropy induced in a strained system, a situation which is frequently encountered in multilayer devices due to the lattice mismatch between the adjacent layers. Strain in a ferromagnet changes the magnetocrystalline anisotropy thus altering the direction of the magnetization. This effect is the inverse of magnetostriction, the phenomenon that changes the sample's dimensions if the direction of the magnetization is changed. The energy for an elastically isotropic medium with isotropic magnetostriction can be written as:

$$E_{ME} = -K_{ME} cos^2(\theta) \tag{4.1}$$

where $K_{ME} = \frac{3}{2}\lambda\sigma$; σ is the stress due to the strain, λ the magnetostriction constant that depends on the orientation and can take positive or negative values while θ is the angle that measures the direction between the magnetization and the direction of the stress.

Last source of magnetic anisotropy is the long range magnetic dipolar interaction, which senses the outer boundaries of the sample. Due to its long range character, the dipolar interaction generally results in a contribution to the anisotropy, which depends on the shape of the specimen. This shape effect in ellipsoidal ferromagnetic samples can be described, with the use of an anisotropic demagnetizing field, H_D, given by:

$$H_D = -\overline{N}M \tag{4.2}$$

where $\overline{N}$ is the shape-dependent demagnetizing tensor and M is the magnetization vector. For a thin film, all tensor elements are zero except for the z-direction, perpendicular to the film. We can express magnetostatic energy density by using:

$$E_D = -\frac{\mu_0}{2V}\int M H_D d\upsilon \tag{4.3}$$

where μ_0 is the permeability in vacuum. Thus the anisotropy energy contribution per unit volume V in a film is given by:

$$E_D = \frac{1}{2}\mu_0 M_S^2 H_D \cos^2\theta \tag{4.4}$$

We assume the magnetization as being uniform with a magnitude equal to the saturation magnetization M_S making an angle θ with the normal to the surface. Thus an in-plane preferential orientation for the magnetization is preferred under the dipolar interaction.

4.1.2 Particularity of the PdNi nanostripes anisotropy

Fig. 4.1 shows a phase diagram for PdNi alloys. It also displays the variation of Curie temperature with the concentration of the two elements. It can be easily seen that for $Pd_{90}Ni_{10}$, the Curie temperature is smaller than $0°$ C (in fact, previous experiments situate Curie temperature for $Pd_{90}Ni_{10}$ at about 120 K), while for $Pd_{20}Ni_{80}$, the same point is reached above well above room temperature (reported at 600 K by Ferrando et al [40]). The obvious facility given by $Pd_{20}Ni_{80}$ is that room temperature techniques can be used to investigate the properties of PdNi-based systems.

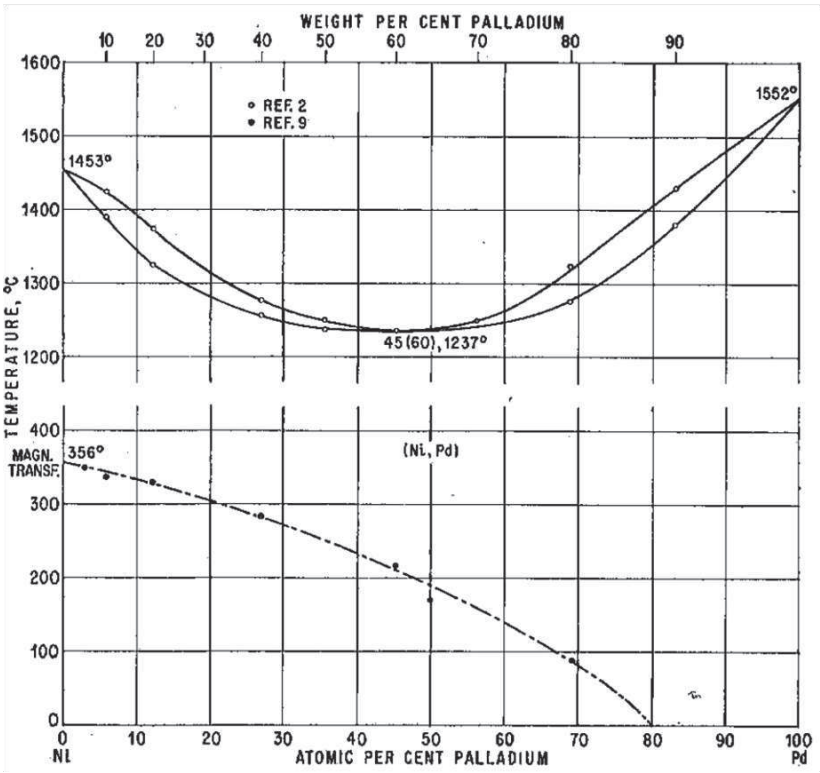

Figure 4.1: *Phase diagram for Pd_xNi_{100-x}; the variations in temperature of the Curie temperature show that a $Pd_{20}Ni_{80}$ is easier to investigate due to Curie point situation well above room temperature in contrast with $Pd_{90}Ni_{10}$ that has a Curie temperature much below the $0°$ C. Image taken from "Constitution of Binary Alloys" by M. Hansen [41].*

A very good example in this sense are the recent experiments conducted by Jean-Yves Chauleau et al [3], who found peculiar magnetization textures upon the investigation of $Pd_{20}Ni_{80}$ nanostripes. They used different imaging techniques (MFM, XMCD-PEEM and SEMPA) to study the surprising transversal orientation of the magnetization both with temperature and with geometric variation of the samples. A magnetic field has also been applied, showing that the magnetization textures under study are not simple metastable states due to growth conditions.

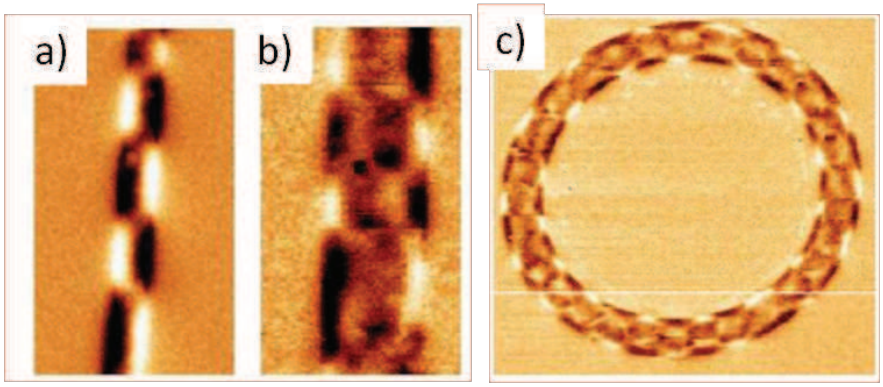

Figure 4.2: *Selection of MFM images on different* $Pd_{30}Ni_{70}$ *nanostructures; the orientation of the magnetization along the hard axis of the system is obvious. (a) nanostripe of* 150 *nm wide and* 30 *nm thick; (b)* 450 *nm wide and* 30 *nm thick nanostripe; (c) nanorings with a diameter of* 5 μm*, a width of* 500 *nm and a thickness of* 30 *nm.*

MFM imaging have shown in 30 *nm* thick stripes, fig 4.2 (a), alternate edge magnetic charges. The obvious correlation between the two sides, having opposite magnetic charges facing each other corresponds to magnetic domains with a transverse magnetization, an orientation orthogonal to easy axis of the stripe i.e. the distribution meant to minimize the magnetostatic energy (shape anisotropy). For wider stripes, fig. 4.2 (b), an inner contrast also appears, revealing a more complex distribution of the magnetization that, obviously, is not entirely along the transverse axis. Nevertheless, the existence of an important transverse component is probed with the use of a ring-shape, sample fig. 4.2, (c). These magnetic structures differ from the images taken on thin film samples.

Since MFM probes only the sample magnetic stray field (and only for one surface of the sample), Chauleau et al used also XMCD-PEEM imaging to probe the magnetic structures both at 300 K and 150 K. Circularly polarized X-rays are falling on the sample at a 16° angle from the surface; differential absorption of the X-rays proportional to the dot product of magnetization and photon wavevector give a different contrast along the samples. The magnetization images are obtained by forming the difference of PEEM images acquired with opposite helicity of the X-rays. This method is restricted by the energy of the collected electrons to probe only the surface of the samples, up to few nanometers in depth.

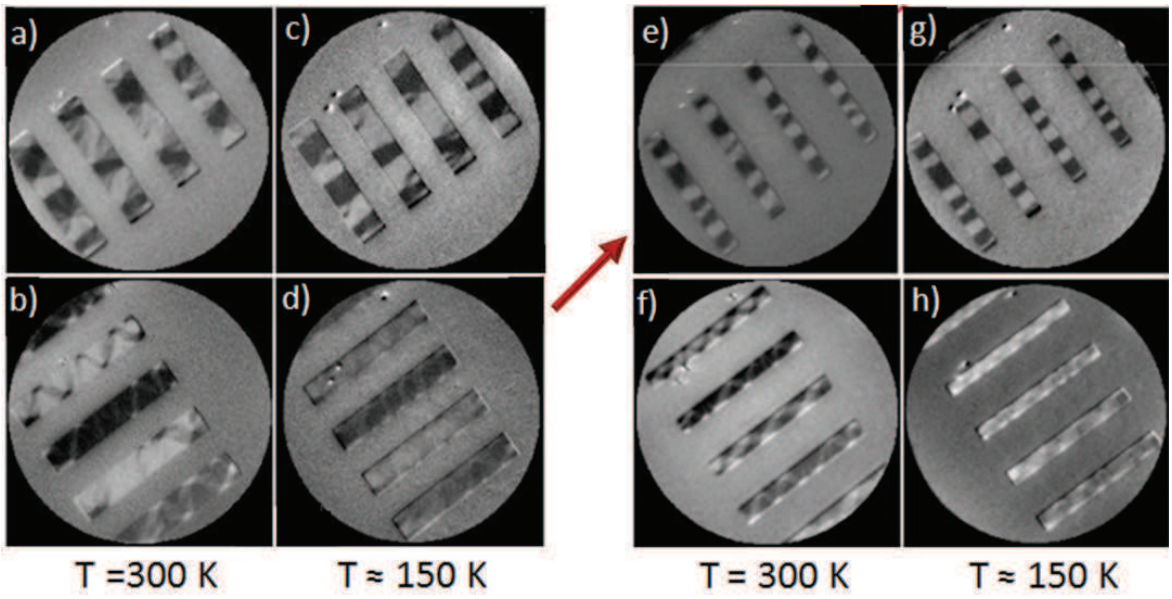

Figure 4.3: *XMCD-PEEM images of* 5 μm *long and* 30 nm *thick* $Pd_{20}Ni_{80}$ *structures, taken at room temperature (columns one and three) and at low temperature (*$\sim$ 150 K *column two and four). Two series of widths are shown, namely* 1μm *to* 0.85 μm *(in the first two columns) and* 0.6 μm *to* 0.45 μm *(in columns three and four), both with a* 50 nm *step. The magnetization components are probed using an X-ray beam oriented according to the red arrow.*

In fig. 4.3 can be seen images from large (from 1 μm to 0.85 μm) and intermediate (from 0.6 μm to 0.45 μm) width nanostructures, having a thickness of 30 nm. These results confirm the interpretation of the images obtained with MFM technique. Fig. 4.3 (a), (e) display a strong transverse component having an increasing complexity with width. The magnetic contrast in the images observed longitudinally, fig. 4.3 (b), (f), show a magnetization not fully transverse. Deformations of the so-called diamond structure appear (see fig. 4.3, (f)), for 500 nm and 600 nm width where closure domains on the long edges with one (longitudinal) magnetization are bigger than for the opposite magnetization, meaning that such structures have a longitudinal moment. At large widths (see fig. 4.3, (b)), this deformation is more pronounced, nevertheless the proximity of the structures determines a dipolar coupling responsible for stabilizing a longitudinal magnetization structure. The alternation of bright and dark overall contrasts attest to that. This dipolar coupling gives rise to an applied field along the longitudinal direction.

Images taken at 150 K show that this peculiar magnetization changes strongly with temperature. Fig. 4.3 (c), (d), (g), exhibit a magnetic distribution much simpler with respect to the one at 300 K; the disappearance of the intermediate grey levels point to an reinforcement of the transverse anisotropy. This hypothesis is backed up also by the low contrast obtained in the images probing the longitudinal component (fig. 4.3, (d) and (h)).

As the shape anisotropy increases as temperature decreases, Chauleau et al explained the results by a thermal stress mechanism related to magnetostriction. The same mechanism was invoked for explaining the spin reorientation transition observed in $Ni_{1-x}Pd_x$ alloys grown on $Cu_3Au(100)$ by Biehler et al [42]. Moreover, elastic, magneto-elastic and micromagnetic simulations reproduced qualitatively the features of the experiments. According to this mechanism, a transverse anisotropy appears at the edges of the structure due to stress relaxation (as no relaxation can occur in the longitudinal direction, this becomes the hard in-plane direction at the edges).

4.1.3 Normal Hall effect and the extraordinary Hall Effect

Hall effect appears when an electric current flows through a conductor placed under an transversal external magnetic field. The force exerted by the field will determine a redistribution of the charge carriers towards one of the sides of the sample thus a difference in voltage between the two sides of the sample will appear. By measuring this difference in voltage, one can get information on both the nature and the quantity of charge carriers. When dealing with ferromagnetic materials, as PdNi, the Hall effect shows some anomalous characteristics. In fact, it is commonly described by the phenomenological equation:

$$\rho_H = R_0 B + R_{EHE}\mu_0 M = R_0\mu_0[H + M(1 - D)] + R_{EHE}\mu_0 M \tag{4.5}$$

where ρ_H is the Hall resistivity, B, H and M are components of the magnetic induction, applied field and magnetization normal to the film plane, and D is the demagnetization factor normal to the plane. R_0 is the ordinary Hall coefficient related to the Lorentz force acting on moving charge carriers. R_{EHE}, the extraordinary Hall coefficient, is associated with a break of the right-left symmetry at spin-orbit scattering in magnetic materials. Demagnetization factor D is equal to 1 when field is applied perpendicular to a homogeneous magnetic film. Hence it remains only:

$$\rho_H = R_0 B + R_{EHE}\mu_0 M \tag{4.6}$$

Voltage measured between Hall contacts located perpendicular to the direction of an electric current is given by:

$$V_H = \frac{I}{d}\rho_H = \frac{I}{d}(R_0 B + R_{EHE}\mu_0 M) \tag{4.7}$$

where I represents the current and d the thickness of the film.

It is generally accepted that EHE in ferromagnetic metals originates from the spin-orbit scattering that breaks a spatial symmetry in the trajectory of scattered electrons. Two main types of scattering events are distinguished in the EHE. One is referred to as skew scattering and is characterized by a constant spontaneous angle at which the scattered carriers are deflected from their original trajectories. The origin of this

mechanism relies in the spin-orbit coupling of the electron-impurity. The correlation between the EHE coefficient and resistivity is expressed as $R_{EHE} = A\rho + B\rho^2$. The second term is frequently neglected and a linear ratio between R_{EHE} and ρ is mentioned. In fig. 4.4 is presented a schematic illustration of the skew scattering mechanism.

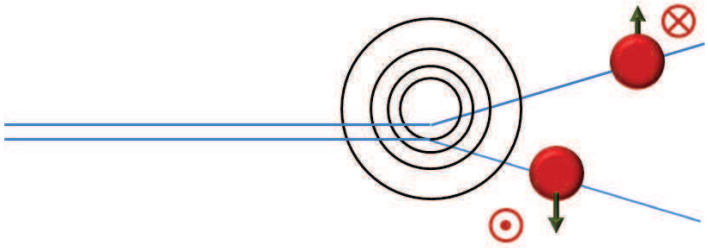

Figure 4.4: *Illustration of the skew scattering mechanism. The spontaneous angle at which the scattered carriers are deflected from their original trajectories is constant.*

The other scattering mechanism, so-called side jump, is quantum in nature and results in a constant lateral displacement of the charge trajectory at the point of scattering. For the side jump process $R_{EHE} \propto \rho$, and it is expected to dominate in highly resistive samples at elevated temperatures or with highly doped materials. In fact, the electron wave is shifted in opposite directions by the opposite electric fields upon approaching and leaving the impurity. A schematic picture of the mechanism is presented in fig. 4.5.

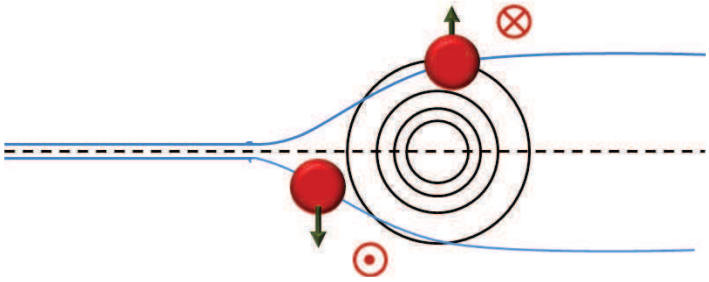

Figure 4.5: *Illustration of the side jump mechanism; when a polarized electron is approaching an impurity, a constant lateral displacement of the charge trajectory takes place.*

Together with the skew scattering and the side jump, we have also the intrinsic deflection. It gives rise to a velocity contribution, perpendicular to the field direction. In ferromagnets the average effect is different from zero.

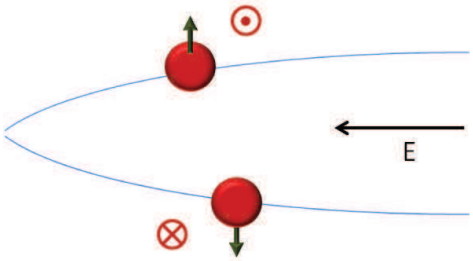

Figure 4.6: *Illustration of the intrinsic deflection phenomena that gives a velocity perpendicular to the field direction.*

4.2 Experimental results

The possibility to control the orientation of the magnetization in ferromagnetic electrodes is of crucial importance for producing efficient quantum spin-transfer-based devices. At such small scales, all sorts of effects (Oersted fields, for example) could influence the behavior of such a device. For that, a good knowledge of the magnetic properties of PdNi alloy when shaped in stripes of micrometric/nanometric sizes holds an important place.

The spin transfer effect has been shown to give rise to coherent magnetization dynamics (for example domain wall dynamics) in a variety of magnetic devices and materials. Most of the initial work focused on the dynamics excited for in-plane magnetized films. Structures based on perpendicularly magnetized components have the additional advantage feature that its dynamics can be induced using applied fields that are relatively low compared to the saturation magnetization. In this case, domain wall width is much smaller despite the larger propagation field. For example $Pt/Co/Pt$ ultrathin films (below 1 nm Co) show a propagation field bigger than 100 Oe while the anisotropy is bigger than 1 T; the domain wall width $\sim$ 5 nm, thus displaying a big spin transfer torque phenomena, compared to permalloy where the domain wall width is of several tens of nanometers.

This investigation had as a departure point previous experiments done by Feuillet-Palma et al [4] that were consistent with a transverse magnetization in PdNi nanostripes used to contact CNT's in order to measure transport effects in a spin valve like device. This result was intriguing, so Chauleau et al [3] used imaging techniques to give an answer for the unusual axis of magnetization. Here, we go one step further and using electrical measurements we try to investigate how different parameters influence the magnetic behavior of the nanostripe-shaped PdNi. Our investigation show that the geometry, thickness and chemical composition together with capping layer used to protect the PdNi against oxidation, they all matter when choosing the right parameters for the electrodes.

Hall effect measurements have been used to detect the out-of-plane magnetization in micrometric and nanometric cross-shaped PdNi samples revealing an extraordinary Hall effect due to the perpendicular component of the magnetization; of course, by looking at the hysteresis curves we can deduce also the in-plane magnetization of the system. Every system has a so called easy axis of magnetization that depends on its anisotropy. When a large magnetic field, H, is applied along the easy axis, the magnetization, M, will align with this field in order to lower the Zeeman energy of the system. A magnetic field applied in the opposite direction will cause the magnetization to reverse after the field crosses its "coercivity" value which depends on the height of the magnetic anisotropy energy barrier. Thus, hysteresis loops having a rectangular shape because of magnetic remanence, and a higher coercive field when an out-of-plane magnetic field is applied, correspond to an out-of-plane magnetization of the samples. On the other hand a closed loop, with no remanence, is clue for an in-plane type of magnetization.

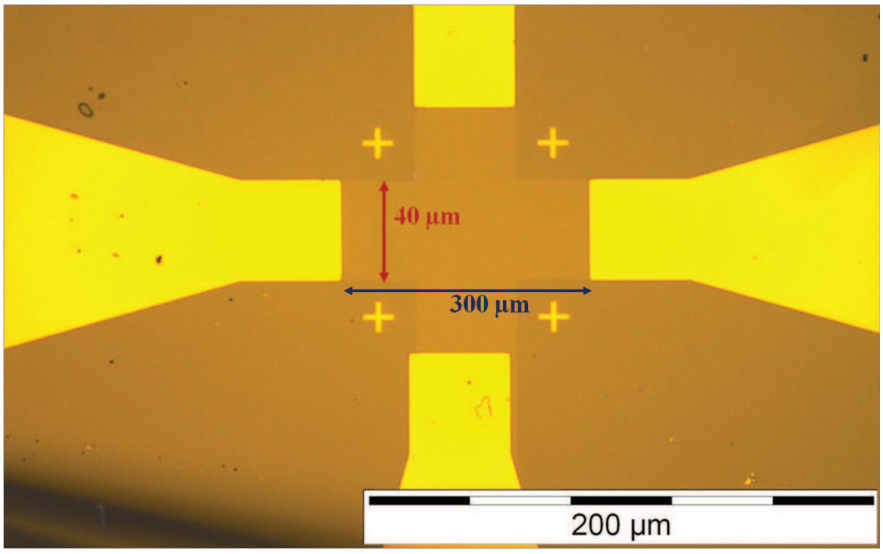

Figure 4.7: *Typical sample. Picture acquired under optical microscope displaying a Hall cross pattern; Au leads are used for electrical measurements and Au crosses are used for a proper alignment during various lithographic steps. The specific dimensions of the sample are also introduced.*

The samples measured during this work look typically like the one presented in fig. 4.7. The Hall crosses have 40 μm in width and a length of 100 μm. Note also that nanometric sized samples with 300 nm in width and 2 μm in length were investigated. The thickness of PdNi varied between 5 and 15 nm. Capping layers of aluminium, palladium and samples without capping were probed. All samples were fabricated on a Si substrate and structured via electron beam lithography and lift-off process as described in Sample Preparation chapter. The deposition of the thin films was done

using evaporation techniques. Au leads are attached to the PdNi crosses as contact pads for electrical measurements; small Au crosses are used to align the patterns during the various steps of lithography. Both $Pd_{90}Ni_{10}$ and $Pd_{20}Ni_{80}$, types of alloy were tested.

Measurements were performed in a PPMS facility that allowed resistivity measurements between 300 and 4 K and the use of a sweeping magnetic field between ± 9 T. It is worth mentioning here that this study was done in collaboration with Keisuke Yamada, post-doc at LPS-Paris XI at that time.

An important remark to be taken into account all along this chapter is that the sign of the EHE hysteretic curves holds no physical interest in our case.

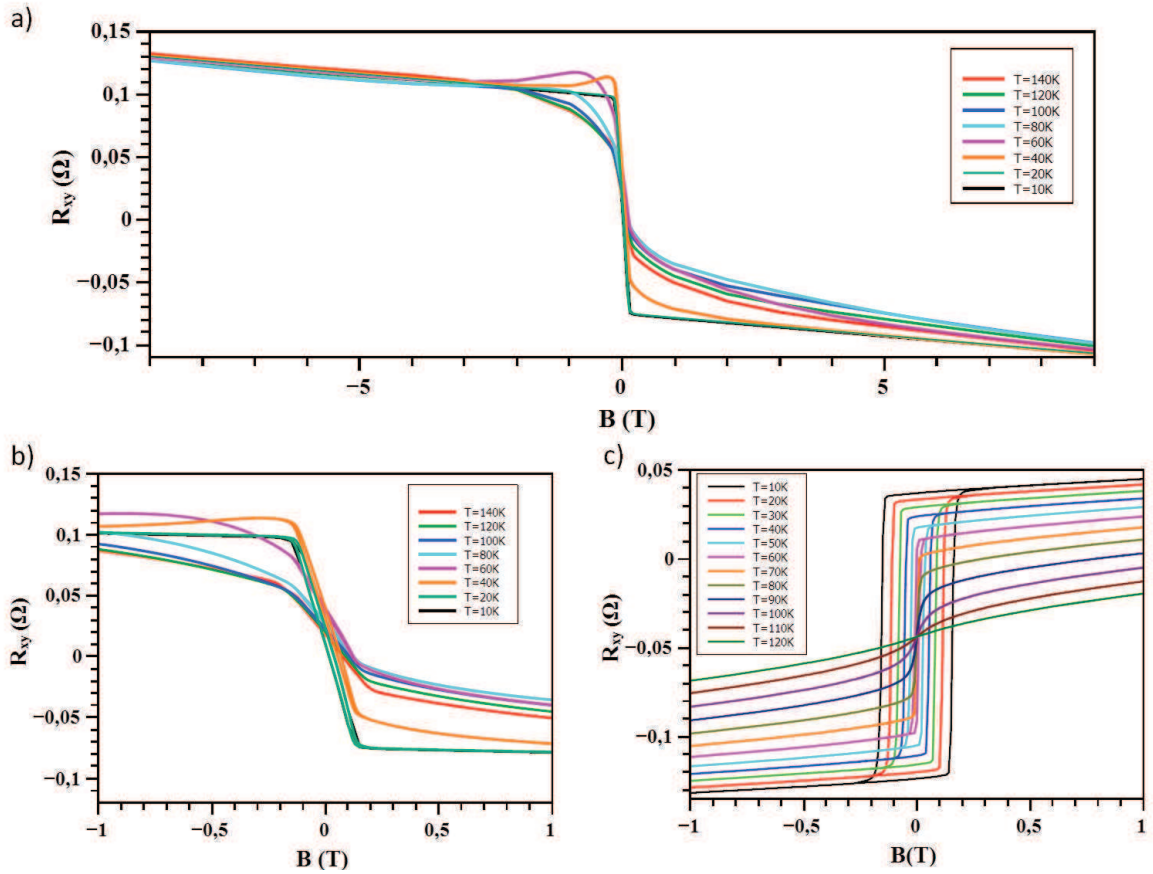

Figure 4.8: *(a) Measurements performed on $Pd_{20}Ni_{80}$ for temperatures between 10 K and 140 K in a field up to 9 T, revealed closed, slanted hysteretic loops. The lack of remanent magnetization is evidence for the in-plane magnetization alignment of the sample; (b) Zoom on the measurements presented at point (a) for field values between -1 T and 1 T; (c) $Pd_{90}Ni_{10}$ for the same interval of temperatures - an evolution from in-plane to out-of-plane magnetization of around 60 K is seen.*

4.2.1 Role of chemical composition

A first question that we asked ourselves was what is the influence the proportion of Pd in PdNi alloy on the anisotropy of ones' samples? For that, both, $Pd_{90}Ni_{10}$ and $Pd_{20}Ni_{80}$ were investigated. Measurements performed on $Pd_{20}Ni_{80}$ for temperatures between 10 K and 140 K in a field sweeping between -9 T and 9 T, see fig. 4.8, (a), show a saturation field between 100 and 200 mT that increases with the increase of the temperature induction. The zoom presented in fig. 4.8, (b), reveales closed, slanted hysteretic loops. The lack of remanent magnetization is evidence for the in-plane magnetization alignment of the sample, even at the lowest temperatures.

When tracing the hysteretic curves for $Pd_{90}Ni_{10}$, see fig. 4.8, (c), for the same interval of temperatures, one can see an evolution from in-plane to out-of-plane magnetization at around 60 K. At 10 K, the anisotropy of the system is fully perpendicular

to the film plane. An increase in the coercive field with the decrease of temperature is emphasized.

An important aspect when considering the transition from $Pd_{20}Ni_{80}$ to $Pd_{90}Ni_{10}$ is lower magnetization of the latter alloy (average atomic moment $\mu = 0.6\ \mu_B$ for $Pd_{20}Ni_{80}$ while $\mu = 0.25\ \mu_B$ for $Pd_{90}Ni_{10}$ as Fischer et al reported [43]), thus a smaller demagnetization energy for the $Pd_{90}Ni_{10}$. On the other hand, magnetostriction initially increases with the increase of the Pd percentage in the compound. So, when analyzing $Pd_{90}Ni_{10}$ we have a smaller demagnetization while more anisotropy in the system thus a bigger chance to observe an out-of-plane easy magnetization.

Following the reasoning of the advantageous out-of-plane magnetization of such electronic device components, it is rightful to say that $Pd_{90}Ni_{10}$ is more suited for spin-based devices than $Pd_{20}Ni_{80}$. Using this logic, from this point on, the research efforts during this work concentrated on studying in more detail $Pd_{90}Ni_{10}$-based structures.

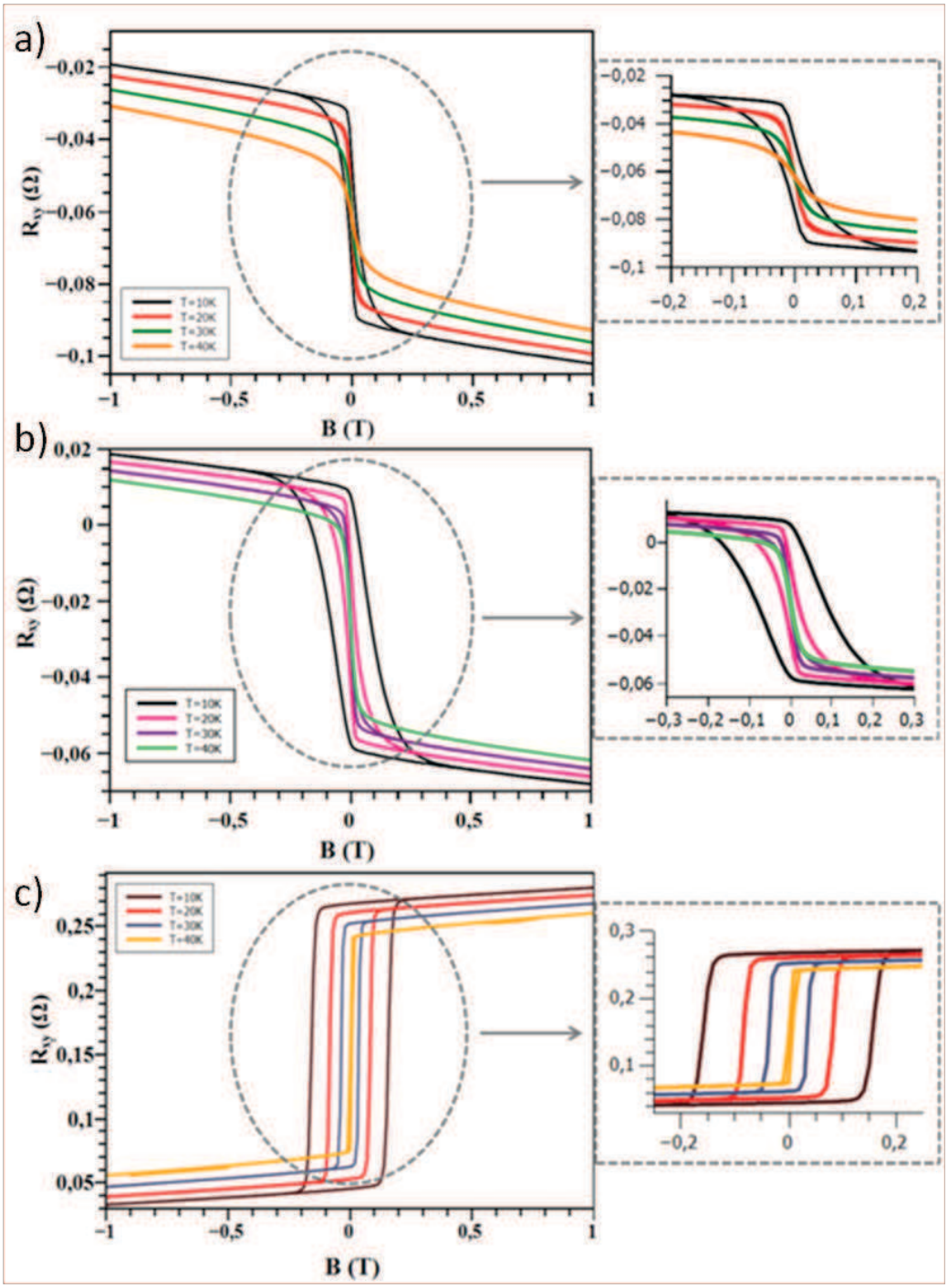

Figure 4.9: *Capping effect on $Pd_{90}Ni_{10}$ Hall crosses of* 10 *nm of thickness; (a) sample not having a capping layer - oxidation phenomena is avoided by performing the measurements immediately after the sample is produced - EHE measurements for temperatures between* 10 *and* 40 *K highlight no hysteretic or very weak hysteretic signal, thus the magnetization does not turn out-of-plane; (b) sample covered with* 3 *nm of Pd layer, the hysteretic behavior becomes more prominent with the decrease of the temperature and in the same time is more accentuated than in the case of the sample with no capping; (c) sample covered with* 3 *nm of Al layer, EHE hysteretic behavior increases with the decrease of the temperature and it turns out-of-plane at* 40 *K.*

4.2.2 Capping layer effect

Fig. 4.9 displays Hall loops taken at different temperatures for samples having a thickness of 10 nm of $Pd_{90}Ni_{10}$ in a field sweeping between $\pm 1\ T$. Each set of measurements corresponds to different capping layer applied on the PdNi to protect it from oxidation. Fig. 4.9, (a), has no capping layer on top of the PdNi sample, oxidation phenomena being avoided by performing the measurements immediately after the sample is produced. Hysteresis loops for temperatures between 10 and 40 K show reversible characteristics (no hysteresis) or very weak hysteretic signal, that increase with the decrease of the temperature. A small hysteretic signal appears only at $T = 10\ K$ but the small coercive field value still indicates an predominant in-plane component for the magnetization.

In fig. 4.9, (b), the PdNi sample is covered by a 3 nm of Pd layer. Hysteresis loops for temperatures between 10 and 40 K show the hysteretic behavior becomes more pronounced with the decrease of the temperature and in the same time is more accentuated than in the case of the sample with no capping, thus a more important out-of-plane component of the magnetization.

EHE measurements on PdNi sample covered with 3 nm of Al layer (fig. 4.9, (c)) show a hysteretic behavior that increases with the decrease of the temperature and that turns out$-$of$-$plane at 40 K.

These results can be explained by various phenomena, like: the presence of an interface anisotropy, the additional stress provoked by differences in the thermic dilatation constant between the materials or by an intermixing effect that has been shown possible between Pd and PdNi (see fig. 4.1). Interface anisotropy appears at the surface, creating an additional anisotropy that does not depend on the thickness of the sample, so that the average sample anisotropy has a $1/thickness$ term. Thus a thickness dependence of the magnetization properties, presented in continuation is the best way to investigate such possibility.

A quick look at the thermic dilatation constants for Si $(2.6 * 10^{-6}\ K^{-1})$, Ni $(13.4 * 10^{-6}\ K^{-1})$ and Al $(23.7 * 10^{-6}\ K^{-1})$, shows a big difference between the two capping layers used in this experiment, in fact the dilatation constant of Al is almost double the one of Ni, making the additional stress due to such differences a possible reason for the results presented above.

Finally, intermixing effects between Pd and PdNi layers were reported in the past, that could cause a change in the magnetic behavior of this films, but such a hypothesis is difficult to verify.

The practical conclusion of the capping effects data is that Al-covered samples have

an out-of-plane orientation, at higher temperatures than the other possibilities investigated (Pd capping and no protective layer).

4.2.3 Thickness effects on PdNi

A study of the thickness influence over the orientation of the magnetization in PdNi microstripes was conducted on samples having 5, 10, 15 nm of $Pd_{90}Ni_{10}$, all having a 3 nm capping of Al. Fig. 4.10 displays the results obtained for the three samples in a temperature interval of $5 - 40$ K for the samples exposed to sweeping a external field up to ± 1 T. Fig. 4.10, (a) shows the results corresponding to 5 nm of PdNi. These EHE measurements highlight non hysteretic loops, that correspond to in-plane type of magnetization even at 5 K. Things start to change for the 10 nm sample where a small out-of-plane component is registered at 5 K. We notice the transition towards out-of-plane magnetization that accentuates with the decrease of the temperature (see fig. 4.10, (b)). The 15 nm sample presented in fig. 4.10, (c) exhibits a clear out-of-plane magnetization even at 40 K and the remanent coercivity continuously increasing as the temperature decreases.

A possible explanation for such behavior can be given considering the high temperatures during the thin film evaporation process of PdNi together with the PdNi/substrate mismatch tensile stress that is imprinted on the metal layer when the sample is cooled down. The thicker the sample, the longer the deposition time thus more heating of the sample during this process and longer cooling down process. Edge effects at the extremities of the sample can be neglected due to the big dimensions of the Hall crosses. Also, any dislocation effects that could appear when above a critical thickness are not visible, making one believe we are in the case of a thickness smaller than this critical value.

This discussion suggests that a good test, not performed yet, is to do the metallization using a sequential growth process: every few nanometers of metal deposed, the sample will be cooled down, before a second/third so on deposition step.

At this point, given the results showing an obvious dependence of the magnetization direction with the sample thickness, one can conclude that interface anisotropy is not responsable for the results obtained in the experiments concerning different capping layers. In the light of such evidence, the additional stress due to differences in the thermic dilatation constant between different materials seems the most plausible explanation for the results presented in this chapter.

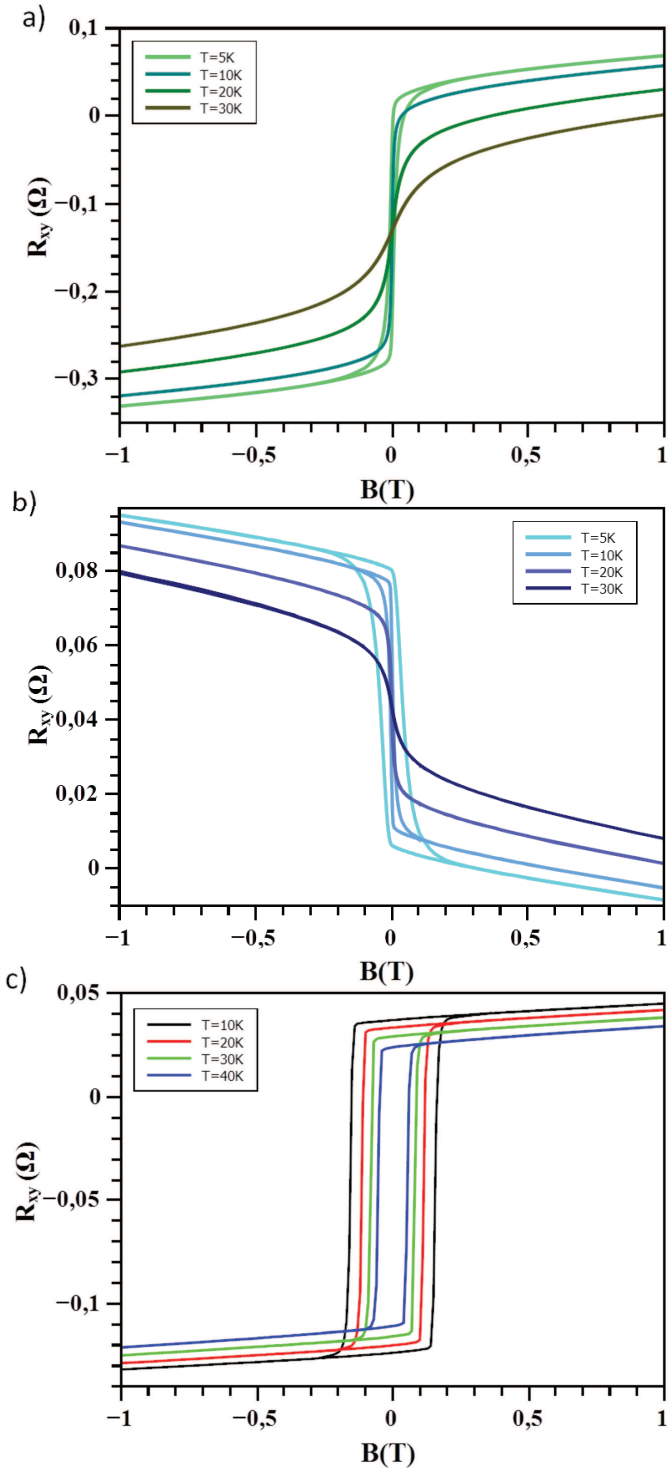

Figure 4.10: *Thickness effect on $Pd_{90}Ni_{10}$ Hall crosses magnetization when in external field; (a) sample of 5 nm of PdNi with a 3 nm capping of Al - EHE measurements for temperatures between 5 and 30 K highlight a non hysteretic signal, mark of a in-plane type of magnetization; (b) sample 10 nm of PdNi with a 3 nm capping of Al, the hysteretic behavior appears at 5 K while at superior temperatures the EHE signal shows a reversal characteristic with the external field; (c) sample 15 nm of PdNi with a 3 nm capping of Al, EHE hysteretic behavior already present at 40 K and loops become broader with the decrease of the temperature - the magnetization has a clear out-of-plane orientation.*

4.2.4 Nanometric samples

Measurements on a nanometric sample (with a width of the Hall cross of 300 nm) were performed. Fig. 4.11, (b) shows the Hall loops corresponding to a temperature interval between 10 and 60 K for such sample. It can be noted the transition from in-plane to out-of-plane magnetization that starts around 40 K. The coercive field H_c and the remanent magnetization, increases as the temperature decreases.

As said in Sec. 4.1.3, if the stripe is as narrow as it is thin, the relaxation of transversal stress takes place across the entire strip. Therefore, thermal strains do lead to out-of-plane and transverse anisotropies, that vary with position, the transverse anisotropy being a side-effect of the perpendicular anisotropy. In addition, the average value of the latter will depend on the aspect ratio of the strip cross-section since it rests on edge contributions.

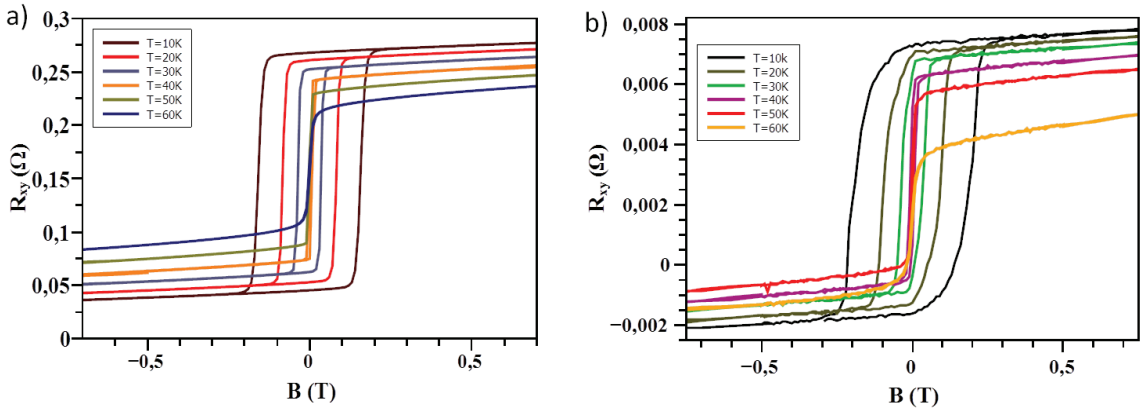

Figure 4.11: *EHE measurements on $Pd_{90}Ni_{10}$ samples. (a) measurements performed on a micrometric-sized sample between* 10 *and* 60 K *highlighting a hysteretic signal for temperatures below* 40 K*; (b) hysteretic signal recorded on a nanometric sample for the same temperature interval as for the micrometric one, with a hysteretic signal for temperatures below* 40 K*, presenting a rounded shape due to lower remanence magnetization than in the micrometric case.*

A comparison between hysteretic loops obtained for the micrometric (fig. 4.11 (a)) and nanometric samples (fig. 4.11 (b)) show a disappointing result: the hysteretic signal in the nanometric samples show a rounding that translates into a lower remanence of the magnetization, that is a less perpendicular component of the magnetization due to board constrictions expected for such small sized samples. Preliminary micromagnetic simulations link this phenomenon to the transverse anisotropy at the edges, that favors magnetization reversal.

4.3 Conclusion

An investigation of PdNi alloy using EHE measurements to put in evidence the out-of-plane component of the magnetization was done. The study concentrated on $Pd_{20}Ni_{80}$ and $Pd_{90}Ni_{10}$. In the case of $Pd_{20}Ni_{80}$, this experiment is a first at low temperature and results show that, even at $T = 10\ K$, the magnetization remains in plane. The result is very helpful for the second part of this work, the one concentrated on quantum spin-valve effect since an in plane magnetization translates into a small stray magnetic field exerted by the two ferromagnetic leads.

The influence of different parameters on the magnetic behavior of the nanostripe-shaped PdNi was investigated. The measurements show the geometry, thickness and chemical composition together with capping layer used to protect the PdNi against oxidation, are key parameters when choosing the right characteristics for a spin-based device. Experiments done on nanometric sized Hall crosses show an out-of-plane component of the magnetization at small temperatures (below 40 K), but less than in the case of the micrometric samples. This is due to the stress relaxation at the edges that becomes important in such small devices.

Extraordinary Hall measurements confirm in all aspects that the magnetic preferential direction of high aspect ratio PdNi contact stripes feature a magnetically easy axis transverse to the strip orientation. Furthermore experimental proof for the model proposed by Chauleau et al [3] sustaining a magnetically easy axis, transversal to the strip orientation due to shape anisotropy. A perpendicular component magnetization effect was recorded, but according to Chauleau et al the edges remain transverse while the core of the stripe will turn out-of-plane.

According to all these results, for the CNT based spin devices, it is therefore recommended to use a Ni-rich alloy for the electrodes connecting the CNT, due to the in-plane orientation of the magnetization that will produce a smaller stray field. Also, best is to apply external magnetic fields in transverse direction to the magnetization of the electrodes in order to obtain a distinct switching behavior.

Chapter 5

Non-collinear magneto-electronics in nanoscale conditions

Spin transport laws radically change when devices have nanometric dimensions. This allows to gain control over multiple characteristics which concede one to obtain new functionalities that would enable the birth of new generations of spintronic devices such as spin field effect transistors. For devices exploiting actively the electronic spin however, control over classical or quantum rotations has to be achieved. In conductors exhibiting many conduction channels, like nanopillars, magnetic stripes or metallic quantum point contacts, where spin transport is of diffusive kind, governed by the classical laws, such control is obtained by manipulating the spin transfer torque phenomenon ([44], [45], [11]). The question that arises now is: what happens when the spin current is carried by a single energy level?

The interest of such question is both of fundamental nature, connected to real spin manipulation in nanoscale conductors and of practical one since such device could be the answer to a number of problems that currently spintronic devices are still facing, like: heating and Oersted field related effects.

Two transport regimes were observed on such devices, depending on the applied gate voltage: the Coulomb blockade regime and the Fabry-Perot regime. They are discussed one after the other in the following pages.

5.1 Coulomb blockade regime

This chapter presents a full transport study of a device stable enough to conduct various transport measurements in presence/absence of gate voltage, source-drain voltage and external field conditions. It is important to mention that measurements were conducted with the help of Shubadeep Datta, post-doc at LPA at that moment.

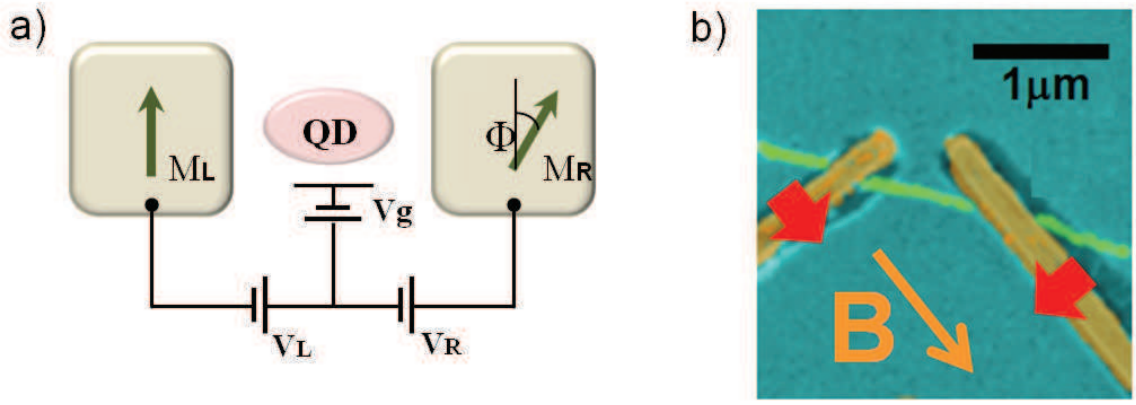

Figure 5.1: *(a) Schema of a quantum dot connected to two non-collinear leads; the device acts like a spin-valve with non-collinear magnetic leads, with a finite tunneling magnetoresistance effect. (b) SEM image of a typical sample in false colors. The red arrows indicate the direction of the magnetizations. A back gate electrode (not visible) is used to tune the energy levels of the device. As shown by the orange arrow, the external B-field is applied along one of the easy axis of the two PdNi strips.*

The device proposed is a SWCNT quantum dot-based, connected to two non-collinear leads like the one presented schematically in fig. 5.1, (a). The system acts like a spin-valve with ferromagnetic electrodes controlled via a finite tunneling magnetoresistance effect. The versatility of carbon nanotubes to fabricate quantum dots when connected to PdNi magnetic electrodes, via tunneling barriers was already introduced in chapter 2, so one can expect here to study non-collinear magnetoresistance related phenomena by designing the magnetic electrodes to form of an angle $\theta = \pi/2$.

Single wall carbon nanotubes were grown by CVD methane-based process on a highly doped Si substrate used as a back gate. Taking into account the study on PdNi magnetic properties, presented in Chapter 4, the samples are connected to ferromagnetic electrodes, $Pd_{30}Ni_{70}$, 30 nm thick and 200-300 nm wide, covered with 5 nm of Pd; the contacts forme an angle $\theta = \pi/2$. The angle between the magnetizations of the electrodes is checked on control samples at room temperature using MFM imaging (see fig. 5.2). White/Brown contrast indicate the orientation of the magnetization inside the leads. It is visible that the magnetization has a transversal orientation with respect to the longitudinal axis of the stripes (see Chapter 4). Thus it is expected for the two magnetizations of align either in parallel/antiparallel geometry or to become perpendicular to one another.

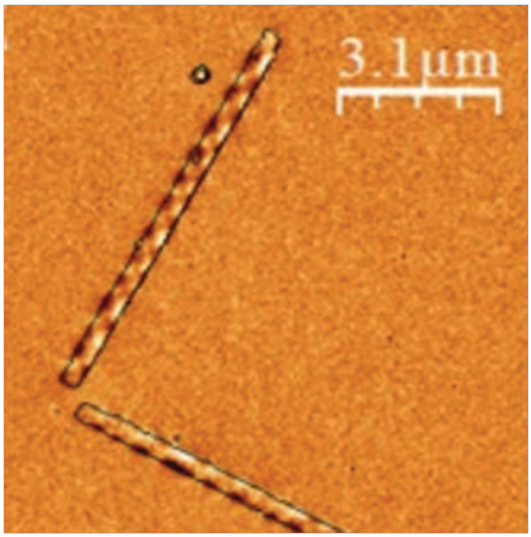

Figure 5.2: *MFM image performed on a $Pd_{30}Ni_{70}$control sample at room temperature. The angle between the two PdNi leads is $\theta = \pi/2$. White / brown contrasts indicate the magnetic charges inside the leads. Their arrangement is consistent with a magnetization mainly perpendicular to the longitudinal axis of the stripes.*

The conductance measurements were performed using standard lock-in detection technique with an AC modulation of 100 μV at 777.77 Hz. Each magnetoresistance plot is obtained by averaging 4 times single curves, all displaying the hysteresis switching. In fig. 5.1, (b), it can be seen a SEM image of a typical sample in false colors. The external magnetic field is applied along the direction of one of the electrodes and thus perpendicular to the second one. The choice of the angle between the electrodes is due to ensure the maximum effect differences when the external field is swept between positive and negative values.

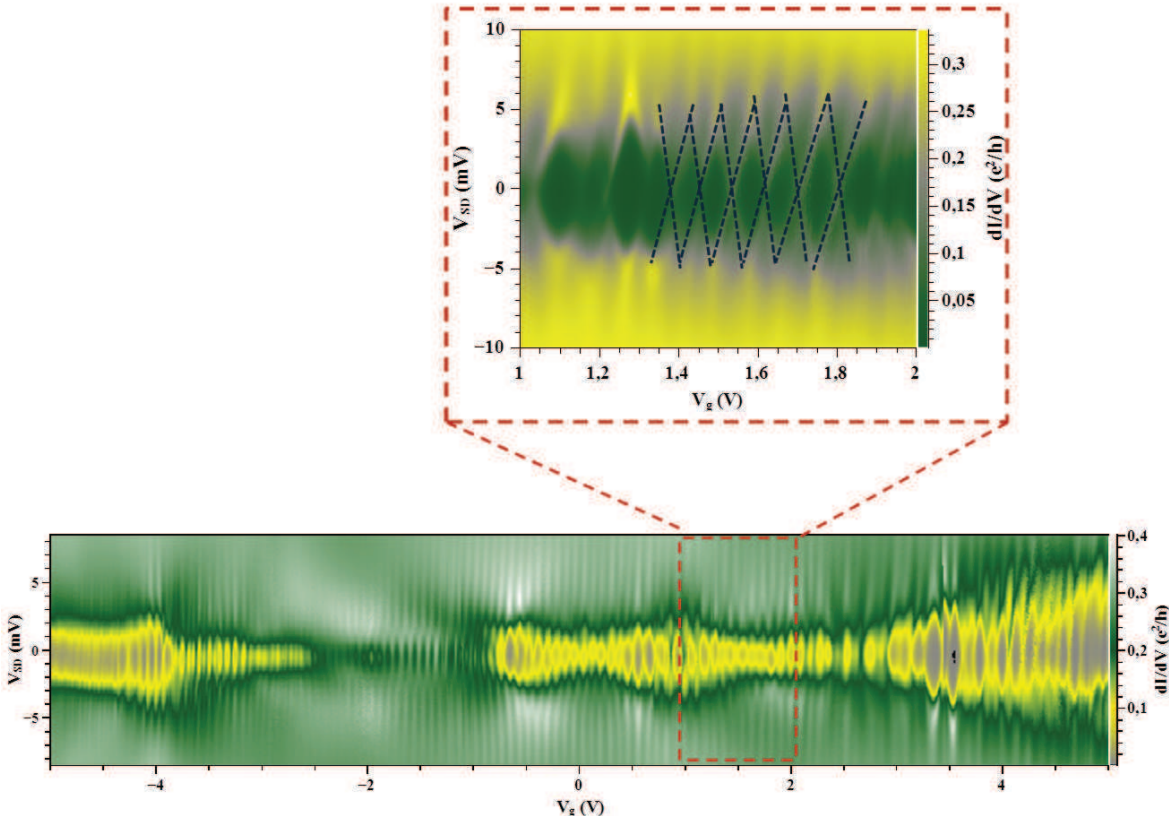

Figure 5.3: *Color scale differential conductance spectroscopy of the device as a function of over a wide range source-drain bias V_{SD} and the gate voltage V_g. Characteristic Coulomb diamonds are displayed. Experimental temperature is* 1.8 K.

Electron transport properties are revealed using bias spectroscopy, where the differential conductance is measured as a function of gate and bias voltages in a color plot. Fig. 5.3 displays such a color scale differential conductance map of the device as a function of the source-drain bias V_{SD} and the gate voltage V_g over a wide range of voltages. The color scale plot shows in the far negative gate voltages signs of Fabry-Perot oscillations, with Coulomb blockade effect around zero bias.

Towards more positive region of gate voltages depicts the case of a metal/CNTs' weak contact. Specific Coulomb diamonds characteristic to the spectroscopy of a quantum dot can be observed. By looking at the average mean height of a diamond, one can read off the charging energy of the system which in this case is about 3 meV. The mean level spacing variate with the gate region: from smaller in the gate region displayed (< 1 meV), to substantially larger (about 3 meV) for more positive values of the gate. The latter value is consistent with the lithographically defined length of the quantum dot which was about 500 nm to 600 nm. All measurements were performed at a temperature of 1.8 K.

5.1.1 Spin transport in the linear regime

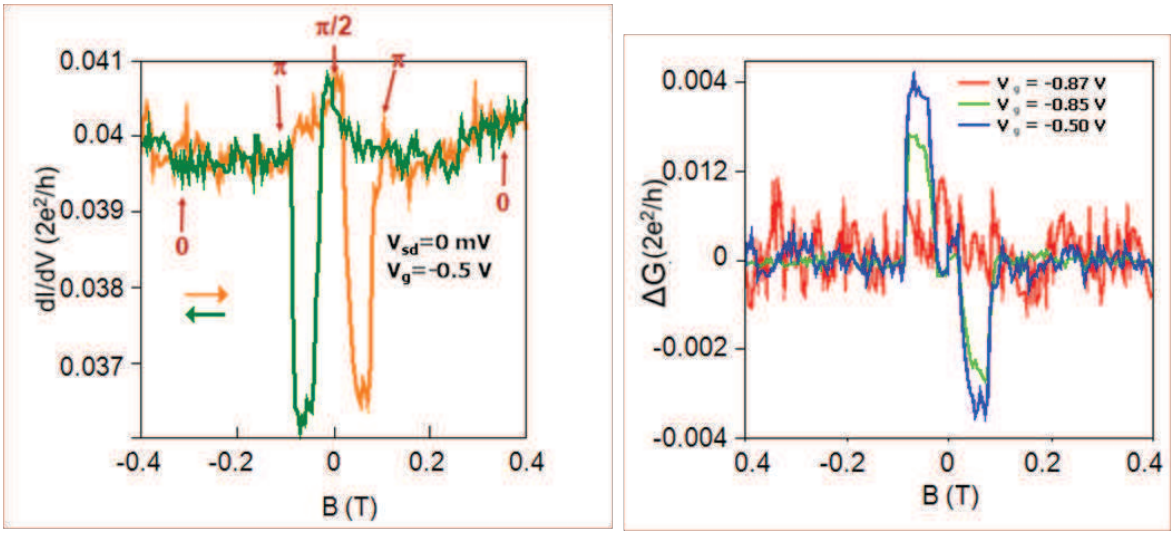

Figure 5.4: *Gate response of magneto-resistance (a) Single magnetoresistance curve for $V_{sd} = 0\ mV$ and $V_g = -0.5\ V$. The orange curve corresponds to increasing magnetic field (G_{trace}). The green curve corresponds to decreasing magnetic fields ($G_{retrace}$). (b) Variations of the jumps magnitude ($\Delta G = G_{trace} - G_{retrace}$) were observed for different values of V_g .*

A first set of data obtained by measuring this device concerns the characterization of the spin transport in the linear regime. That is in the absence of a source-drain voltage. An external magnetic field is sweeped between $\pm 0.4\ T$ while applying also a gate voltage. One can observe a typical magnetoresistance signal, fig. 5.4, (a) typical to a spin-valve behavior where the hysteretic switchings are situated at about 10 mT and 80 mT when the magnetic field is increasing and at $-10\ mT$ and $-80\ mT$ for a decreasing magnetic field. This switches correspond to the modifications in the magnetizations of the ferromagnetic leads: at zero magnetic field the angle between the two electrodes is $\theta = \pi/2$, as already seen in the MFM image taken at room temperature.

The first switch can be translated as the return of the magnetization in one of the leads leading to the relative degree between the two magnetization of $\theta = \pi$. The second switching event is attributed to a switch from $\theta = \pi$ to $\theta = 0$. If the amplitude of the hysteresis, ΔG, is seen as the difference in conductance upon increasing the external magnetic field, G_{trace}, and decreasing the external magnetic field, $G_{retrace}$, one can observe in fig. 5.4, (b), that at different gate voltages ($V_g = -0.87\ V$, $V_g = -0.85\ V$ and $V_g = -0.5\ V$) appear variations in the jumps magnitude.

A representation of the amplitude of the hysteresis, ΔG, on a larger interval of V_g, represented in colorscale plot as a function of the external magnetic field B and V_g

in fig. 5.5, (a) show variations between 4 % and annihilation. The clear vertical red (positive) and blue (negative) stripes show how the hysteresis is modulated as the gate voltage is swept. Such behavior accounts for a controlled character of the phenomena, specific to magnetic tunnel junction-type of device. The results are similar to the one observed in the collinear regime by Sahoo et al [35]. The oscillations of the hysteresis are best shown by defining the TMR as : $(G_{trace} - G_{retrace})/G_{trace}$ at $B = 75\ mT$.

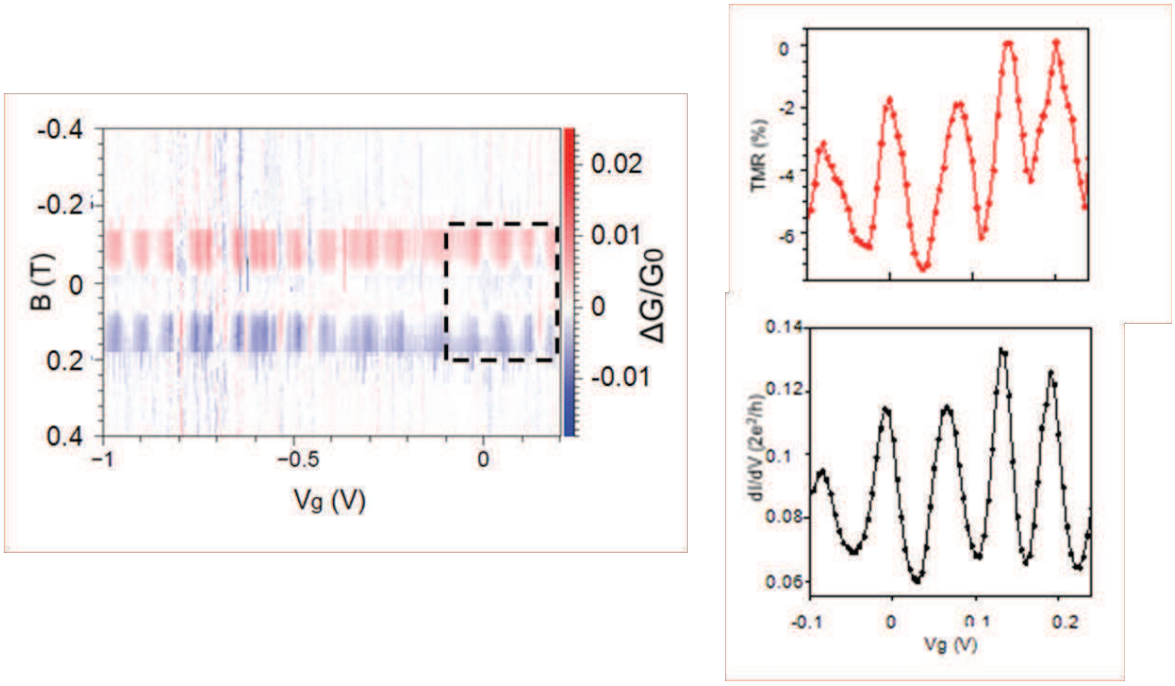

Figure 5.5: *(a) Wide source- voltage response of the spin signal* $\Delta G = G_{trace} - G_{retrace}$ *in color scale as a function of the B-field and the gate voltage* V_g*. (b) Top panel : Linear conductance modulations at zero magnetic field as a function of the back gate voltage for the region inside the square in dashed lines of panel (a). Bottom panel: TMR modulations measured simultaneously with the linear conductance.*

The TMR is represented in fig. 5.5, (b) bottom panel below the linear conductance at zero field. Both quantities oscillate as a function of the gate voltage due to the quantum behavior of the nanotube connected to ferromagnetic electrodes. The oscillations of the TMR originate in quantum interferences phenomena as well as interactions taking place inside the device. The oscillations of the TMR are slightly shifted in phase (by about $\pi/4$) with respect of the modulations in conductance, with the same period. This accounts for spin injection phenomena in a coherent conductor with quantized energy levels, as Cottet et al have shown [46]. Additionally, it allows one to discard other mechanisms that could account for the hysteretic signal, like the magneto-Coulomb effect, which imply that the modulations of the TMR are proportional to the derivative of the conductance. Finally, it's worth noticing that the TMR has a constant negative sign on all the interval.

5.1.2 Out of equilibrium spin-signal

The non-linear transport regime ($V_{SD} \neq 0$ was also investigated. In fig. 5.6 it is displayed a hysteretic signal taken as a function of both the external field and the source-drain bias V_{SD} for a gate voltage of $V_g = 0.312\ V$. The difference with respect to the linear regime consists in the sign change of the the hysteresis signal as the source-drain voltage is swept between positive and negative values, from positive at $V_{SD} = 1.25\ mV$ to negative for $V_{SD} = -2.75\ mV$.

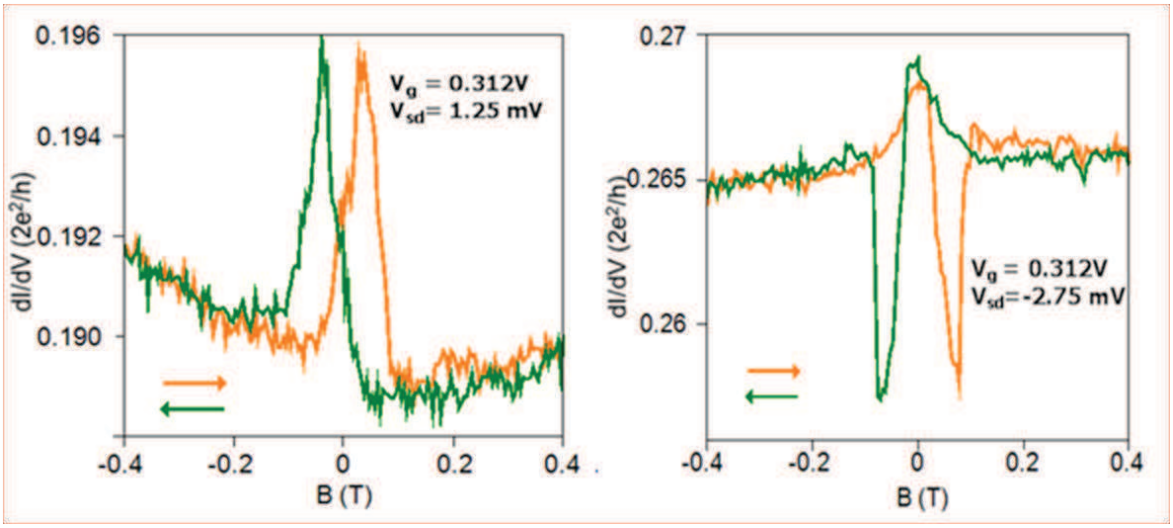

Figure 5.6: *Single magnetoresistance curves for $V_{SD} = -2.75\ mV$ and $V_{SD} = 1.25\ mV$. The back gate voltage is $V_g = 0.312\ V$. The orange curve corresponds to increasing magnetic field (G_{trace}). The green curve corresponds to decreasing magnetic fields ($G_{retrace}$)*

The representation of the spin signal, ΔG, on a larger interval of V_{SD}, is represented in colorscale plot as a function of the external field and V_{SD} for the same gate in fig. 5.7, (a). The clear vertical red (positive) and blue (negative) stripes show the evolution of the hysteretic signal with the source-drain voltage. As a convention, the blue stripe corresponds to positive B fields and negative bias while the red stripe is used for positive bias and it depicts a spin signal with the same symmetry as the current. This behavior proves itself consistent in fig. 5.7, (b), where the TMR versus source-drain V_{SD} displays a nearly anti-symmetric behavior, up to a constant background which is attributed to a classical-single barrier like-TMR signal.

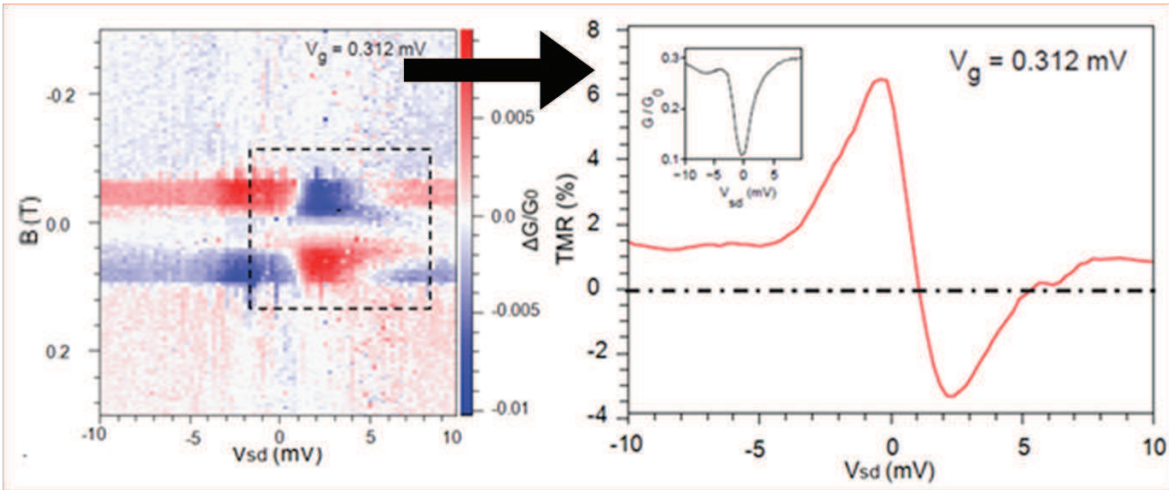

Figure 5.7: *Left: color scale plot of the spin signal ΔG as a function of the external magnetic field, B, and the source-drain voltage, V_{SD}, for $V_g = 0.312\ mV$; right panel: TMR signal as a function of the source-drain voltage, V_{SD}, for $V_g = 0.312\ mV$; the inset shows the differential conductance, G, versus source-drain bias, V_{SD} for the same gate voltage as before.*

Fig. 5.8 accounts for the non triviality of the behavior: one can see the same anti-symmetric evolution of the TMR for five different gate voltages. Some of the features displayed in the image do not have yet an explanation. This behavior is qualitatively different from that of the linear regime and can only be explained if interactions are taken into account inside the system, as suggested by Cottet et al [47].

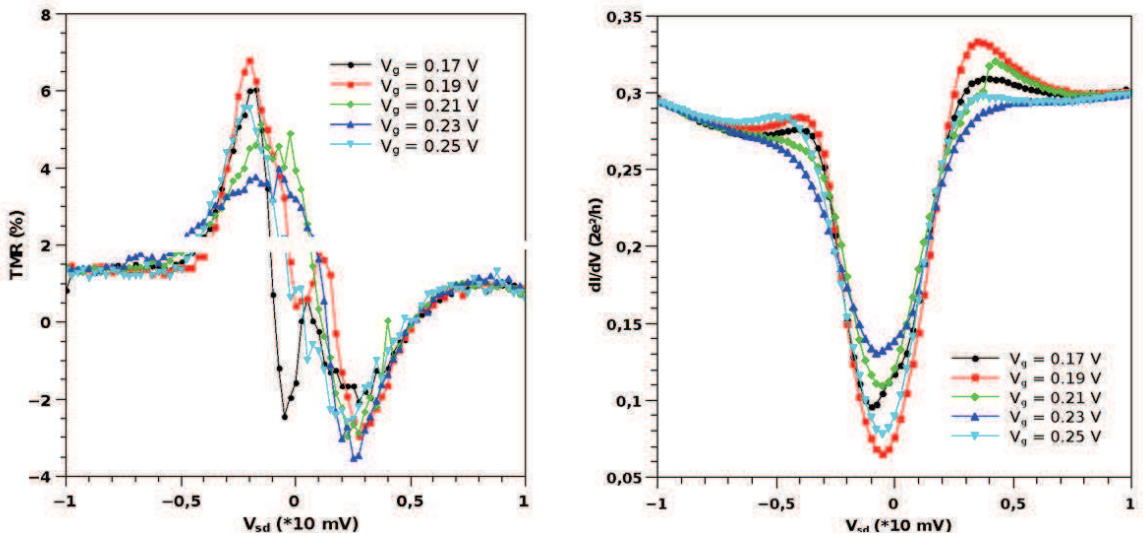

Figure 5.8: *Left panel: TMR signal as a function of the source-drain bias V_{SD} for different gate voltagesright panel: the differential conductance, G, versus source-drain bias, V_{SD} for the same gate voltages as in the left panel.*

This anti-symmetric behavior (which has the same symmetry as the current) is suggestive of current induced spin precession. It can be understood using a simple semiclassical Bloch-Redfield type equation for the spin on the dot which allow one to calculate the dot's spin projection $S_{L(R)}$ on the magnetization of each ferromagnetic contact. We get :

$$S_{L(R)} = \frac{h}{2e} p(1 - \cos\phi) I \tau_s \times \frac{1}{1 + (\omega_L \tau_s)^2 (\sin\phi)^2} \tag{5.1}$$

Here, I is the electrical current flowing through the device, p is the spin polarization of the ferromagnetic electrodes, ϕ is the angle between the magnetizations of the electrodes, $\omega_L = g\mu_B B/h$ is the Larmor frequency corresponding to precession of the dot's spin around the external magnetic field and τ_s is the spin relaxation time of the dot's spin.

Equation (5.1) has two parts: the first one testifies on the competition between spin accumulation and spin relaxation phenomena while the second one (which has a Lorentzian shape as a function of the external magnetic field) is a Hanle type term which describes spin precession [48]. One can evaluate $S_{L(R)}$ through the hysteretic part of the conductance and/or the TMR.

In the device characterised here, the coupling to the leads are very asymmetric, thus TMR, $\Delta G \propto p_{L(R)} S_{R(L)}$. Because of this, one can use equation (5.1) to compare

it with the experimental data to see is it can be estimated the evolution of τ_s with the bias applied to the device. One can consider:

$$\tau_s \approx \tau_0/(1+(V_{SD}/V_0)^2)^2 \tag{5.2}$$

and using a constant classical background of 1.2%, can get the solid red curve fitting quantitatively the TMR data versus bias V_{sd} for $V_g = 0.21\ V$ represented in fig. 5.9. The parameters used in this calculus are $\tau_0 \approx 3\ ns$ and $V_0 = 2.2\ mV$. Such an evolution can be seen as a spin accumulation phenomena which tends to force the spin inside the dot to yeald the current (that is to have the same antisymmetric evolution in bias) whereas spin relaxation acts against it, altering the spin signal data ΔG in the bias-field plane [49].

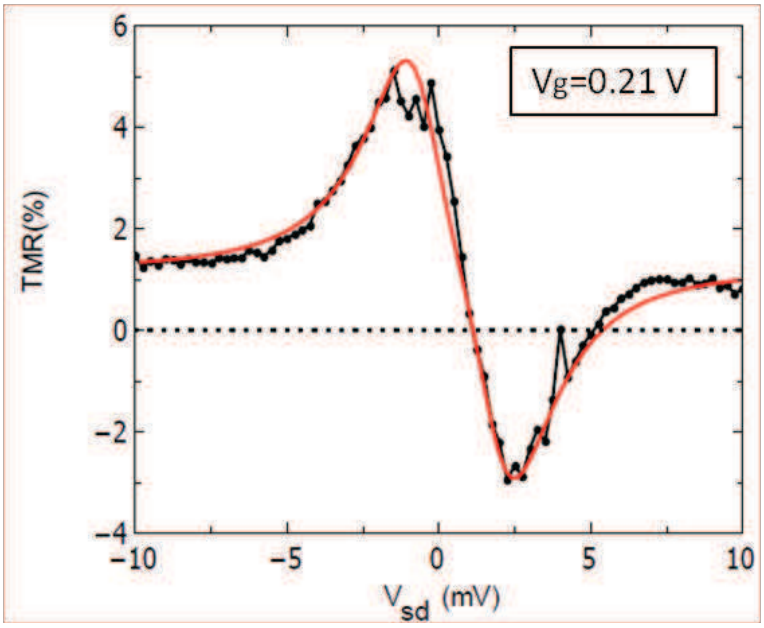

Figure 5.9: *black line - Linear conductance measured simultaneously with the spin signal and taken from a horizontal cut of the color scale plot from fig; red line- theoretical simulations in accord with the experimental data.*

To show that current induced spin precession is a valid explanation for the results presented here, the low bias behavior of the spin signal must be investigated. In fig. 5.10, it is shown a zoom in the colorscale plot between $-5\ mV$ and $5\ mV$ for two different gate voltages, $V_g = 0.25\ V$ and $V_g = 0.23\ V$. Green dashed lines are used to emphasize the gate dependence of the dispersion at zero TMR point in the $B - V_{SD}$ plane. The slope of the white line that is the vanishing point of the TMR comes from the second (precession) part of equation 5.1. The bias increases as the spin relaxation time decreases leading to a larger width of the Lorentzian curve of the second part. This slope gives thus direct access to the spin relaxation time inside the device.

Of course, the spin relaxation time is different whether the dot's level is at resonance or off resonance due simply to a density of states argument. A study of this effects' evolution with gate dependence, should help clearing the phenomenological picture. For this, it is useful to define an effective g-factor, $g_{eff} = eV_{SD}/\mu_B B$.

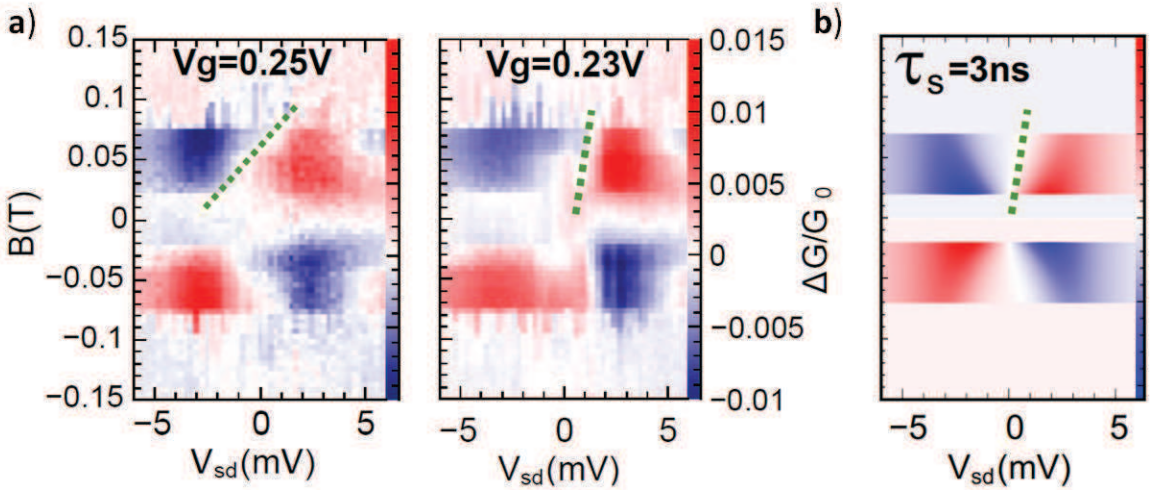

Figure 5.10: *(a) Zoom on the color scale plot of the spin signal as a function the external magnetic field, B, and the source-drain bias, V_{sd}, for $V_g = 0.25\ V$ and $V_g = 0.23\ V$. The tilted white line highlighted by the green dashed line corresponds to the points where the spin signal changes sign; (b) Simulated color scale plot of the spin signal as a function the external magnetic field, B, and the source-drain bias, V_{sd}, for $V_g = 0.23\ V$ using equation (5.1), $\tau_s = 3\ ns$ and $V_0 = 2.2\ mV$.*

Obtained values for the effective g-factor range from 200 to 700, which means that the small field of about 100 mT, used to switch one of the ferromagnetic electrodes and rotate the other one, has an effect on the spins on the quantum dot which would be equivalent to about 20 T and 70 T. These high values can only be explained if spin precession is taking place inside the QD (a schematic view of the process is displayed in fig. 5.10, (a)).

This slope is very well reproduced by equation 5.1, as one can easily see in fig. 5.10, (b). A simulated color scale plot of the spin signal, S_L, as a function the external magnetic field, B, and the source-drain bias, V_{sd}, for $V_g = 0.23\ V$, show good agreement with the magnetoresistance measurement. The switchings of the magnetizations are accounted for using simple Heaviside functions.

For the simulations, the spin accumulation on the dot is described using:

$$\frac{h}{2e} pI(\overrightarrow{n}_L - \overrightarrow{n}_R) \tag{5.3}$$

where p is the spin polarization of the ferromagnetic electrodes. We consider the two polarizations corresponding to the two leads as being equal. I is the electrical current and $\overrightarrow{n}_{L(R)}$ are the unit vectors collinear, respectively, to the left electrode's magnetization, (L), and the right's electrode magnetization, (R).

If the spin inside the QD, $\overrightarrow{S}$, is considered placed into a magnetic field, that can be real or effective, then one can write:

$$\overrightarrow{B} = B_L \overrightarrow{n}_L + B_R \overrightarrow{n}_R \tag{5.4}$$

For an external field that is coplanar to the magnetizations of the two leads, which is the case in the experiments runned here, the Bloch-Redfield type equations describing the dynamics of QD's spin, $\overrightarrow{S}$, can be written as:

$$\frac{d\overrightarrow{S}}{dt} = \frac{h}{2e} pI(\overrightarrow{n}_L - \overrightarrow{n}_R) + \overrightarrow{S} \times \overrightarrow{B} - \frac{\overrightarrow{S}}{\tau_s} \tag{5.5}$$

The following notations are used: $\overrightarrow{S} = S_L \overrightarrow{n}_L + S_R \overrightarrow{n}_R + S_\perp \overrightarrow{n}_L \times \overrightarrow{n}_R$ and $\cos\phi = \overrightarrow{n}_L . \overrightarrow{n}_R$. thus one gets, in the stationary regime:

$$\begin{aligned} -\frac{h}{2e} pI(1-\cos\phi) + S_\perp B_L \sin^2\phi - \frac{S_R}{\tau_s} &= 0 \\ \frac{h}{2e} pI(1-\cos\phi) - S_\perp B_R \sin^2\phi - \frac{S_L}{\tau_s} &= 0 \\ S_L B_R - S_R B_L &= \frac{S_\perp}{\tau_s} \end{aligned} \tag{5.6}$$

Finally, the spin signal, S_L, can be written using:

$$S_{L(R)} = \frac{h}{2e} p(1-\cos\phi) I\tau_s \times \frac{1 \pm B_{L(R)}(B_L - B_R)\sin^2\phi}{1 + (B_L^2 + B_R^2)\tau_s^2 \sin^2\phi} \tag{5.7}$$

This formula yields equation (5.1) if $B_L = 0$ and $B_R = B$.

Other possible explanations for the phenomenology observed during this work, like Zeeman or orbital effects would be much too weak to explain these features. The gate modulations of g_{eff} as well as the conductance modulations are shown in fig. 5.11, (b). As one could expect intuitively, the spin precession effect (see schematics in fig. 5.11, (a)) is maximum when the dot is off resonance when the dwell time of the electron is also maximum.

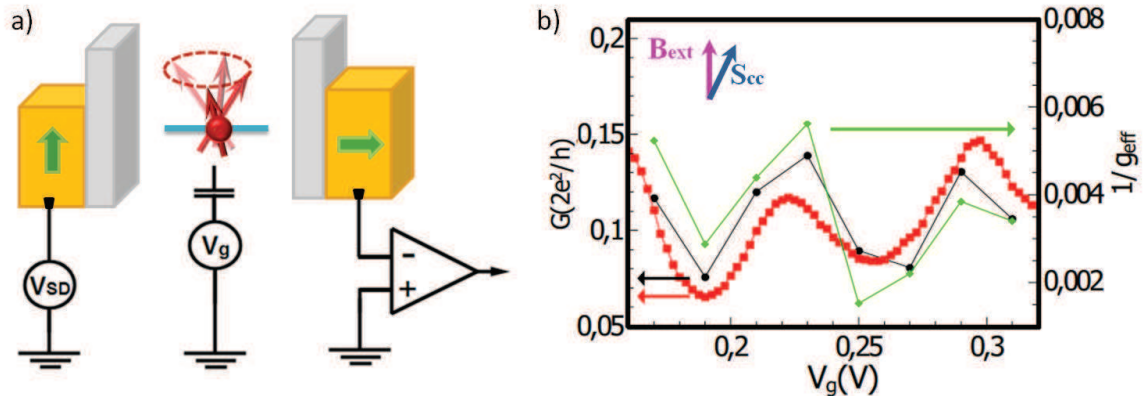

Figure 5.11: *(a) Schematic picture of the precession place inside the CNT due to the competition between spin accumulation represented by the purple vector and spin precession represented by the blue vector; (b) Green diamonds : Effective inverse g-factor* $1/g_{eff}$ *(right axis) as a function of gate voltage. Black circles and red squares : linear conductance measured simultaneously with the spin signal in triangles and taken from a horizontal cut of a color scale plot. The latter has been shifted by* $-0.02\ V$ *to compensate the small gate shift which occurred between the two measurements.*

5.1.3 Conclusion

A carbon nanotubes based device with with ferromagnetic PdNi electrodes was proposed to investigate transport in a quantum non-collinear magnetoelectronic system. Owing to the transverse anisotropy of the leads and transparent enough contacts between the CNT and the ferromagnets, one can actually study quantum dots with non-collinear leads by defining magnetic electrodes forming an angle of $\pi/2$. A full transport study of one device, stable enough to go through all possible spin transport measurements at finite bias voltage was performed.

The device acts like a spin-valve with a finite tunneling magnetoresistance effect. Measurements in linear spin dependent transport display the usual signatures of electronic confinement already seen in collinear geometry devices. In addition, the finite bias magnetoresistance displays an anti-symmetric reversal in contrast with the linear regime.

This effect, can be understood only if electronic interactions are considered. In fact, both experiments and simulations indicate an interplay between spin accumulation phenomena which tends to force the spin inside the dot to follow the symmetry of the current and spin relaxation that acts against it, determining a precession of the spin inside the QD and thus altering the spin signal in the bias-field plane.

5.2 Fabry-Perot transport regime

Highly transparent contacts between the CNT and the ferromagnetic leads allow the manifestation of Fabry-Perot's physics. This usually happens at negative values of the gate voltage when the tunneling barrier become more transparent. This transport regime can be described by using an analogy to the Fabry-Perot interferometer: by using the gate voltage or the source-drain voltage one can modulate the relative position of the Fermi levels in the ferromagnetic leads with respect to the energy levels inside the QD (which are broaden than in the case of the Coulomb blockade). This counts for the modulation of the injected carriers' wavevector. Phase is accumulated while the carriers pass through the nanotube and when the phase suffers a shift of 2π, the conductance undergoes an oscillation.

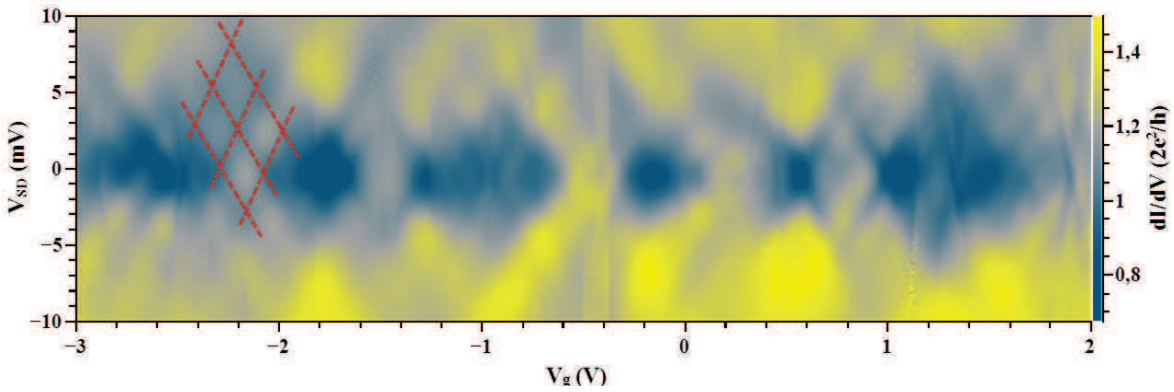

Figure 5.12: *Color scale differential conductance spectroscopy of the device over a wide range of source-drain bias, V_{SD}, and gate voltage, V_g. Characteristic chessboard patters, specific to Fabry-Perot physics, can be seen. Experimental temperature is* 1.8 K. *The energy spacing is of* 5 mV, *consistent with the lithographically defined length of the CNT which is about* 600 nm.

When plotting a greyscale of the conductance, taken at 1.8 K, as a function of the gate voltage and source-drain voltage one gets a chessboard like pattern, see fig. 5.12. The rhombic structure easily identifiable gives access to the energy spacing inside the QD. In fact, the distance between the centers of adjacent rhombs depends on the length of the nanotube, L: $\Delta E = hv_F/L$. FOr the sample characterised in this work, the energy spacing is of 5 mV, consistent with the lithographically defined length of the CNT of about 600 nm. In this regime, the nanotube acts as a coherent waveguide and the resonant cavity is formed between the two CNT-electrode interfaces.

5.2.1 Spin transport in the linear regime

Measurements in the linear regime concern the characterization of the spin transport in the absence of source-drain voltage. An external field is sweped between $\pm 0.4\ T$ along one of the electrodes of the device and perpendicular to the other one while applying also a gate voltage. As in the case of the device exhibiting Coulomb blockade transport regime, the amplitude of the hysteresis is defined as the difference in conductance upon increasing the external magnetic field, G_{trace}, and decreasing the external magnetic field, $G_{retrace}$. When plotted as a function of the external magnetic field B and V_g, see fig. 5.13, the vertical red (positive) and blue (negative) stripes show a hysteretic signal, modulated along the gate voltage.

One can see the hysteretic switchings take place in two stages, equivalent for both the positive/negative regions of the amplitude: one between 20 mT and 60 mT and a second one between 60 mT and 110 mT. This switches correspond to modifications in the magnetizations of the ferromagnetic leads. Measurements done on a larger interval of V_g show variations in the jumps magnitude up to 4 % with noisier signal detected in the positive area of V_g. Such behavior is typical for a magnetic junction-type of device.

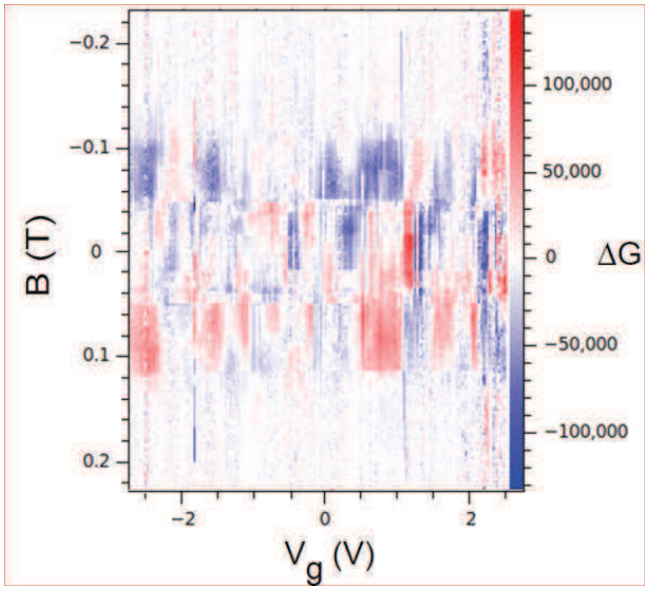

Figure 5.13: *Wide gate voltage response of the spin signal* $\Delta G = G_{trace} - G_{retrace}$ *in color scale as a function of the external magnetic field,* B*, and gate voltage* V_g*.*

5.2.2 Spin transport in non-linear regime

These promissing results, encouraged further investigations regarding the out of equilibrium transport regime. In fig. 5.14, (a), it is displayed the amplitude of the hysteresis as the difference in conductance signal as a function of the source-drain bias V_{SD} when

the device is placed in an external magnetic field. Things look somehow different from those in the linear regime: for once there is no sign change in the TMR signal, but in the same time, one can see a clear and consistent modification of the field value where the switch takes place. For V_{SD} between $-3\ mV$ and $1.4\ mV$ the switches in the magnetization take place at $\pm 0.1\ T$ while the second switch is more variable with V_{SD}. For source-drain values bigger than $1.4\ mV$ the switches take place at $-0.1\ T$ and $0.2\ T$ and correspondingly in the positive area of V_{SD}.

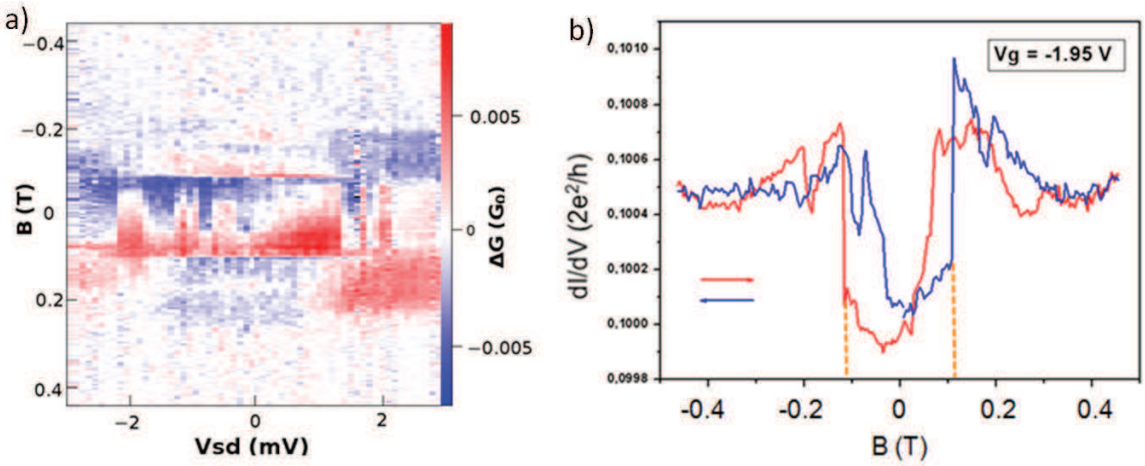

Figure 5.14: *(a) Wide gate voltage response of the spin signal* $\Delta G = G_{trace} - G_{retrace}$ *in color scale as a function of the B-field and* V_{SD}*. (b) Single magnetoresistance curves for* $V_g = -1.95mV$*. Magnetization reversal before the external field changes sign.*

Fig. 5.14, (*b*), shows a very interesting hysteresis curve taken for $V_g = -1.95\ V$. Its particularity lies in the fact that the switch of the first electrode takes place before the external magnetic field applies changes sign, both when the field increases and decreases (for $B = -0.11\ T$ and $B = 0.6\ T$ when the field increases, respectively $B = 0.11\ T$ and $B = -0.4\ T$ when it decreases). While surprising, the phenomena was registered for various V_{SD} values show the non triviality of this behavior.

While more investigations needs to be pursued to establish with certainty the nature of such result, one could think of considering an equilibrium torque that helps the external applied field to switch the magnetization of the two leads.

5.2.3 Conclusion

Highly transparent contacts between the CNT and the ferromagnetic leads allow the manifestation and the investigation of Fabry-Perot's physics. This usually happens at

negative values of the gate voltage when the tunneling barrier become more transmitting. Our measurements indicate a energy spacing is of 5 mV inside the nanotube, consistent with the lithographically defined length which is about 600 nm. In this regime the nanotube acts as a coherent waveguide and the resonant cavity is formed between the two CNT-electrode interfaces.

Linear transport measurements indicate that hysteretic switchings take place in two stages both when the external magnetic field increases and when it decreases. The phenomenon is consistent on a large interval of gate voltage and is modulated by it.

Out-of equilibrium transport measurements showed an intriguing result. We recorded hysteretic loops where magnetization reversal in the electrodes takes place before the external magnetic field applied changes sign, both when the field increases and decreases. The phenomena was registered for various V_{SD} values.

To establish with certainty the nature of such result more investigations need to be performed but these preliminary results seem to suggest an equilibrium torque that helps the switch of the magnetization in the leads.

Chapter 6

Conclusions

During this work we have first investigated PdNi alloy, using EHE measurements to put in evidence the out-of-plane component of the magnetization. Our efforts concentrated on $Pd_{20}Ni_{80}$ and $Pd_{90}Ni_{10}$. In the case of $Pd_{20}Ni_{80}$, this study is a first of the kind and results show that, even at low temperatures ($T = 10\ K$), the magnetization remains in plane. The result is very helpful for the second part of this work, the one concentrated on quantum spin valve effect since an in plane magnetization translates into a small stray magnetic field exerted by the two ferromagnetic leads.

We investigated how different parameters influence the magnetic behavior of the nanostripe-shaped PdNi. The measurements show that geometry, thickness and chemical composition together with capping layer used to protect the PdNi against oxidation, are all important parameters when choosing the right characteristics for a spin-based device. Measurements done on nanometric sized Hall crosses show an out-of-plane component of the magnetization at small temperatures (below 40 K), but less than in the case of the micrometric size samples. This is due to due to the stress relaxation at the edges which has an enhanced importance for small dimensions devices.

Extraordinary Hall measurements confirm in all aspects that the magnetic preferential direction of high aspect ratio PdNi contact strips feature a magnetically easy axis transverse to the strip orientation. This is a further experimental proof for the model proposed by Chauleau et al [3] sustaining a magnetic easy axis, transversal to the strip orientation due to shape anisotropy. A perpendicular component magnetization effect was recorded, but according to Chauleau et al the edges remain transverse while the core of the stripe will turn out-of-plane.

According to all these results, in our CNT based spin devices, it is therefore recommended to use a Ni-rich alloy for the electrodes connecting the CNT, due to the in-plane orientation of the magnetization that will produce a smaller stray field. Also, best is to apply external magnetic fields in transverse direction to the magnetization of the electrodes in order to obtain a distinct switching behavior.

In the second part of this work, we combined the versatility of carbon nanotubes grown by CVD methane-based process on a highly doped Si substrate to quantum dots when connected to ferromagnetic electrodes. We used $Pd_{30}Ni_{70}$, 45 nm thick covered with 5 nm Pd to contact the CNT, via tunneling barriers so that one can study QD physics with non-collinear leads. The magnetic electrodes are lithographically designed to form an angle of $\theta = \pi/2$. The QD is capacitively connected to a gate voltage while the electrodes'chemical potential is controlled via a source-drain voltage.

Depending on the transparency of the contacts between the nanotube and the ferromagnetic leads, we were able to record two different transport regimes: Coulomb blockade and the Fabry-Perot regime, both confirmed by their specific patterns by their specific patterns on conductance maps.

Characterization of the spin transport in Coulomb blockade, linear regime, showed that when an external field applied along the magnetization of one of the leads give a typical TMR signal, accounting for a spin-valve behavior of the device. The hysteretic switchings are symmetric with respect to the 0 external field and corresponding to the modifications in the relative magnetization of the electrodes. Measurements on a large interval of gate voltages show gate controlled variations in the jump magnitude, up to 4 %.

The TMR signal oscillates with the gate voltage due to the quantum behavior of the nanotube connected to leads. The oscillations of the TMR originate in quantum interferences phenomena as well as interactions taking place inside the device. The oscillations of the TMR are slightly shifted in phase (by about $\pi/4$) with respect of the modulations in conductance, with the same period, marker of spin injection phenomena in a coherent conductor with quantized energy levels.

Overall, the device acts like a spin-valve with a finite tunneling magnetoresistance effect. Linear spin dependent transport highlights the usual signatures of electronic confinement already seen in collinear geometry devices while the finite bias magnetoresistance displays an anti-symmetric reversal in contrast with the linear regime. This effect, can be understood only if electronic interactions are considered. In fact, both experiments and simulations indicate a concurential behavior between spin accumulation phenomena which tends to force the spin inside the dot to follow to the current and spin relaxation that acts against it, determining a precession of the spin inside the QD and thus altering the spin signal in the bias-field plane.

Highly transparent contacts between the CNT and the ferromagnetic leads allow the manifestation of Fabry-Perot's physics, this usually happens at negative values of the gate voltage when the tunneling barrier become more transmitting. Our measurements indicate a energy spacing is of 5 mV inside the nanotube, consistent with the

its lithographically defined length which is about 600 nm. In this regime the nanotube acts as a coherent waveguide and the resonant cavity is formed between the two CNT-electrode interfaces.

Magnetization switchings of the leads take place in two stages, equivalent for both the positive/negative regions of the amplitude: one between 20 mT and 60 mT and a second one between 60 mT and 110 mT.

The non-equilibrium regime, gave a mostly interesting result of this thesis. We recorded hysteretic loops in which the magnetization reversal in the electrodes takes place before the external magnetic field applies changes sign, both when the field increases or decreases. The phenomena was registered for various V_{SD} values proving the non triviality of this behavior.

While more investigations needs to be pursued to establish with certainty the nature of such result, one could think of considering an equilibrium torque that helps the external applied field to switch the magnetization of the two ferromagnetic leads.

Bibliography

[1] S. Iijima. *Helical microtubules of graphitic carbon*. Nature, 354, pages 56 - 58 (1991).

[2] Y. Matsuda, W.-Q. Deng, III W. A. Goddard *Contacts resistance for "end-contacted" metal-graphene and metal-nanotube interfaces from quantum mechanics*. J. Phys Chem, 114 (2010)

[3] J.-Y. Chauleau, B.J. McMorran, R. Belkhou, N. Bergeard, T.O. Mentes, M. A. Nino, A. Locatelli, J. Unguris, S. Rohart, J. Miltat, A. Thiaville. *On the magnetization textures in NiPd nanostructures*. Phys. Rev. B, B 84, 094416 (2011).

[4] C. Feuillet-Palma, T. Delattre, P. Morfin, J.-M. Berroir, G. Feve, D. C. Glattli, B. Placais, A. Cottet, and T. Kontos. *Conserved spin and orbital phase along carbon nanotubes connected with multiple ferromagnetic contacts*. Phys. Rev. B, B 81, 115414 (2010).

[5] A. Fert, F. Nguyen, Van Dau F. Petroff, P. Etienne, G. Creuzet, A. Friederich, M. N. Baibich, J. M. Broto and J. Chazelas. *Giant magnetorezistance of* $(001)Fe/(001)Cr$ *magnetic superlattices*. Phys. Rev. Lett., 61:2472 - 2475 (1988).

[6] F. Saurenbach, G. Binasch, P. Grunberg and W. Zinn. *Enhaced magnetoresistance in layered magnetic structures with antiferromagnetic interlayer exchange*. Phys. Rev. B, 39:4828-4830 (1989).

[7] A. Brataas, G. E. W. Bauer, P. J. Kelly. *Non-collinear Magnetoelectronics*. (2007).

[8] M. Johnson and R. H. Silsbee. *Interfacial charge-spin coupling: injection and detection of spin magnetization in metals*. Phys. Rev. Lett., 25:1270 (1970).

[9] J.C. Slonczewski, J. Magn. Magn. Mater. *Interfacial charge-spin coupling: injection and detection of spin magnetization in metals*. 159, L1 (1996).

[10] L. Berger. *Emission of spin waves by a magnetic multilayer traversed by a current*. Phys. Rev.B, 54, 9353-9358 (1996).

[11] E. B. Myers, D. C. Ralph, J. A. Katine, R. N. Louie, R. A. Buhrman. *Current Induced Switching of Domains in Magnetic Multilayer Devices*. Science, 285, 5429, pages 867-870, 5429.867 (1999).

[12] S. Datta, B. Das. *Emission of spin waves by a magnetic multilayer traversed by a current*. App. Phys. Lett., 56:665 (1990).

[13] E. A. de Andrada e Silva, G.C. La Rocca, F. Bassani. Phys. Rev. B, 55, 16293 (1997).

[14] E. Rashba. Sov. Phys. Solid State, 2, 1109 (1960).

[15] D. Grundler. *Large Rashba Splitting in InAs Quantum Wells due to Electron Wave Function Penetration into the Barrier Layers*. Phys. Rev. Lett., 84, 6074-6077 (2000).

[16] J. Nitta, T. Akazaki, I. Takayanagi, E. Takatomo. *Gate Control of Spin-Orbit Interaction in an Inverted* $In_{0.53}Ga_{0.47}As/In_{0.52}Al_{0.48}As$ *Heterostructure*. Phys. Rev. Lett., 78, 7, 1335-1338 (1997).

[17] H. C. Koo, J. H. Kwon, J. Eom, J. Chang, S. H. Han, M. Johnson. *Control of spin precession in a spin-injected field effect transistor*. Science, Vol 325, 5947 (2009).

[18] H. T. Man, I. J. W. Wever and A. F. Morpurgo. *Spin-dependent quantum interference in single-wall carbon nanotubes with ferromagnetic contacts*. Phys. Rev.B (Condenced Matter and Materials Physics), 73(24), 241401 (2006).

[19] G. E. Blonder, M. Tinkham, T. M. Klapwijk. *Transition from metallic to tunneling regimes in superconductive microconstriction. Excess current, change imbalance and supercurrent conversion*. Phys. Rev. B, 25, 7, 1335 - 1338 (1982).

[20] M. Julliere. *Spin-polarized electron tunneling*. Phys .Lett. A, 54:225 (1975).

[21] J. M. MacLaren, X.-G. Zhang, W. H. Butler. *Validity of the julliere model of spin-dependent tunneling*. Phys. Rev. B, 56, 11827-11832 (1997).

[22] J. M. Teresa, A. Barthelemy, A. Fert, J. P. Contour, R. Lyonnet, F. Montaigne, P. Seneor and A. Vaures. *Inverse tunnel magnetoresistance in* $Co/SrTiO_3/La_{0.7}Sr_{0.3}MnO_3$*: New ideas on spin polarized tunneling*. Phys. Rev. Lett, 56: 665, (1990).

[23] Y. Suzuki, S. Yuasa, T. Nagahama. *Spin-polarized resonant tunneling in magnetic tunnel junctions*. Science, 61: 2472, pages 234-237 (2002).

[24] J. C. Slonczewski. *Conductance and exchange coupling of two ferromagnets separated by a tunneling barrier*. Phys. Rev.B, 39(10), 6995-7002 (1989).

[25] M. Buttiker. *Symmetry of electrical-conduction*. IBM J. Res. Dev., 32, pages 317-334 (1988).

[26] Y. Imry, R. Landauer. *Conductance viewed as trasmission*. Rev. Mod. Phys., 71, pages 306-312 (1999).

[27] R. Landauer. *Electrical resistance of disordered one-dimensional latices*. Phil. Mag., 21, 863, 0-19-852500-1 (1970).

[28] T. Delattre. *Current quantum frluctuations in carbon nanotubes*. PhD Thesis, University Paris VI (2009).

[29] P. D. Huertas-Hernando, Y. V. Nazarov, A. Brataas, G. E. W. Bauer. *Conductance modulation by spin precession in noncollinear ferromagnet normal-metal ferromagnet systems*. Phys. Rev. B, 62, 5700-5712 (2000).

[30] X. Waintal, O. Parcollet. *Current induced Spin Torque in a nanomagnet*. Phys. Rev. Lett., 94, 247206 (2005).

[31] M. Braun, J. Konig, and J Martinek. *Theory of transport through quantum-dot spin valves in the weak-coupling regime*. Phys Rev B, 70, 195345 (2004).

[32] K. Ono, H. Shimada and Y. Ootuka. *Enhanced magnetic valve and magneto-Coulomb oscillations in ferromagnetic single electron transistor*. J. Phys. Soc. Jpn, 67, 2852 (1998).

[33] F. J. Jedema, H. B. Heersche, A. T. Filip, J. J. A. Baselmans, B. J. van Wees. *Electrical detection of spin precession in a metallic mesoscopic spin valve*. Nature, 416, 713-716 (2002).

[34] S. Datta, L. Marty, J. P. Cleuziou, C. Tilmaciu, B. Soula, E. Flahaut, and W. Wernsdorfer. *Magneto-Coulomb Effect in Carbon Nanotube Quantum Dots Filled with Magnetic Nanoparticles*. Phys. Rev. Lett., 107, 186804 (2011).

[35] S. Sahoo and T. Kontos, J. Furer, C. Hoffman, M. Graber, A. Cottet, C. Schronenberger. *Electric field control of spin transport*. Nature Physiscs, 1:99 (2005).

[36] A. Cottet and M.-S. Choi. *Magnetoresistance of a quantum dot with spin active interfaces*. Phys. Rev.B, 74(23), 235316 (2006).

[37] A. Pasupathy, R. C. Bialczak, J. Martinek, J. E. Grose, L. A. K. Donev, P. L. McEuen, D. C. Ralph. *The Kondo effect in the presence of ferromagnetism*. Science, 306(5693), 86-89 (2004).

[38] J. Paaske, J.R. Hauptman and P.E. Lindelof. *Electric-field-controlled spin reversal in a quantum dot with ferromagnetic contacts*. Nature Physics, 4, 373-376 (2008).

[39] Y. Martin and K. Wickramasinghe. *Magnetic Imaging by Force Microscopy with* 1000 *A Resolution*. Appl. Phys. Lett., 50(20), 1455-1457 (1987).

[40] W. A. Ferrando, R. Segnan, A. I. Schindlerl. Phys. Rev. B, B5, 4657 (1972).

[41] M. Hansen. *Constitution of Binary Alloys*. McGraw-Hill Book (1958).

[42] A. Biehler, M. Klaui, M. Fonin, C. Konig, G. Guntherodt, U. Rudiger. Phys. Rev. B, B 75, 184427 (2007).

[43] G. Fischer, A. Herr, A. Meyer. J. Appl. Phys., 39, 545 (1968).

[44] T.Y Chen, Y. Ji, C.L. Chien, and M.D. Stiles. *Current-Driven Switching in a Single Exchange-Biased Ferromagnetic Layer*. Phys. Rev. Lett., 93, 026601 (2004).

[45] J.-Y. Chauleau, R. Weil, A. Thiaville, J. Miltat. *Magnetic domain walls displacement : automotion vs. spin-transfer torque*. Phys. Rev. B, 82, 214414 (2010).

[46] A. Cottet, T. Kontos, S. Sahoo, H. T. Man, M.-S. Choi, W. Belzig, C. Bruder, A. F. Morpurgo, C Schonenberger. *Nanospintronics with carbon nanotubes*. Semiconductor Science and Technology, 21, 11, S78 (2006).

[47] A. Cottet, T. Kontos, W. Belzig, C. Schonenberger and C. Bruder. *Controlling spin in an electronic interferometer with spin-active interfaces*. Europhys. Lett., 74, 320 (2006).

[48] L. E. Hueso, J. M. Pruneda, V. Ferrari, G. Burnell, J. P. Valdes-Herrera, B. D. Simons, P. B. Littlewood, E. Artacho, A. Fert, N. D. Mathur. *Transformation of spin information into large electrical signals using carbon nanotubes*. Nature Lett., Vol 445, 410 (2007).

[49] W. Wetzels, G. E. W. Bauer. *Exchange effects on electron transport through single-electron spin-valve transistors*. Phys. Rev. B, 74, 224406 (2006).

[50] P. Seneor, A. Bernard Mantel, F. Petroff. *Nanospintronics: when spintronics meets single electron physics*. Journall of Physics (Condensed Matter), 19, 165222 (2007).